Controlled nanometer liquid layer thicknesses for the study of nanomaterials and biospecimens in liquid-cell transmission electron microscopy

by

Tyler Lott

A thesis
presented to the University of Waterloo
in fulfillment of the
thesis requirement for the degree of
Doctor of Philosophy
in
Chemistry

Waterloo, Ontario, Canada, 2023

© Tyler Lott 2023

Examining Committee Membership

The following served on the Examining Committee for this thesis. The decision of the Examining Committee is by majority vote.

External Examiner:	Jason R. Dwyer Professor, Dept. of Chemistry, University of Rhode Island
Supervisor:	Germán Sciaini Associate Professor, Dept. of Chemistry, University of Waterloo
Internal Member:	Anna Klinkova Assistant Professor, Dept. of Chemistry, University of Waterloo
Internal-External Member:	Michael Pope Associate Professor, Dept. of Chemical Engineering, University of Waterloo
Other Member(s):	Tanya Prozorov Adjunct Assistant Professor, Dept. of Chemistry, University of Waterloo

Author's Declaration

This thesis consists of material all of which I authored or co-authored: see Statement of Contributions included in the thesis. This is a true copy of the thesis, including any required final revisions, as accepted by my examiners.

I understand that my thesis may be made electronically available to the public.

Statement of Contributions

This thesis presents a suite of instrumentation solutions to resolve a long-standing challenge within the field of liquid-cell transmission electron microscopy (LC-TEM), that is the presence of window membrane bulging during *in-situ* measurements. Throughout the course of this Ph.D. project I have had the opportunity to develop a unique and proprietary nanofluidic cell (NFC), electron microscopy holders, and a NFC sample loading tool (loading station) for LC-TEM. Through the reverse-engineering of existing electron microscope holders for conventional transmission electron microscopy (TEM) and the use of SolidWorks computer-aided design (CAD) software, I designed, developed drawings, and worked directly with precision machinists to produce electron microscopy holders and loading stations for the assembly of proprietary NFCs. Working as an assistant to Dr. Ariel Petruk in the Quantum Nano Fabrication and Characterization Facility (QNFCF), I aided in the development of a unique and proprietary NFC design to be used in conjunction with the electron microscopy holders and loading station that I developed. This thesis outlines the development of the suite of instrumentation during the course of my Ph.D. and presents preliminary results of the developed technology and instrumentation by successfully reporting the virtual elimination of bulging within LC-TEM experiments conducted on model systems.

Throughout the course of this Ph.D. project I have developed LC-TEM holders and

loading stations for the three major electron microscope companies (FEI, Hitachi, and JEOL). For the purposes of this thesis, the instrumentation for FEI microscopes is discussed as these microscopes were readily available for preliminary experiments at the Canadian Centre for Electron Microscopy (CCEM).

In addition to these contributions, I have similarly developed prototypes of a Cryo-electron microscopy (Cryo-EM) holder, a Faraday cup holder for electron microscopy, and an LC-TEM flow holder. These developments are works in progress.

Portions of Chapters 2 and 3 were adapted from:

1. Lott, T. S.; Petruk, A. A.; Shaw, N. A.; Hamada, N.; Andrei, C. M.; Liu, Y.; Liu, J.; Sciaini, G.; Robust Fully Controlled Nanometer Liquid Layers for High Resolution Liquid-Cell Electron Microscopy, *Lab Chip*, **23**, 3217-3225, (2023); also in ChemRxiv, https://doi.org/10.26434/chemrxiv-2023-834fn.

DOI = 10.1039/D3LC00190C

https://doi.org/10.1039/D3LC00190C

2. Lott, T. S.; Petruk, A. A.; Sciaini, G.; A miniature high-vacuum valve, *engrXiv*, 2021.

DOI = 10.31224/osf.io/hx4np

https://doi.org/10.31224/osf.io/hx4np

3. Lott, T. S.; Petruk, A. A.; Shaw, N. A.; Hamada, N.; Andrei, C. M.; Liu, Y.; Liu, J.; Sciaini, G.; A High-Throughput Method for Bulgeless Liquid Cell Imaging in the Transmission Electron Microscope, *Microsc. Microanal.*, 2023 Jul 22; 29 (Supplement_1): 658-659.

DOI = 10.1093/micmic/ozad067.323

https://doi.org/10.1093/micmic/ozad067.323

Other co-authored work not included in this thesis:

1. Gicala, P.; Cheng, M.; Lott, T.S.; Du, K.; Cheong, S.-W.; Petruk, A. A.; Pichugin, K.; Sciaini, G.; Time-resolved broadband impulsive stimulated Brillouin scattering in single crystal hematite, *Appl. Phys. Lett.*, 28 June 2021; 118 (26): 264101.

DOI = 10.1063/5.0057604

https://doi.org/10.1063/5.0057604

2. Shaw, N. A.; Lott, T. S.; Petruk, A. A.; Hamada, N.; Andrei, C. M.; Liu, Y.; Liu, J.; Sciaini, G.; High-Throughput Low-Dose Biomolecule Imaging in Liquid Phase Electron Microscopy, *Microsc Microanal.*, 2023 Jul 22; 29 (Supplement_1): 986-987.

DOI = 10.1093/micmic/ozad067.493

https://doi.org/10.1093/micmic/ozad067.493

3. Thiemann, F.; Sciaini, G.; Kassen, A.; Lott, T.S.; Horn-von Hoegen, M.; Deciphering the Real and Imaginary Components of the Dielectric Response of Photoexcited Bismuth (Submitted *Phys. Rev. Lett*).

Design and testing of the nanofluidic electron microscope holder, loading station, and methodology was completed by myself with the advisory supervision of Dr. Ariel Petruk and Prof. Germán Sciaini. Machining was performed by Science Technical Services (STS) at the University of Waterloo. Nanofluidic cell design and nanofabrication was conducted by Dr. Ariel Petruk with assistance from myself and Nicki Shaw. LC-TEM experiments presented in this thesis were conducted at the CCEM by myself, Nicki Shaw, and Dr. Ariel Petruk with guidance from the electron microscope technicians: Carmen Andrei and Natalie Hamada. Electron energy loss spectroscopy (EELS) and image data analyses were completed by myself.

Abstract

Liquid-cell transmission electron microscopy (LC-TEM) is an *in-situ* microscopy technique which aims to image nanomaterials and biospecimens in their native liquid phase environment. To accomplish this task, miniature vessels known as nanofluidic cells (NFCs) are utilized to enclose the liquid sample droplet and protect it from evaporating in the high or ultra-high vacuum of the electron microscope. These NFCs must conform to strict requirements so that a small volume of liquid sample is hermetically sealed between two ultrathin windows. Although the technique has seen significant growth in recent years with the utilization of hybrid material window membranes for improved imaging resolution,[1,2] the incorporation of machine learning techniques for image processing,[3] and advancements in bio-imaging in the liquid phase,[4] the establishment of uniform thin liquid layers in the absence of membrane bulging has remained a challenge. The bulging of window membranes causes inhomogeneity across the viewing area of the assembled NFC. Since conventional NFCs are structurally sensitive to handling and are assembled in the atmosphere of the laboratory environment before being inserted into the electron microscope for imaging, bulging of the thin window membranes occurs. Researchers thus have been led to collect their LC-TEM data along the edges of the windows where bulging is minimized and therefore resolution is maximized.[5,6] In this thesis a complete suite of instrumentation is presented, comprising: i) proprietary shape-engineered NFCs, ii) LC-TEM

holders, and iii) a proprietary sample loading method/station that allows the enclosure of liquid in the absence of air. This combined technology enables the formation of uniform thin liquid layers for LC-TEM measurements in the absence of window membrane bulging. The capabilities of this method to achieve uniform thin liquid layers in assembled NFCs are demonstrated through the high-resolution imaging of gold (Au) nanorods, polystyrene (PS) nanospheres, and 1,2-dioleoyl-sn-glycero-3-phosphocholine (DOPC) liposomes as model sample specimens. In addition to these high-resolution images, electron energy loss spectroscopy (EELS) measurements were conducted within the electron microscope as a means to quantify the liquid layer thickness. The developed instrumentation and methodology resolves a long-standing issue in the LC-TEM community, conferring high-throughput imaging and establishing uniform thin liquid layers across the complete viewing area of the assembled NFC, enabling lattice resolution for crystalline materials and high-contrast for biospecimens.

Acknowledgements

I would like to thank everyone who has made the work in this thesis possible. During my time at the Ultrafast electron Imaging Lab (UeIL) I have been fortunate to be involved in a wide variety of research topics; and while the work made UeIL interesting, the people I worked with made it feel like home. I would first like to thank Dr. Nicolás Rivas who provided a tremendous amount of support and training in my early days at the UeIL during my time as a M.Sc. student. Working with Dr. Rivas provided me with a chance to learn about experimental development and apply Python scripting to data analysis. This was an extremely valuable experience that I have carried forward with me throughout my research. I owe a immense degree of gratitude to Dr. Ariel Petruk who provided me with support in developing technical skills in the Quantum Nano Fabrication and Characterization Facility (QNFCF) as well as a tremendous amount of advice along the way. I am thankful to Nicki Shaw for all of her support throughout this research project. Thank you to all the past and present members of the UeIL with special thanks to Dr. Kostyantyn Pichugin, Patryk Gicala, Dr. Meixin Cheng, Sam Netzke, and Ruofei Zheng for making the lab and office such an enjoyable place to work. Thank you to Prof. Germán Sciaini for everything, truly. Thank you for your encouragement, kindness, and overall enthusiasm for science.

I would of course also like to thank the precision machinists at Science Technical Services (STS) with special thanks to Hiruy Haile and Andrew Dube for their patience, kindness,

and professionalism to work with me in producing the instrumentation presented in this thesis. I would also like to thank the staff at the QNFCF for their support in providing training and assistance throughout the nanofabrication process for the development of the nanofluidic cells (NFCs). Furthermore, I would like to thank Dr. Nabil Bassim and the entire staff at the Canadian Centre for Electron Microscopy (CCEM) for supporting the development of the presented technology. Special thanks to Dr. Carmen Andrei and Dr. Natalie Hamada for providing training and offering their expertise in electron microscopy.

I am also grateful to the excellent administrative staff at the University of Waterloo, especially Catherine Van Esch, who was always incredibly helpful whenever I had questions regarding the graduate program.

Thank you to my committee members: Prof. John Honek, Prof. Anna Klinkova, and Prof. Tanya Prozorov who have provided me with a lot of support and encouragement throughout my Ph.D. journey. I am very grateful to Prof. Tanya Prozorov who offered me an opportunity to conduct research at the Ames Laboratory in Iowa, U.S.A. where I first was introduced to the technique of liquid-cell transmission electron microscopy (LC-TEM).

I would also like to thank my friends and family for their love and support throughout my graduate studies.

Dedication

To curiosity!

Table of Contents

Examining Committee Membership ii

Author's Declaration iii

Statement of Contributions iv

Abstract vii

Acknowledgements ix

Dedication xi

List of Figures xiii

List of Equations xiv

List of Abbreviations xv

List of Metric Prefixes xvi

List of Chemical Abbreviations xvii

List of Symbols xviii

1 Introduction 1

1.1 Fundamentals of electron microscopy 4

1.2 Basic imaging modes of electron microscopy used in liquid-cell transmission electron microscopy 7

1.2.1 Transmission electron microscopy 7

1.2.2 Scanning transmission electron microscopy 12

1.2.3 Electron energy loss spectroscopy 13

1.3 The emergence of liquid phase investigations using electron microscopy and its challenges 17

1.4 Challenges in modern liquid-cell transmission electron microscopy 24

2 Methodology and instrumentation development 30

2.1 Methodology for conducting electron microscopy in the liquid phase 31

2.1.1 Electron transmission 31

2.1.2 Determining the liquid layer thickness with EELS 34

2.1.3 Radiolysis in LC-TEM 37

2.1.4 Carbon contamination in LC-TEM 38

2.1.5 Electron dosage in LC-TEM 39
2.2 Considerations for the design and nanofabrication of "closed cell" sandwich devices for LC-TEM 41
2.3 The evolution of the design of a static NFC assembly kit for LC-TEM . . . 60
2.4 A novel NFC for static LC-TEM experiments 64
2.5 Development of a novel method for LC-TEM sample loading 70

3 Results and discussion **86**
3.1 Instrumentation and model sample specimens utilized in this thesis 87
3.1.1 Transmission electron microscopy 87
3.1.2 Instrumentation for liquid-cell transmission electron microscopy measurements 88
3.1.3 Model systems for measurements 89
3.2 Electron beam transmission through liquids 91
3.3 Membrane deformation and liquid layer thickness measurements 92
3.4 Imaging model sample specimens in situ 100

4 Conclusion **108**
4.1 Conclusion 108

5 Outlook **110**

5.1 Outlook 110

References **112**

APPENDICES **112**

A Python Code for Data Analysis **113**

A.1 Conversion of image stacks to video 113

A.2 EMD file type conversion 121

A.3 EELS Analysis 132

A.4 Savitzky-Golay filtering 151

B Javascript Code for Data Analysis **154**

B.1 Auto contrast of image stacks 154

List of Figures

1.1 A comparison between the optical microscope and the electron microscope 6

1.2 Correction of energy spread with a monochromator 11

1.3 The principle of reciprocity between transmission electron microscopy imaging modes 13

1.4 A typical electron energy loss spectroscopy (EELS) spectrum 16

1.5 The first "closed cell" for electron microscopy (EM) 19

1.6 A "closed cell" nanofluidic cell (NFC) "sandwich" design for scanning electron microscopy (SEM) in the liquid phase 20

1.7 Different nanofluidic cell (NFC) "sandwich" designs for liquid-cell transmission electron microscopy (LC-TEM) 21

1.8 Different static nanofluidic cell (NFC) designs for liquid-cell transmission electron microscopy (LC-TEM) 23

1.9 A cartoon illustration of how nanofluidic cells (NFCs) are typically sealed within a specialized NFC holder in liquid-cell transmission electron microscopy (LC-TEM) 25

1.10 A cartoon illustrating how window membrane bulging severely reduces the maximum obtainable resolution in liquid-cell transmission electron microscopy (LC-TEM) 26

1.11 A cartoon illustration of deliberate bubble generation for liquid layer thinning in liquid-cell transmission electron microscopy (LC-TEM) 27

2.1 Theoretical electron transmission through various materials commonly used for liquid-cell transmission electron microscopy (LC-TEM) 34

2.2 A plasma cleaner used for the preparation of nanofluidic cells (NFCs) and sample holders for liquid-cell transmission electron microscopy experiments 39

2.3 A nanofabrication chemical wet bench typically used for the Radio Corporation of America (RCA) process 43

2.4 A simple photolithography process 48

2.5 The process of exposure for diazonaphthoquinone (DNQ)-novolac based photoresists 50

2.6 A diagram showing the schematic cycling of etching and passivating gases during the Bosch process 54

2.7 A summary of the nanofabrication steps described as illustrated through the development of the wafer structure 59
2.8 A universal circular nanofluidic cell (NFC) for electron microscopy 61
2.9 Various unique nanofluidic cell (NFC) designs and electron microscopy holder tips developed by the Ultrafast electron Imaging Laboratory (UeIL) 62
2.10 The various liquid-cell (LC) loading stations developed for preparing samples for static (LC-TEM) experiments 63
2.11 The dimensions of a conventional liquid-cell (LC) for liquid-cell transmission electron microscopy (LC-TEM) 64
2.12 Spacer overflow in conventional nanofluidic cells (NFCs) 66
2.13 Spacer contamination of conventional liquid-cells (LCs) from regular handling 67
2.14 New nanofluidic cells (NFCs) developed by the Ultrafast electron Imaging Laboratory (UeIL) 69
2.15 The liquid-cell transmission electron microscopy (LC-TEM) electron microscope sample holder and loading station 71
2.16 The preparation of the nanofluidic cell (NFC) assembly using the novel assembly kit 72
2.17 A cartoon illustration of the evacuation of the loading station in the preparation of a nanofluidic cell (NFC) assembly 74

2.18 Bulging of nanofluidic cell assemblies (NFC) under an applied pressure differential . . . 75
2.19 Reducing the bulging of nanofluidic cell assemblies (NFC) by reducing the short length of the silicon nitride (SiN_x) window membrane . . . 78
2.20 A detailed assembly process of the loading station designed to assemble liquid-cells (LCs) for liquid-cell transmission electron microscopy . . . 81
2.21 A miniature high-vacuum valve developed by the Ultrafast electron Imaging Laboratory (UeIL) . . . 83
2.22 The sealing process of the miniature high-vacuum valve . . . 84
2.23 Recently developed instrumentation for liquid-cell transmission electron microscopy (LC-TEM) experiments . . . 85

3.1 The contribution of water to electron beam transmission losses from total scattering cross section approximations . . . 91
3.2 Silicon nitride window membrane deformation measurements for 25 nanometre (nm) thick membranes . . . 93
3.3 A high-angle annular dark field image showing a representative line scan region for liquid thickness measurements . . . 95
3.4 Using the log-ratio method to determine the liquid layer thickness in a liquid-cell transmission electron microscopy (LC-TEM) experiment . . . 96

3.5 Liquid layer thickness measurements conducted with ultrapure water . . . 97
3.6 Bowing of nanofluidic cells (NFCs) observed through electron energy loss spectroscopy (EELS) measurements . . . 98
3.7 Demonstrating the uniformity of the liquid layer thickness across the viewing area of the nanofluidic cell (NFC) . . . 101
3.8 Demonstrating high-resolution scanning transmission electron microscopy (STEM) imaging *in situ* . . . 103
3.9 A line-intensity profile measurement of a gold nanorod located at the centre of the nanofluidic cell (NFC) assembly . . . 104
3.10 Imaging unstained liposomes *in situ* . . . 105
3.11 High-resolution images of gold nanorods in solution . . . 107

List of Equations

1.1 de Broglie's theory of light-matter wave propagation: Relativistic electron wavelength 4

1.2 Diameter of a chromatically aberrated image disc in an electron microscope . 9

1.3 Diameter of a spherically aberrated image disc in an electron microscope . . 11

2.1 Approximating the total scattering cross section from the total elastic scattering cross section 32

2.2 Approximating the total mean free path of an electron interacting with a material 32

2.3 Relating the electron beam transmission to the total mean free path and thickness of a given material 32

2.4 Determining the liquid layer thickness in a liquid-cell transmission electron microscopy experiment: The log-ratio equation 34

2.5 Determining the liquid layer thickness in a liquid-cell transmission electron microscopy experiment: The inelastic mean free path of the electron 34

2.6 Determining the liquid layer thickness in a liquid-cell transmission electron microscopy experiment: The relativistic factor 35
2.7 Determining the liquid layer thickness in a liquid-cell transmission electron microscopy experiment: The average energy loss through a material 35
2.8 Determining the liquid layer thickness in a liquid-cell transmission electron microscopy experiment: The effective atomic number of a material 35
2.9 Determining the liquid layer thickness in a liquid-cell transmission electron microscopy experiment: Partitioning intensity contributions from the total intensity ratio 35
2.10 Determining the liquid layer thickness in a liquid-cell transmission electron microscopy experiment 35
2.11 Determination of the electron dose per frame for electron micrographs 39
2.12 Silicon etch rate in a potassium hydroxide (KOH) bath 56
2.13 Determining the final pressure in the loading station vacuum chamber 73
2.14 Bulging of silicon nitride membranes under a uniform pressure 76

List of Abbreviations

A Ampere(s)

atm Standard atmosphere

BSE Backscattered Electron(s)

CAD Computer-Aided Design

CCD Charge-Coupled Device

CCEM Canadian Centre for Electron Microscopy

CEOS Corrected Electron Optical Systems

CFEG Cold Field Emission Gun

CMOS Complementary Metal-Oxide Semiconductor

Cryo-EM Cryo-Electron Microscopy

EELS Electron Energy Loss Spectroscopy

EFTEM Energy Filtered Transmission Electron Microscopy / Energy Filtered Transmission Electron Microscope(s)

EM Electron Microscopy / Electron Microscope(s)

ESEM Environmental Scanning Electron Microscopy / Environmental Scanning Electron Microscope(s)

eV Electronvolt(s)

FEG Field Emission Gun

FWHM Full Width at Half Maximum

g Gram(s)

GIF Gatan Imaging Filter

GLC Graphene Liquid Cell(s)

h Hour(s)

HAADF High-Angle Annular Dark Field

HEPA High-Efficiency Particulate Absorbing

IC Integrated Circuit(s)

IEE Ion Enhanced Etching

IMFP Inelastic Mean Free Path

iSCAT Interferometric Scattering Microscopy

ISO International Organization for Standardization

kx Thousand times

L Litre(s)

LC Liquid-Cell(s)

LC-TEM Liquid-Cell Transmission Electron Microscopy

LPCVD Low Pressure Chemical Vapour Deposition

m Metre(s)

M Molar

NFC Nanofluidic Cell(s)

OD Optical Density

Pa Pascal(s)

QNFCF Quantum-Nano Fabrication and Characterization Facility

RCA Radio Corporation of America

RF Radio Frequency

RIE Reactive Ion Etching

rpm Revolutions Per Minute

s Second(s)

SC-2 Standard Clean 2

SC-1 Standard Clean 1

sccm Standard Cubic Centimetres per Minute

SEM Scanning Electron Microscopy / Scanning Electron Microscope(s)

SMLM Single-Molecule Localization Microscopy

SRM Super-Resolution Microscopy

STEM Scanning Transmission Electron Microscopy / Scanning Transmission Electron Microscope(s)

STS Science Technical Services

TEM Transmission Electron Microscopy / Transmission Electron Microscope(s)

UeIL Ultrafast electron Imaging Laboratory

USP United States Pharmacopeia

UV Ultraviolet

V Volt(s)

W Watt(s)

ZLP Zero-Loss Peak

List of Metric Prefixes

p Pico-: a metric prefix which denotes a multiplication of 10^{-12} for a given unit.

n Nano-: a metric prefix which denotes a multiplication of 10^{-9} for a given unit.

μ Micro-: a metric prefix which denotes a multiplication of 10^{-6} for a given unit.

m Milli-: a metric prefix which denotes a multiplication of 10^{-3} for a given unit.

c Centi-: a metric prefix which denotes a multiplication of 10^{-2} for a given unit.

k Kilo-: a metric prefix which denotes a multiplication of 10^{3} for a given unit.

M Mega-: a metric prefix which denotes a multiplication of 10^{6} for a given unit.

List of Chemical Abbreviations

NH_3 Ammonia

NH_4OH Ammonium hydroxide

DNQ Diazonaphthoquinone

SiH_2Cl_2 Dichlorosilane

DOPC 1,2-dioleoyl-sn-glycero-3-phosphocholine

GeO_2 Germanium oxide(s)

Au Gold

GOx Graphene Oxide(s)

HCl Hydrochloric acid

HF Hydrofluoric acid

H_2O_2 Hydrogen Peroxide

HEPES 4-(2-hydroxyethyl)-1-piperazineethanesulfonic acid

IPA Isopropyl alcohol

NMP N-methyl-2-pyrrolidone

C_4F_8 Octafluorocyclobutane

Pd@Ru Palladium core, ruthenium shell

PEEK Polyether ether ketone

PS Polystyrene

KOH Potassium hydroxide

SiO_2 Silica / silicon dioxide

SiN_x Silicon nitride

NaCl Sodium chloride

Si_3N_4 Stoichiometric silicon nitride

SF_6 Sulfur hexafluoride

H_2O Water

List of Symbols

Å Angstrom: a metric unit of length which is defined as 10^{-10} m

Ω Ohm: a unit of electrical resistance.

Chapter 1

Introduction

Researchers have long sought after an imaging technique to characterize *in-situ* processes occurring in liquids with highly resolved image quality. Confocal microscopy is capable of characterizing samples without the threat of damage from a high energy probe, but is limited by diffraction to an optimum spatial resolution of 200 nanometres (nm).[7,8] Other techniques exist which surpass the diffraction limit such as super-resolution microscopy (SRM) and interferometric scattering microscopy (iSCAT).[9,10] For example, single-molecule localization microscopy (SMLM), is recognized to offer the highest potential spatial resolution of SRM techniques with a spatial resolution typically in the range of 20-50 nm.[9,11] However, this technique requires long acquisition times, typically tens of minutes, limiting its utilization for studies requiring the acquisition of dynamic information.[11,12] SRM is able

to achieve high-resolution imaging where atomic resolutions are not required, offering high specificity due to the use of fluorophores coating the sample, however this procedure disrupts the native conditions of the sample environment.[9] While iSCAT can offer spatial resolutions similar to SRM, this technique does not coat the specimen with fluorophores and as a result lacks the specificity of SRM.[10,13] In addition, iSCAT is highly sensitive to nanoscopic amounts of matter such that slight variations in the optical path can cause a background signal which is challenging to remove from the signal of interest.[13] Both SRM and iSCAT offer the potential to be complementary to LC-TEM with a capability of offering nanoscale spatial resolution. However, both techniques still lack the ability to achieve atomic resolutions *in situ*. In contrast, electron microscopy (EM) offers researchers the capability to probe samples with atomic resolution but often does so by taking the sample out of its native environment through the use of chemical fixation due to the fact that electron microscopes operate under a high or ultra-high vacuum.

To achieve high-resolution imaging while preserving the natural state of the *in-situ* process occurring in the liquid phase, one needs to utilize a different approach with additional instrumentation. Liquid-cell transmission electron microscopy (LC-TEM) is an imaging technique which allows for the high-resolution imaging of materials and biospecimens *in situ* through the use of nanofabricated liquid storage vessels. These nanofluidic cells (NFCs) have led to the realization of a wide variety of *in-situ* and *in-operando* studies

including the monitoring of magnetic induction in magnetotactic bacteria,[14] the observation of diffusion dynamics in electrochemical processes,[15] and the oxidation of core-shell nanoparticle systems.[16] In order to accomplish the characterization of processes such as these, researchers must ensure that they are generating an appropriate environment for the process of interest. By utilizing established methods of nanofabrication, NFCs may be engineered to allow for the study of a wide variety of processes through the use of cleverly designed temperature control systems, the design of micro-electrodes, the selection of an appropriate window membrane material, and the manipulation of liquid layer thickness with spacer materials.[17,18] However, despite the vast improvements which have been made in the nanofabrication of devices and instrumentation for LC-TEM, a number of key challenges still remain to achieve high-resolution imaging with reproducibility and high-throughput. In this thesis, a new methodology employing unique instrumentation for the study of *in-situ* samples in the electron microscope is outlined and demonstrated. The demonstrated instrumentation and methodology confers reliable uniform liquid layer thicknesses with a sample loading technique that offers a new and unique solution to solve the challenges which exist in conventional LC-TEM experiments. To begin the discussion of how this technology is enabling the advancement of the field of LC-TEM, a brief introduction to electron microscopy is given, the requirements of the LC-TEM technique are discussed, and a brief history of the field and its challenges are introduced.

1.1 Fundamentals of electron microscopy

According to the Abbe diffraction limit, in a conventional microscope the spatial resolution is limited to roughly half the wavelength of the illumination source.[7] The electron is therefore an excellent candidate for achieving high spatial resolutions as electrons can be generated from a stable source, they can be readily accelerated to achieve shorter wavelengths, and they can be manipulated with electromagnetic fields to control the optical path. Following from de Broglie theory, it was acknowledged that the electron could be utilized to perform imaging.[19]

de Broglie's theory of wave-particle duality and the dependence of the wavelength of the electron on the acceleration voltage is highlighted in Equation: 1.1 below:

$$\lambda = \frac{\frac{h}{\sqrt{2m_0eV}}}{\sqrt{1+\frac{eV}{2m_0c^2}}} \tag{1.1}$$

where λ is the wavelength of the electron, h is Planck's constant, m_0 is the mass of the electron, e is the fundamental charge of the electron, V is the acceleration voltage of the electron, and c is the speed of light in a vacuum.

From Equation: 1.1 it is clear that the wavelength of the electron can be made in-

credibly short through the utilization of a high acceleration voltage inside of the electron microscope. Thus, comparing the wavelength of the electron to the wavelength of light in an optical microscope, it is clear that one can resolve much smaller features with an electron microscope. While electrons offer a significantly reduced wavelength for improved resolution capabilities in imaging, there are a number of challenges that arise from using electrons for imaging. Electron microscopy must be conducted in a high or ultra high-vacuum environment since interactions of the short wavelength electron with contaminant particles in the air can cause the electrons to scatter, severely diminishing the coherence of the electron beam before the electron beam has reached the sample. Both optical microscopy and electron microscopy rely on an illumination source (photons vs. electrons), lenses (optical vs. electromagnetic), apertures, and a camera to record the image. The electron microscope is compared to the optical microscope in Figure: 1.1.[20] From the illumination source, a condenser lens condenses the source of illumination into the sample plane, the transmitted beam is then magnified for viewing by an observer using an objective lens and a projector lens.[20]

There are many important theoretical factors to discuss in order to achieve the acquisition of high-quality data from the electron microscope. Further details can be explored in a variety of classic electron microscopy textbooks such as the one from Kohl and Reimer.[21] Next, a short introduction to commonly used imaging modes in LC-TEM will be intro-

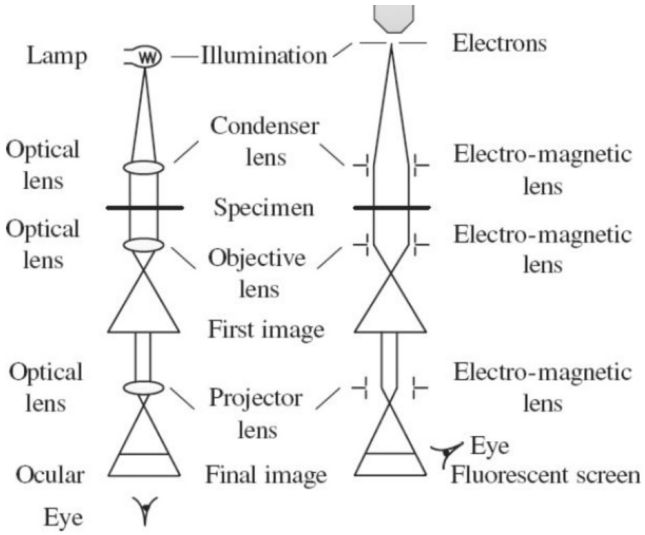


Figure 1.1: A comparison between the optical microscope and the electron microscope. Reproduced with permission from X. Chen, Optical and digital microscopic imaging techniques and applications in pathology, *Anal. Cell Path.*, **34**, 5-18, (2011). Copyright © 2011 Hindawi Publishing Corporation and the authors.[20]

duced, followed by a discussion of the application of electron microscopy in liquid phase experiments. As we will see, the liquid phase presents a unique challenge for both imaging and the preparation of samples.

1.2 Basic imaging modes of electron microscopy used in liquid-cell transmission electron microscopy

1.2.1 Transmission electron microscopy

In transmission electron microscopy (TEM), an ultrathin sample specimen is irradiated with a plane wave of a collimated beam of electrons accelerated through the microscope column with a voltage typically in the range of 100 - 300 kilovolts (kV). The electrons are emitted from what is known as the electron gun, a component which acts as a source of electrons which are typically generated from thermionic emission or field emission.[22–24] In a conventional TEM, the area of the sample which is illuminated is controlled by two condenser lenses, allowing for fine control in the variability of the electron illumination.[21] This illumination system ensures that the intensity of the formed image is sufficient across all magnifications. After the electron beam has transmitted through the sample, a series of lenses including the objective, magnify and project the formed image onto a fluorescent screen or onto a camera. The typical image which is formed in conventional TEM is one which is said to have a bright-field contrast. In this imaging mode, the sample of interest appears to be darker than the support membrane (field) which it is resting on. Within the microscope such an image is obtained with either scattering contrast or phase

contrast. When the scattered electrons reach the objective aperture at angles larger than the objective aperture, the image is said to display scattering contrast. Phase contrast is obtained through modulation of the microscope's contrast transfer function which is an interference of the scattered wave and the unscattered wave on the imaging plane.[21] In addition, it is possible to achieve dark field contrast by causing the primary beam to fall on the diaphragm of the objective lens through tilting or hollow-cone illumination.

While the electron gun, illumination system, and imaging system of the electron microscope allow a user to form images with a variety of contrasts each with their own significant advantages, one must also consider the limiting factors which act as a barrier to achieving high-resolution imaging in the electron microscope. Just as optical microscopy has limitations based on the wavelength of the illumination source and the aberrations which exist in the optical components, electron microscopy also faces similar barriers. In recent decades much effort has been put into the aberration correction of electron microscopes. There are two main types of aberrations which plague the resolution capabilities of the electron microscope, chromatic aberrations and spherical aberrations.

Chromatic aberrations exist within the electron microscope due to variations in the electron energy which in turn causes variations in the focal length. In addition, energy losses can occur as the electron beam passes through the sample specimen (eg. electron energy loss spectroscopy (EELS)), limiting the resolution by the energy spread of the

electron beam. When energy spread of the electron beam occurs, the point which is imaged is represented by a chromatic-aberration disc as indicated in Equation: 1.2.[21] With the recent work that has been done in the correction of aberrations in electron microscopes and the advent of new imaging techniques, the resolution of the microscope is approaching the limit set by the vibration of the atomic lattice.[25]

$$d_c = \frac{1}{2} C_c \frac{\Delta E}{E} \frac{1 + \frac{E}{E_0}}{1 + \frac{E}{2E_0}} \alpha_o M \tag{1.2}$$

where d_c is the diameter of the chromatically aberrated disc formed at the image point, C_c is the chromatic-aberration coefficient, ΔE is the energy spread of the electron beam, E is acceleration voltage, E_0 is the rest energy of the electron, α_o is the angular aperture defined by the objective diaphragm, and M is the magnification.

The chromatic aberration coefficient is typically on the order of $0.6f$ to f, where f is the focal length of the lens from which the chromatic aberration is arising. The thickness of the sample specimen plays a significant role in the formation of chromatic aberration. As electrons pass from the electron gun to the sample specimen, as thickness of the sample specimen increases, the number of inelastically scattered electrons substantially increases. These interactions are detrimental for the formation of highly resolved images and therefore

the spectrum of electron energies which are lost to the specimen will broaden.[21] To combat these effects, an operator of an electron microscope can employ a monochromator within the electron microscope or utilize energy filtering to focus on the most probable energy of the electron beam to reduce the energy spread of the electron beam to 0.1 electronvolts (eV) or less.[26,27] An assembly of electromagnetic optical components, is placed behind the objective lens to correct for the aberrations of the objective lens. There are a variety of different configurations for the incorporation of monochromators within the electron microscope.[26,27] The improvement that a monochromator makes on the energy spread of the electron beam can be visualized in Figure: 1.2.

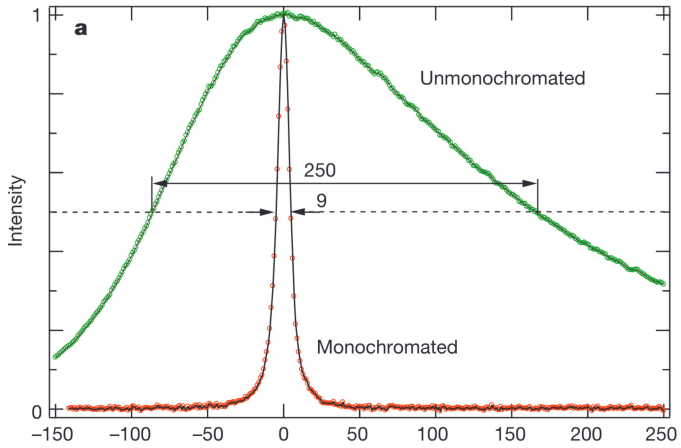


Figure 1.2: Correction of energy spread with a monochromator. The zero-loss peak (ZLP) from an unmonochromated electron beam is compared to the ZLP from a monochromated electron beam. Both measurements were conducted in an electron microscope with a cold field emission gun (CFEG). The energy spread is measured by the full width at half maximum (FWHM) of the ZLP in the energy loss spectrum, indicating a 250 millielectronvolt (meV) FWHM for the unmonochromated beam and a 9 meV FWHM for the monochromated beam. An acceleration voltage of 60 kiloelectron volts (keV) was utilized in these measurements. Reproduced from O. L. Krivanek *et al.*, Vibrational Spectroscopy in the Electron Microscope, *Nature*, **514**, 209-212, 2014, Springer Nature, reproduced with the permission of SNCSC.[28]

In addition to chromatic aberration, spherical aberration plays a role in limiting the resolution of electron microscopy. Electrons which travel through the outer edge of the lens will inherently have their focal length reduced, thus electrons passing through the lens will focus at different points after passing through the objective lens and therefore the resulting image will be blurred.[21] Spherical aberration in electron microscopy is a phenomenon which originates due to the utilization of rotationally symmetric lenses. The electromagnetic potential formed focuses the electrons more extremely at the boundaries of the lenses and thus spherical aberrations exist.[29,30] When spherical aberration is present in the imaging plane, the point which is imaged is represented by a spherical aberration disc as indicated in Equation: 1.3.[21]

$$d_s = 2C_s{\alpha_o}^3 M \tag{1.3}$$

where d_s is diameter of the spherically aberrated disc formed at the image point, C_s is the spherical-aberration coefficient, α_o is the angular aperture defined by the objective diaphragm, and M is the magnification.

In general, objective lenses in the electron microscope normally have a spherical-aberration coefficient of 0.5 to 2 millimetres (mm). Spherical aberrations are reduced

in the electron microscope by the utilization of multipole lens configurations which also correct for chromatic aberrations.[21]

1.2.2 Scanning transmission electron microscopy

The aberrations which limit the resolution of the conventional TEM also affect the imaging mode known as scanning transmission electron microscopy (STEM). In the STEM imaging mode, the electron beam is typically focused to a probe diameter of 0.2 to 5 nm and this beam is scanned over the surface of the sample specimen so that electrons are scattered forwards into the detector.[21,24] In contrast to the TEM mode of electron microscopy, STEM is said to be incoherent and when operated in the high-angle annular dark field (HAADF) mode, exceptionally high contrast is available for high atomic number materials. Incoherent illumination can also lead to higher resolution imaging, although low contrast materials, such as carbonaceous materials, are poorly visible in the HAADF mode as a result of the scattering dependence on the high-atomic number.[24,31] By scattering electrons from the sample at shallow angles, the STEM imaging mode can also be utilized to obtain images with a bright field contrast similar to the TEM imaging mode.[32] The STEM mode is also said to be the reciprocal of the TEM imaging mode such that a wave at point A which originated from a source B is the same as a wave detected at point B from a source at A.[21] A simplified diagram of the STEM and TEM setups is illustrated in Figure: 1.3.

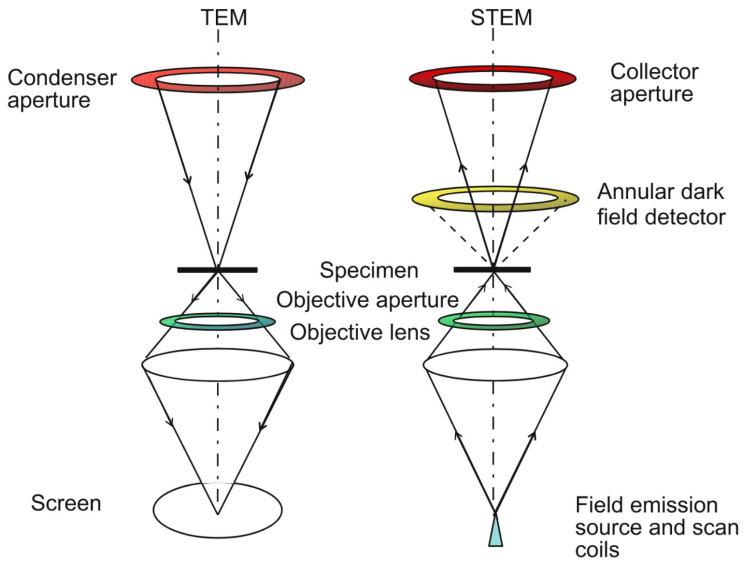


Figure 1.3: The principle of reciprocity between transmission electron microscopy imaging modes. Reproduced from T. T. Shang *et al.*, Interface of transition metal oxides at the atomic scale, *Sci. China: Phys. Mech. Astron.*, **59**, (2016), by permission of SNCSC.[32]

1.2.3 Electron energy loss spectroscopy

Electron energy loss spectroscopy (EELS) is a technique utilized in transmission electron microscopy to study the interaction of a monoenergetic electron beam with a sample specimen.[33] This technique can be deployed for a wide variety of studies such as the assessment of sample specimen thickness,[34] the quantification and characterization of the material present within a sample,[35] and it may even be used to observe the vibrational motions of atoms within the sample specimen.[28] Electrostatic forces regulate the interactions of electrons as they pass through a material. As electrons impact the material, some are

scattered and a change in momentum occurs such that the electron transfers a portion of its energy from its acceleration to the material. For EELS we are primarily concerned with two types of scattering, those being elastic and inelastic scattering. Classically, elastic scattering occurs when the electrostatic forces of atomic nuclei, which can be thought of as point charges, cause electrons to divert from their initial trajectory due to repulsion from the electric field surrounding the nucleus. Collisions between the electron and an atom can occur at shallow scattering angles (less than 90°) or large scattering angles up to a head-on collision where the scattering angle is equal to 180°. When an electron collides with an atom at large angles, backscattering occurs and the electron can eject from the same position in the specimen from which it entered. Energetically, these large angle interactions transfer significantly more energy to the atom than a shallow angle interaction. In a crystalline solid, this scattering occurs as diffraction where electron waves are scattered as a distribution of sharp peaks dictated by the atomic spacing within the lattice.[33]

Inelastic scattering occurs when the incoming electron interacts with an electron surrounding an atom in the material. This interaction can excite the atomic electrons to a higher energy level. The resulting de-excitation process of these interactions can lead to the emission of light, Auger electrons, secondary electrons, and x-rays, allowing for the study of a wide variety of electron-material interactions. Inelastic scattering is also the basis for the formation of plasmon resonance in some materials. Plasmon resonance is

a collective phenomenon in which a portion of the energy from the incoming electron is shared among many atoms when the process is observed over an extended period.[33,36] In an electron microscope, an EELS experiment is conducted by transmitting the beam of electrons through the sample specimen and into a high-resolution spectrometer. The spectrometer allows for the separation of electrons into an intensity spectrum which quantifies the number of scattered electrons as a function of the kinetic energy lost to the sample specimen. Within a typical energy loss spectrum, a sharp peak is observed at the beginning of the spectrum. This peak is known as the zero-loss peak (ZLP) and it is made up of all of the electrons that pass into the spectrometer unscattered by the specimen or elastically scattered with insignificant energy lost to the specimen. At energy losses of 4 to 40 eV, inelastic scattering from electrons within the outer shell of the atom (in the Bohr model) can be observed as a peak. Inelastic scattering from electrons within the inner shell of the atom can be seen at higher energy losses in the spectrum according to their respective binding energies. This phenomenon gives rise to quantitative EELS which can be used to perform elemental analysis and even track oxidation states.[33] A typical EELS spectrum is shown in Figure: 1.4.

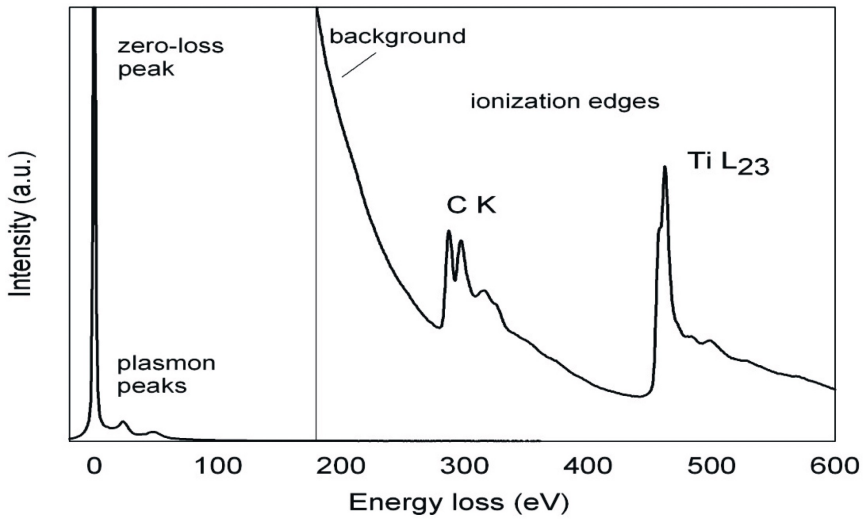


Figure 1.4: A typical electron energy loss spectroscopy (EELS) spectrum. An EELS spectrum of a 20 nanometre (nm) thick titanium carbide sample specimen. This spectrum was recorded in a transmission electron microscope (TEM) equipped with an energy-filtering spectrometer and operating at 200 kiloelectron volts (keV). Reproduced from F. Hofer *et al.*, Fundamentals of electron energy-loss spectroscopy, *IOP Conf. Ser.: Mater. Sci. Eng.*, **109**, (2016), DOI: 10.1088/1757-899X/109/1/012007 with permission from IOP Publishing Ltd..[37]

1.3 The emergence of liquid phase investigations using electron microscopy and its challenges

Building upon the theory of electron optics based on the collective contributions of Thomson, de Broglie, and Busch, Ernst Ruska and Max Knoll established the first TEM in 1931.[38,39] After immense research in the advancement of the field of electron optics and EM, researchers looked for opportunities to study specimens dispersed within solutions in the EM. This of course presented the interesting challenge of ensuring that a liquid placed into a high-vacuum environment did not evaporate immediately upon insertion into the

electron microscope. This was the first barrier for the investigation of liquid phase studies in the EM. The first example of a TEM with the capability to study liquid phase samples came from the development of a differentially pumped environmental chamber by Ernst Ruska in 1942. This instrument utilized differential pumping so that the pressure at the sample region could be as low as 0.3 bar, offering the capability to study hydrated samples. This experimental design for the imaging of liquid phase / hydrated samples is known as an "open cell" TEM method.[40,41] In contrast and in primary focus for this thesis, the "closed cell" TEM imaging method of liquid phase samples relies on dispensing a liquid droplet containing the sample of interest onto a nanofabricated chip and enclosing the solution with a second nanofabricated chip placed on top.

In 1944, the first "closed cell" for EM was created using a platinum substrate and a 60 nm thick nitrocellulose film window membrane by Abrams and McBain (Figure: 1.5).[40,42] Abrams and McBain proposed a suitable design for a "closed cell" for EM which possessed windows which were transparent to the electron beam while also being mechanically strong enough to withstand the vacuum of the microscope without rupturing or allowing liquid to leak through the membrane.[42] To seal two chips together, Abrams and McBain designed the platinum chips with a groove to contain adhesive wax.[42] This early method of NFC engineering did not utilize the instrumental accuracy of modern tools for the nanofabrication of the NFC architecture, however, this early research established the idea that window mem-

branes must balance the requirements of electron transparency and mechanical strength in order for EM experiments to be successful in the liquid phase.

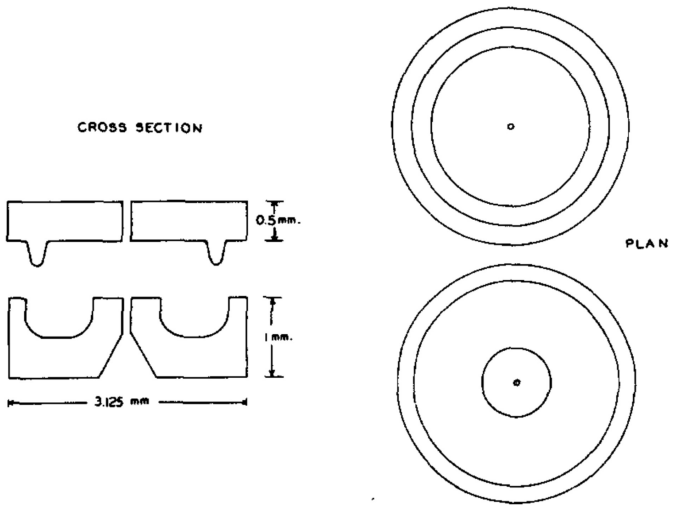


Figure 1.5: The first "closed cell" for electron microscopy (EM). A cross section and plan view of the first "closed cell" utilized by Abrams and McBain to perform liquid phase experiments in the EM. In this pioneering design, platinum was utilized as a substrate, nitrocellulose served as the window membrane material, and the entire assembly was sealed with wax. Reprinted from I.M. Abrams and J.W. McBain, A Closed Cell For Electron Microscopy, *J. Appl. Phys.*, **15**, 607, (1944) with the permission of AIP Publishing.[42]

To further establish the technique of LC-TEM, an alternative technique was needed in order to ensure that individual liquid-cells (LCs) were brought together to form a hermetic seal from the vacuum of the EM and that the window membrane was more resistant to stress while offering greater transparency. Many researchers continued to investigate the EM of liquid samples through the use of differential pumping in environmental scanning electron microscopes (ESEM) until "closed cells" were further developed to improve upon the original design by Abrams and McBain.[38,43] These "closed cells" were developed to

overcome some of the shortcomings of ESEM imaging such as tedious sample preparation requirements.[18]

At the beginning of the 21st century, "closed cell" EM began to evolve significantly. Before "closed cell" technology developed to what it is currently, liquid capsules with polyimide and graphene oxide (GOx) window membranes were designed by a number of research groups for "closed cells" being used in EM.[44,45] These designs were limited to using backscattered electrons (BSEs) to capture processes which occurred near the window membrane surface.[18]

Currently, the most popular "closed cell" design for LC-TEM is the "sandwich" design (Figure: 1.6) in which a liquid sample is enclosed within two solid materials (typically silicon) with transparent window membranes (typically silicon nitride (SiN_x)). This design necessitates the use of a sealant material such as an o-ring or a low outgassing epoxy.[18,43]

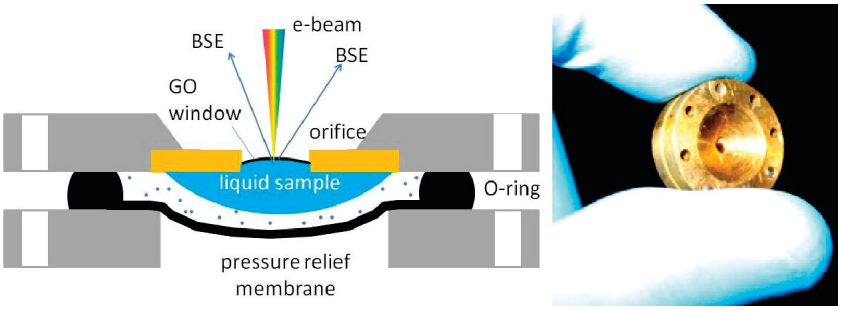


Figure 1.6: A "closed cell" nanofluidic cell (NFC) "sandwich" design for scanning electron microscopy (SEM) in the liquid phase. One of the first "closed cell" designs which used graphene oxide (GOx) as the window membrane material. Reprinted with permission from M. Krueger *et al.*, Drop-Casted Self-Assembling Graphene Oxide Membranes for Scanning Electron Microscopy on Wet and Dense Gaseous Samples, *ACS Nano*, **5**, 12, 10047–10054, (2011). Copyright (2011) American Chemical Society.[45]

The sandwich design is attractive for "closed cell" LC-TEM as evaporation of the liquid inside of the cell can be avoided or at least limited so that the liquid layer remains relatively constant throughout the image collection process. A variety of NFC designs are illustrated in (Figure: 1.7).

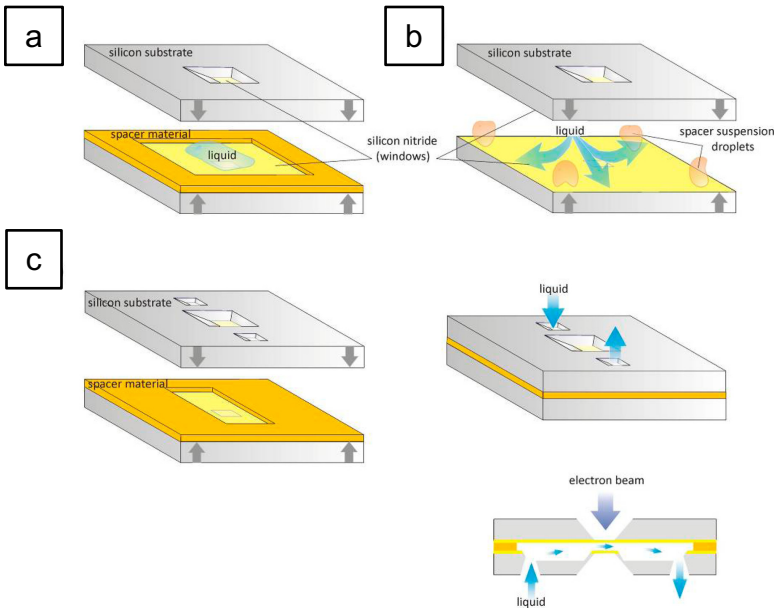


Figure 1.7: Different nanofluidic cell (NFC) "sandwich" designs for liquid-cell transmission electron microscopy (LC-TEM). a) A static NFC design with the spacer material indicated in orange, b) A flow NFC design where the liquid layer thickness is defined through the application of polymer suspension droplets, indicated in orange, dispensed in the corners of the substrates, and c) An NFC with a nanofabricated flow path with inlet and outlet ports implemented into the cell, and where the liquid layer thickness is defined by the spacer material indicated in orange. Reprinted with permission from C. Mueller *et al.*, Nanofluidic Cells with Controlled Pathlength and Liquid Flow for Rapid, High-Resolution In Situ Imaging with Electrons, *J. Phys. Chem. Lett.*, **4**, 14, 2339–2347, (2013). Copyright 2013 American Chemical Society.[45]

While many approaches and designs exist to enclose samples in the liquid phase for imaging in the EM, the production of truly static NFCs appears to be absent on a com-

mercial scale. While some options do exist, generally these designs rely on capillary action to bring the liquid phase sample into the NFC which is a method which has been explored by other researchers.[46] This method leaves much to be desired as the preparation of these NFCs is non-trivial, reproducibility is a significant challenge, and the range of potential sample candidates may be limited. To compensate for the lack of ability of static NFCs on the commercial market and in an attempt to improve the presence of detrimental effects on imaging caused by thick windows or window bulging, researchers have designed a number of unique NFCs. Some of these designs are illustrated in Figure: 1.8. Graphene liquid-cells (GLCs) have become a popular option for the imaging of liquid phase samples, however, these cells encapsulate liquid in a non-reproducible manner.[47] Therefore, although thin liquid layers may be achieved in GLCs for LC-TEM, these experiments are not very reproducible. Other designs such as the micro-well NFC offer additional support for the window membrane to minimize the bulging that the window membrane experiences.[48] This design is intriguing, however, expertise is required in the handling of the graphene films which cover the wells, creating a challenge for achieving reproducibility in experiments.

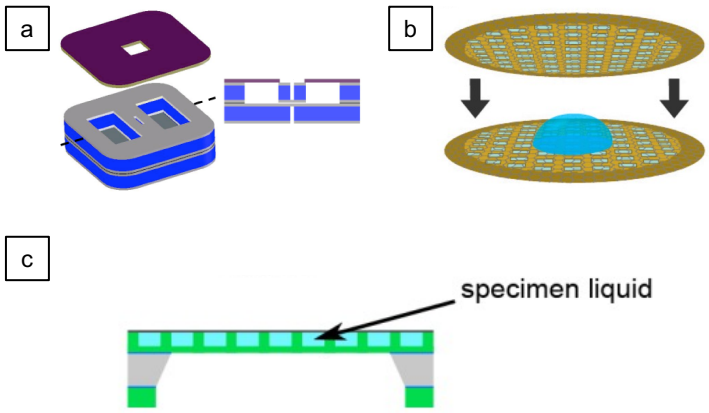


Figure 1.8: Different static nanofluidic cell (NFC) designs for liquid-cell transmission electron microscopy (LC-TEM). a) A static NFC design which is filled by capillary action. The cover (purple) is sealed with an epoxy against the silicon nitride (grey), with wells patterned into the silicon (blue) leading into the viewing area.[46] b) A schematic which illustrates the enclosure of a liquid sample droplet between two copper grids, each covered with a graphene layer. c) A micro-well NFC design where the top layer is composed of graphene (black), the sample liquid (blue) is placed into silicon nitride (green) micro-wells, and the supporting substrate is composed of silicon (grey). Figure a) was reprinted with permission from H. Zheng *et al.*, Observation of Single Colloidal Platinum Nanocrystal Growth Trajectories, *Science*, **324**, 5932, 1309-1312, (2009). Copyright 2009 American Association for the Advancement of Science.[46] Figure b) reprinted from Micron, 149, S. Keskin *et al.*, Verification of water presence in graphene liquid cells, 103109, Copyright 2021, with permission from Elsevier.[47] Figure c) was reprinted with permission from A. Hutzler *et al.*, Unravelling the Mechanisms of Gold–Silver Core–Shell Nanostructure Formation by in Situ TEM Using an Advanced Liquid Cell Design, *Nano Lett.*, **18**, 11, 7222–7229, (2018). Copyright 2018 American Chemical Society.[48]

1.4 Challenges in modern liquid-cell transmission electron microscopy

Expanding on the NFCs presented in the previous section, there are a number of factors which have historically caused issues for researchers when imaging in the liquid phase. One of the initially challenging barriers in LC-TEM was the establishment of hermetic sealing for the NFC assemblies, where the sample, typically assembled in the standard pressure of the laboratory environment, must be reliably sealed in order to prevent sample evaporation to the high-vacuum of the electron microscope. From the early days of liquid phase experiments in the electron microscope, researchers have developed various methods to overcome the hurdles of this non-trivial challenge. From the trialed use of wax in the work of Abrams and McBain,[42] to the utilization of epoxy by Peckys *et al.*,[49] researchers within the LC-TEM community now typically rely on miniature o-rings to form a hermetic seal in the tip of specialized NFC holders as illustrated in Figure: 1.9.[50–52] While the challenge of reliable hermetic sealing has been overcome, two major issues remain as a barrier to the success of an LC-TEM experiment, both of which are factors in achieving reproducibility and sufficient resolution for liquid phase experiments.

One of the ongoing challenges which limit the resolution of images obtained through the technique of LC-TEM is the well-known phenomenon of window membrane bulging

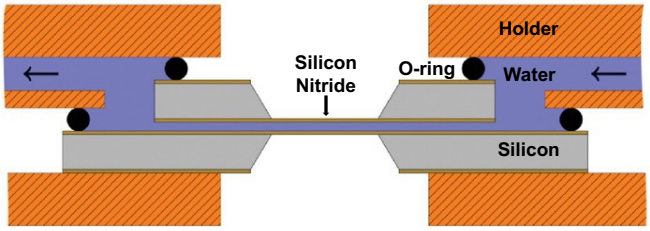


Figure 1.9: A cartoon illustration of how nanofluidic cells (NFCs) are typically sealed within a specialized NFC holder in liquid-cell transmission electron microscopy (LC-TEM). The silicon nitride (brown) coated NFCs (grey) are hermetically sealed within the holder (orange) through the use of specialized miniature o-rings (black). This ensures that the NFC remains hydrated with liquid (typically water as shown in blue) throughout the course of the experiment. Arrows within the liquid indicate that this type of holder design is typically for NFCs built for flow experiments. The spacer is not illustrated here. Reproduced with permission from E. Jensen and K. Mølhave, (2016). Encapsulated Liquid Cells for Transmission Electron Microscopy. In F. Ross (Ed.), Liquid Cell Electron Microscopy (Advances in Microscopy and Microanalysis, pp. 35-55). Cambridge: Cambridge University Press.[53]

(Figure: 1.10) which is a result of assembling an NFC in the standard atmosphere of the laboratory environment only to be later imaged in the high-vacuum environment of the electron microscope. This procedure, which creates a large pressure differential between the interior of the NFC and the interior of the microscope column, is known to lead to apparent liquid layer thicknesses which are one to two orders of magnitude higher than the nominal liquid layer thickness.[5,54,55] The liquid layer thickness is determined through a number of techniques, but primarily through electron energy loss spectroscopy (EELS) as will be discussed in section 2.1.[54,56]

Due to the bulging of the window membrane, (typically made of silicon nitride) and the fact that high-resolution images are only obtainable in the thinnest liquid layer regions, observation of samples in the NFC are often limited to the edges or corners of the window

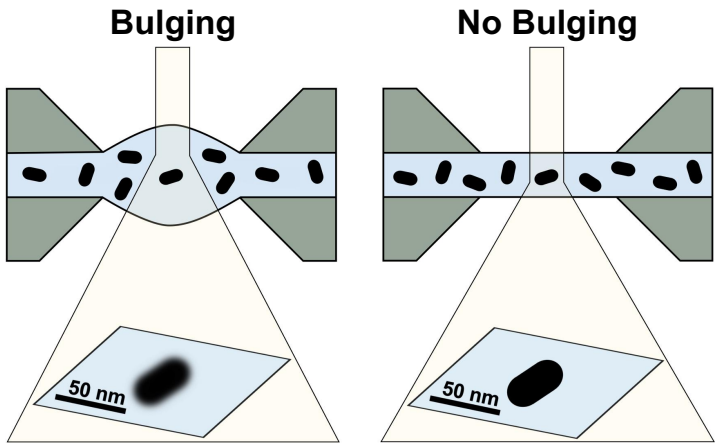


Figure 1.10: A cartoon illustrating how window membrane bulging severely reduces the maximum obtainable resolution in liquid-cell transmission electron microscopy (LC-TEM). Window membrane bulging typically occurs on the order of hundreds to thousands of nanometres, seriously impacting the ability to resolve features of interest in the liquid phase. Reproduced with permission from T. S. Lott *et al.*, Robust Fully Controlled Nanometer Liquid Layers for High Resolution Liquid-Cell Electron Microscopy, *Lab Chip*, **23**, 3217-3225, (2023).[57]

membrane.[58] If high resolution imaging is required, this bulging therefore significantly reduces the viewable area for the acquisition of images and the characterization of dynamic phenomena. This problem is so significant that researchers have had to develop unique but invasive and time consuming procedures such as the electron beam induced generation of gaseous voids and bubbles in the liquid as seen in Figure: 1.11.[59–61]

In addition, given that NFCs are typically assembled in the open laboratory environment, the internal pressure of the NFC assembly is unregulated which can lead to variability in repeat measurements. Furthermore, the design and simply the assembly of conventional NFCs renders them vulnerable to the high possibility of particle contamination in a stan-

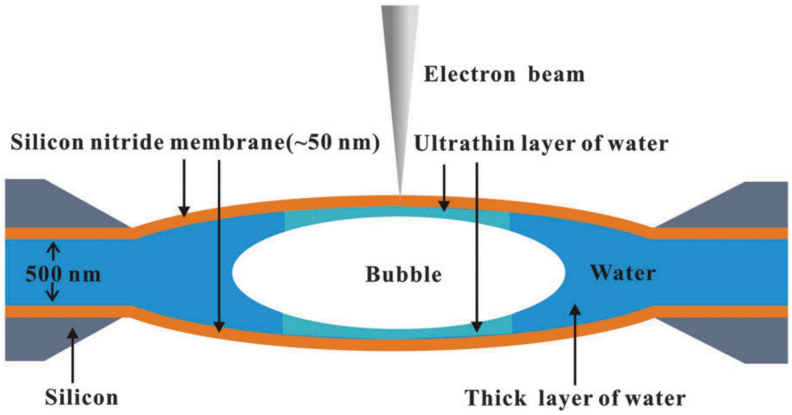


Figure 1.11: A cartoon illustration of deliberate bubble generation for liquid layer thinning in liquid-cell transmission electron microscopy (LC-TEM). Due to window membrane bulging, the liquid layer can be thinned by creating bubbles within the solution. Reproduced from G. Zhu *et al.*, Atomic resolution liquid-cell transmission electron microscopy investigations of the dynamics of nanoparticles in ultrathin liquids, *Chem. Commun.*, **49**, 10944-10946, (2013) with permission from the Royal Society of Chemistry.

dard laboratory environment which lacks high-efficiency particle absorbing (HEPA) filters. Class 9 (standard laboratory air), the lowest International Organization for Standardization (ISO) standard of cleanroom environments can contain no more than 293,000 5 micrometre (µm) diameter particles / m^3, 8.3 million 1 µm diameter particles / m^3, and 35.2 million 0.5 µm diameter particles / m^3. Particles with diameters smaller than those listed above are classified as being present in a very high particle concentration and therefore for this class of cleanroom, these particles are left unquantified.[62] When assembling an NFC, the typical space left for liquid is on the order of hundreds of nanometres. Therefore, when assembling an NFC in the standard laboratory environment there is a substantial risk for compromising the spacer of the NFC, causing the true spacer which defines the liquid layer

thickness, to be substantially higher than the nominal spacer which is produced with high accuracy through nanofabrication. Thus, if one is concerned with maintaining a high level of accuracy and reproducibility in the defined liquid layer thickness, one must consider the environment in which the NFC is assembled and a class 9 environment is therefore insufficient for the assembly of these devices. One should therefore at the very least prepare NFCs in a portable fume hood with an installed HEPA filter to minimize the chance of the contamination of the device prior to an experiment.

As the technique of LC-TEM continues to evolve, advancements in the development of NFC devices will be necessary to improve the imaging capabilities and resolution of dynamic processes occurring in *in-situ* and *in-operando* environments. A major challenge which remains is improving the window membrane material for the NFC devices. Although bilayer graphene is currently available for imaging to provide roughly 98 % transmission of the electron beam at 100 kV, the production of these films is not as refined or widely available as the silicon nitride film nanofabrication processes previously discussed in section 2.2.[63] In addition, graphene membranes tend to wrinkle and fold around the sample solution which ultimately causes limitations in the usable area of the window membrane due to an inability to clearly resolve the specimen in areas of window membrane deformation.[63] Silicon nitride films are capable of offering high-transmission ($\sim$ 75 %) at 200 kV when the film thickness is less than 10 nm. In addition, these films are quite robust, as a square

silicon nitride membrane of 100×100 μm^2 which has not been optimized to reduce bulging is remarkably able to withstand pressures of approximately 0.5 atm.[63,64]

It is therefore evident that additional solutions in window membrane bulge reduction and precisely nanofabricated spacer materials need to be developed in order to have precise control of the liquid layer thickness. This thesis presents such a solution to achieve highly controlled liquid layer thicknesses with a simplified and high-throughput NFC assembly approach. In the next chapter, a methodology for conducting experiments in LC-TEM is outlined, a brief overview of nanofabrication for conventional NFC devices will be given, and the developed instrumentation to achieve highly controlled liquid layer thicknesses will be introduced.

Chapter 2

Methodology and instrumentation development

In this chapter, details will be provided on the methodology of conducting electron microscopy in LC-TEM, common techniques involved to produce NFCs will be discussed, and the developed instrumentation which resolves long-standing challenges within the LC-TEM community will be outlined.

2.1 Methodology for conducting electron microscopy in the liquid phase

Using electrons to image solid samples is a challenging task due to the need for a high or ultra-high vacuum environment and the incorporation of electromagnetic control of the electron beam. Even more challenging is the prospect of imaging solid samples immersed in the liquid phase environment where many additional challenges exist for the successful imaging of sample specimens. The use of NFCs has opened the door to the exploration of these liquid phase processes, however there are many factors that must be considered in order for an electron microscopy experiment in the liquid phase to be successful. In this section, a methodology which addresses the challenges and considerations for a typical electron microscopy experiment in the liquid phase will be discussed.

2.1.1 Electron transmission

One of the main challenges in performing electron microscopy imaging in the liquid phase as discussed previously is the uniform formation of thin liquid layers throughout the NFC. The act of surrounding the specimen of interest in a liquid medium in itself is contrary to the principles of conventional TEM which requires dry ultrathin samples. The addition of a liquid medium introduces more material that electrons passing through the specimen

will have to traverse in comparison to a dry sample. The addition of this liquid introduces more opportunities for multiple scattering events to occur during the process of imaging.[65] As a result, obtaining data with the necessary resolution for the study of interest can be a challenge in the liquid phase. This challenge is further complicated by the inability to obtain uniform liquid layer thicknesses within the NFC. The contribution of liquid water to the loss of transmission of the electron beam can be appreciated by relating the transmission of the electron beam to the total mean free path and thickness of the material as seen in Equation: 2.1 - Equation: 2.3.[57,63,66]

$$\sigma_{tot} = 18\frac{\sigma_{el}}{Z} + \sigma_{el} \tag{2.1}$$

$$\Lambda_{tot} = \frac{1}{\Sigma\frac{N_A\rho}{M}\left(n_i\sigma_{tot,i} + n_j\sigma_{tot,j} + ...\right)} \tag{2.2}$$

$$T = e^{\frac{-t}{\Lambda_{tot}}} \tag{2.3}$$

where σ_{tot} is the total scattering cross section of a given atom which composes a material, σ_{el} is the total elastic scattering cross section of a given atom which composes a material, Z is the atomic number of a given atom which composes a material, Λ_{tot} is the total mean free path of the material, N_A is the Avogadro constant, ρ is the density of the material, M

is the molecular mass of the material, n is the number of moles of a given element in the material, T is the transmission of the electron beam, and t is the thickness of the material.

When considering the impact that a specific film has on obtaining high transmission data in the electron microscope, from studying Equation: 2.1 - Equation: 2.3 it becomes evident that the choice of a low density, low mass material must be balanced with nanofabrication capabilities and membrane thickness optimization. Figure: 2.1 illustrates that high-quality silicon nitride membranes offer an electron transmission percentage comparable to 5 nm of amorphous carbon. These silicon nitride thin-films are reliably attained through established nanofabrication techniques, a benefit which is not offered by current graphene and amorphous carbon technologies for NFC production.

Thus, to perform imaging with high spatial resolutions, one should use an optically transparent thin membrane material with sufficient strength such as thin-film silicon nitride. Graphene and amorphous carbon films are also good options to perform imaging, however these materials currently lack engineering processes which are scalable as previously mentioned. In addition, the formation of folds and wrinkles within the support film is highly prominent due to the nature of its production and application to enclose samples.[63]

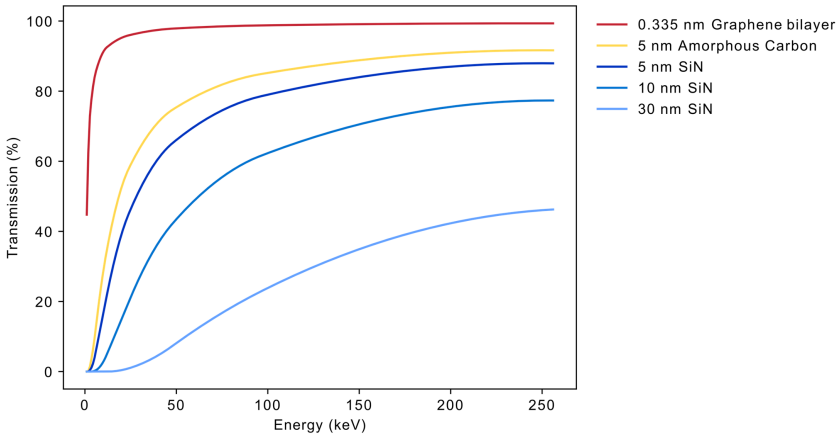


Figure 2.1: Theoretical electron transmission through various materials commonly used for liquid-cell transmission electron microscopy (LC-TEM). The transmission of total electrons (both inelastic and elastic) through graphene, amorphous carbon, and various thicknesses of silicon nitride films as indicated. Calculations were performed with total scattering data obtained by Riley *et al.* and fit with an exponential function across nominal acceleration voltages.[67] This figure can be reproduced using the code available at https://github.com/UeIL-Waterloo/Electron_transmission. Reproduced with permission from N. Shaw, Improving Biospecimen Imaging in Liquid Phase Electron Microscopy, MSc Thesis, University of Waterloo (2023).[68]

2.1.2 Determining the liquid layer thickness with EELS

In this thesis, EELS was utilized to characterize the liquid layer thickness in the assembled NFCs. Through EELS the liquid layer thickness may be measured through the commonly used log-ratio method shown in Equation: 2.4 - Equation: 2.10.[33,34]

$$\frac{t}{\lambda} = ln\left(\frac{I}{I_0}\right) \tag{2.4}$$

$$\lambda \approx \frac{106FE_0}{E_m ln\left(\frac{2\beta E_0}{E_m}\right)} \tag{2.5}$$

$$F = \frac{1 + \frac{E_0}{1022}}{\left(1 + \frac{E_0}{511}\right)^2} \tag{2.6}$$

$$E_m = 7.6 Z_{\text{eff}}^{0.36} \tag{2.7}$$

$$Z_{eff} = \frac{\Sigma_i f_i Z_{\text{i}}^{1.3}}{\Sigma_i f_i Z_{\text{i}}^{0.3}} \tag{2.8}$$

$$\frac{t_{total}}{\lambda_{total}} = \frac{t_w}{\lambda_w} + \frac{t_{SiN_x}}{\lambda_{SiN_x}} \tag{2.9}$$

$$t_w = \left(ln \left(\frac{I}{I_0} \right)_{total} - ln \left(\frac{I}{I_0} \right)_{SiN_x} \right) \times \lambda_w \tag{2.10}$$

where t is the thickness of the material interacting with the electron beam, λ is the inelastic mean free path (IMFP) of the material interacting with the electron beam, I is the intensity contribution of all of the electrons in the electron energy loss spectroscopy (EELS) spectrum, I_0 is the intensity contribution of the electrons which can be considered to have lost no energy to make up the zero-loss peak (ZLP), F is a relativistic factor, E_0 is the energy of the accelerated electron in kiloelectron volts (keV), E_m is the average energy loss in electron volts (eV), β is the collection angle of the EELS spectrometer, Z_{eff} is the effective atomic number of the material which is being investigated, f_i is the atomic fraction

of the atoms which make up the material which is being investigated, Z_i is the atomic number of the atoms which make up the material which is being investigated, and here the subscripts *total*, w, and SiN_x refer to the corresponding values for the NFC assembly (including water), solely water, and solely the silicon nitride membranes, respectively.

To quantify the thickness of the liquid layer within an NFC, two EELS spectra are acquired to perform calculations according to Equation: 2.10. One EELS spectrum is acquired for an empty NFC, devoid of liquid and another is acquired for an NFC with liquid contained within a predefined spacer. Once data have been collected for both of these NFCs, the log-ratio intensity of the NFC containing liquid is subtracted by the log-ratio intensity of the empty NFC. Since the inelastic mean free path (IMFP) of liquid water can be calculated with knowledge of the electron microscope instrument parameters according to Equation: 2.5 - Equation: 2.8, the thickness of the water layer can be determined for an NFC filled with water. For the purposes of liquid layers calculated in this thesis, the Lenz model was utilized for the calculation of Z_{eff}.[34] In addition, it should be clarified that the IMFP of water utilized in these calculations may be underestimated by roughly 50 % as noted in the recent work of Yesibolati *et al.*.[69] Since this method relies on parameterization of the inelastic mean free path in terms mean atomic number of the sample specimen, the incident electron energy, and the collection angle of the EELS spectrum in order to determine the sample thickness, an accuracy of +/- 20 % for inorganic specimens has been

estimated, although, this may be higher for organic specimens.[34] Therefore, the presented calculations must be viewed as approximations to the liquid layer thickness.

2.1.3 Radiolysis in LC-TEM

Another unique challenge which exists in LC-TEM is the presence of radiolysis effects which result from the high-energy reducing beam of the electron microscope interacting with the liquid which is immersing the sample of interest. Radiation damage is well known to exist in conventional electron microscopy techniques, where the radiation damage imposed on a sample specimen is known to be dependent on the dissipated energy over the illuminated volume which is dependent on the amount of time that the sample specimen is irradiated for. Primarily, damage is due to inelastic scattering in which the transferred energy is dissipated either as heat or results in the scission of bonds within the sample specimen. Although thermal diffusion, evaporation, and reactions with radicals may take place in samples under the irradiation of the electron beam, this behaviour is even less trivial in liquid immersed samples.[21] In LC-TEM experiments, much attention must be paid to the electron dose, otherwise the irradiation can result in deleterious effects on the sample triggered by the electron beam interacting with the surrounding liquid.[70–73] In addition to the generation of highly reactive radicals, the generation of bubbles, precipitation of salts, the influence of the electron beam on redox chemistry, the rupturing of biological

membranes, and the aggregation of colloidal materials are all phenomena which may take place in a typical LC-TEM experiment if the electron dose is not precisely controlled.[73]

2.1.4 Carbon contamination in LC-TEM

Due to the well known phenomenon of carbon contamination in the microscopy community, preventing the electron beam initiated deposition of carbon is an important consideration to achieve accurate thickness measurements through EELS.[74,75] Carbon contamination in the electron microscope can be avoided during the course of an EELS line scan by plasma / UV-ozone cleaning the NFCs and the NFC sample holder prior to the experiment as seen in Figure: 2.2.[76,77] Plasma / UV-ozone cleaners effectively remove organic layers that assemble onto surfaces in the regular laboratory environment. Typically the plasma cleaner utilized in this thesis was operated at 30 watts (W) or 50 W with a mixture of hydrogen, neon, and argon gases. Upon exposure of the surfaces in the plasma for two minutes, the previously hydrophobic surfaces are rendered hydrophillic with the removal of the organic layer.

In order to further prevent carbon build-up and contamination of the sample specimen during EELS measurements, the region of interest was found using a defocused STEM probe ($\sim$ 100 μm of defocus). Defocusing of the STEM probe was found to significantly reduce carbon contamination without influencing the interpretation of the EELS spectra.

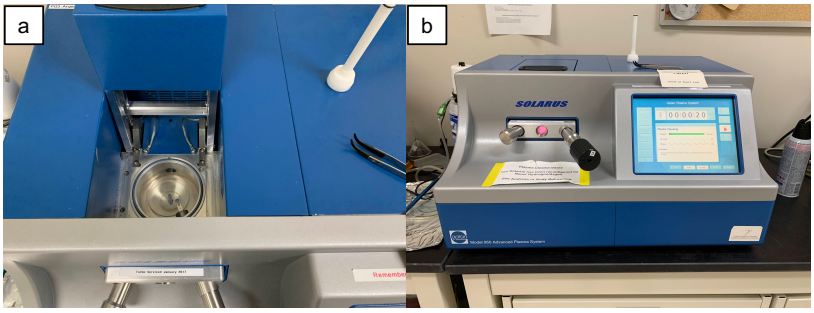


Figure 2.2: A plasma cleaner used for the preparation of nanofluidic cells (NFCs) and sample holders for liquid-cell transmission electron microscopy experiments. a) A top view of a Gatan Solarus plasma cleaner with the sample compartment open. b) Running a plasma cleaning process in the Gatan Solarus. The plasma (pink) is generated in a mixture of hydrogen, neon, and argon gas with 50 Watts (W) of power for two minutes.

2.1.5 Electron dosage in LC-TEM

The calculation of the electron dose on the imaged specimens presented in this thesis was conducted via standard methods in the literature.[78] The electron dose is calculated according to Equation: 2.11.

$$D_f = \frac{i_e t_f}{eA} \tag{2.11}$$

where D_f is the electron dose per frame (electrons per square angstrom (Å) per frame), i_e is the calibrated beam current in amperes (A), t_f is the frame time in seconds, e is the elementary charge of an electron in coulombs, and A is the imaging area in $Å^2$ which is calculated by the square area of the image in STEM mode and from the beam diameter in TEM mode.

This equation indicates that as the magnification of the sample image is increased, the dose per frame is increased substantially as the area in which the electron flux is spread is severely reduced. Thus, it is important to only utilize magnifications which are necessary to achieve the resolution of features which one desires to resolve. Furthermore, since the image metadata will typically include the frame time of the image as well as the area over which the image was taken, importantly one must ensure that a method to measure the beam current is utilized so that the calibrated beam current is correctly collected for the image. It is therefore imperative to calibrate and determine i_e for a wide range of magnifications prior to imaging in the electron microscope. This is accomplished via measurements taken with the same beam conditions with a Faraday cup or a calibrated fluorescent screen.

2.2 Considerations for the design and nanofabrication of "closed cell" sandwich devices for LC-TEM

There are a number of companies which currently offer commercial solutions for researchers looking to conduct LC-TEM experiments. Many of these companies design their nanofabrication processes around the creation of "closed cell" sandwich devices due to the well-known nanofabrication techniques necessary to produce these devices. Throughout this section, the nanofabrication of a standard "closed cell" sandwich device will be outlined

and discussed. The important features of the nanofabrication process will be investigated with detail.

Some initial considerations one must consider when manufacturing a product are the requirements of the device, the target market of the device, and the capability to manufacture the device with a finite amount of resources. This leads the manufacturer to consider the materials which will be best suited for the final product that they are looking to design. For example, the complexities involved with manufacturing NFCs with GOx windows may be suitable for the researcher who requires small quantities of devices for their experiments, while the same technology may not be feasible for a company or facility looking for a reliable large-scale product using readily available nanofabrication equipment. Much of the nanofabrication involved in the production of NFCs is done using silicon substrates and window membrane materials which are convenient and reliable such as polyimide and SiN_x.

Silicon substrates have long been the most common materials for nanofabrication processes due to the large natural abundance of silicon and the ease of control in growing large silicon crystals, resulting in an economical and effective solution for silicon wafer manufacturing.[79] More importantly, the native oxide of silicon, silica (SiO_2), is easily formed as a passivation layer upon silicon to act as a diffusion barrier for dopant species. Furthermore, silica may be preferentially etched from silicon with high selectivity. Due to the lack of

such an effective passivation layer, many alternative substrates such as germanium oxide (GeO_2) are less suited for the stringent nanofabrication processes necessary to fabricate devices such as integrated circuits (ICs).[79] Therefore, although there is progress in developing substrates beyond the era of silicon such as silicon hybrid materials and carbon based materials like graphene, silicon currently remains the preferred substrate choice for nanofabricating NFCs.

The substrate must be prepared for subsequent nanofabrication steps which involve multiple deposition and etching cycles. A common practice in preparing substrates for effective nanofabrication processing is to first perform a Radio Corporation of America (RCA) cleaning process on commercially supplied wafers. The RCA cleaning process was originally developed by Werner Kern and David Puotinen of RCA Laboratories in 1970. This cleaning procedure was founded on the idea that reliable and effective semiconductor technology must be fabricated with minimal contamination during the processing steps in order to increase the stability and reproducibility of device characteristics.[80]

Foundationally, the cleaning process focuses on removing molecular, ionic, and atomic contaminants from the wafer surface. Each contaminant poses a unique threat to the quality of the final product such as how organic molecular contaminants can make a device surface undesirably hydrophobic, ionic contaminants can cause drift of ionic species under the influence of an electric field, or how atomic contaminants can significantly influence sur-



Figure 2.3: A nanofabrication chemical wet bench typically used for the Radio Corporation of America (RCA) process. Reprinted with permission from G. Fisher *et al.*, Silicon Crystal Growth and Wafer Technologies, *Proc. IEEE*, **100**, 1454-1474, (2012). Copyright © 2012 IEEE.[79]

face conductivity.[80] To ensure that the wafer surface has been sufficiently cleaned, organic residues due to molecular contamination which mask underlying contaminants must be removed from the surface first, followed by ionic and atomic contaminants. Typical residues from wafer-polishing operations are removable through the use of organic solvents.

The RCA process is a multi-step cleaning process which is conducted by utilizing wet chemical cleaning as seen in Figure: 2.3. The original procedure outlined by Kern and Puotinen recommended the following solution formulations and conditions:[80]

i) Standard Clean 1 (SC-1: A 5:1:1 to 7:2:1 parts by volume solution of deionized water (H_2O): hydrogen peroxide (H_2O_2) (30 %, unstabilized): ammonium hydroxide (NH_4OH)

(27 %) is prepared to remove organic contaminants. NH_4OH provides strong solvation of the organic contaminants (as well as metals such as copper, silver, nickel, cobalt, and cadmium) present on the wafer surface while the oxidative strength of hydrogen peroxide effectively strips organic contaminants away from the wafer surface. The wafer should be submerged in the solution (preheated to 75 – 80 °C) for 10 – 20 minutes. The wafer should then be rinsed in deionized water before proceeding to the next step.

ii) Standard Clean 2 (SC-2: A 6:1:1 to 8:2:1 parts by volume solution of deionized H_2O: H_2O_2 (30 %, unstabilized): hydrochloric acid (HCl) (37 %) is prepared to remove any heavy metals which may be present on the wafer surface as well as to form soluble complexes with the resultant ions for the prevention of displacement replating from the cleaning solution. As done for the SC-1 cleaning process, the wafer should be submerged in the described solution (preheated to 75 – 80 °C) for 10 – 20 minutes. The wafer should then be rinsed in deionized water before drying with filtered dry nitrogen or inert gas.

This cleaning protocol was noted to be remarkably effective at removing hydrophobic organic contaminants as well as organic contaminants from silicon wafer surfaces through the use of water spray tests and desorption quantification using radioactive tracers.[80] However, to improve the cleaning process, Kern noted in a 1990 review article that the SC-1 treatment can lead to the entrapment of trace impurities within a hydrous oxide film. Thus, Kern recommended a 15 second immersion in a 1:99 parts by volume solution of hydroflu-

oric acid (HF): deionized H_2O. This intermediary step should be conducted with careful consideration as the resultant surface from HF cleaning is highly reactive and attractive to particles.[81]

A final remark on the RCA cleaning process concerns the equipment used to conduct these cleaning processes. In many cleanrooms, there may be allocated baths which are carefully monitored at wet benches to ensure optimal purity of the cleaning solutions. Otherwise, the immersion procedures should be conducted with Teflon wafer carriers in vessels made from fused silica rather than Pyrex in order to prevent the leeching of aluminum, boron, and other alkali metals into the SC-1 and SC-2 cleaning solutions.[81] The HF immersion process must be conducted in Teflon or polypropylene vessels.

After one has ensured that the substrate has been decontaminated, a thin film of the material which will serve as the window membrane must be deposited onto the wafer surface. This film is typically silicon nitride due to a number of its favourable properties such as a high Young's modulus, its ease of implementation for subsequent nanofabrication steps, and relative chemical inertness which is favourable to allow for the investigation of a wide variety of chemical environments.[53,63]

Using a low pressure chemical vapour deposition (LPCVD) furnace, the pre-processed silicon wafers are typically coated with silicon nitride on both sides of the wafer.[63] To achieve this coating, silicon nitride forms on the surface of the silicon substrate in a stoi-

chiometry which is dependent on the ratio of the gas mixture (dichlorosilane (SiH_2Cl_2), and ammonia (NH_3)) within the furnace. Typical processes occur within a temperature range of 700-900 °C and at a pressure below 1 Torr.[82] These general parameters have been discovered to offer good results in terms of thickness uniformity, consistency in silicon nitride composition, and conformal step coverage in the resultant processed wafers.[82] Mechanical properties of the deposited films may be tuned by adjusting the gas mixture ratios which affect the stoichiometry of the deposited silicon nitride film. For example, Si_3N_4 films possess a large tensile residual stress and may be actively selected for in the deposition process if an excess of NH_3 is utilized in the gas mixture.[82]

A typical deposition process may have the following conditions: 140 standard cubic centimetres per minute (sccm) of NH_3, 50 sccm of SiH_2Cl_2, a furnace temperature of 800 °C, and a pressure of 136 mTorr.[83] The deposition rate of silicon nitride for a process such as this may be around approximately four nanometres per minute and thus the process should be setup to deposit a desired thickness which is typically of tens to hundreds of nanometres.[83] The mechanism of the generation of silicon nitride from the gas mixture has been investigated through multiple studies.[84,85] Briefly, the process can be appreciated first by considering a silicon substrate surface which is hydrogen terminated after the rigorous cleaning processes discussed previously.[86] The dichlorosilane reactive intermediate ($SiCl_2^{\ddagger}$) which is formed from the interaction of SiH_2Cl_2 and NH_3 gas attacks the Si-H and N-H

bonds which exist on the substrate surface. This reaction causes the formation of Si-N and Si-Si bonds to form a SiH_3 terminal species after the elimination of HCl. This newly formed structure can then react with NH_3 again to form more Si-N bonds, thus extending the Si-N bonding network to generate the desired silicon nitride film.[87]

Now that the silicon nitride film has been prepared on the substrate surface, one can now begin to consider the features which one wishes to create on the wafer. To accomplish precise patterning in the wafer material one can utilize ultraviolet (UV) photolithography in which a photoresist compound (consisting of a photoactive component, a resin, and a solvent) is exposed to UV light or near-UV light to either increase the solubility (positive resist) or decrease the solubility (negative resist) of the exposed photoresist material to a corresponding developer solution. For the purposes of this discussion, the process of photolithography will be outlined with respect to positive photoresists.

One must ensure that the photoresist being used has a variety of desired properties to effectively be utilized in the process of producing the desired device. These properties include but are not limited to high solubility in a highly selective solvent, strong adhesion to the desired substrate, adequate UV absorption, and a balance between contrast and sensitivity.[88] Figure: 2.4 illustrates a simplified schematic of the UV photolithography process. Shown in this schematic is the application of photoresist, its exposure to UV light, and its dissolution via a developer solution.

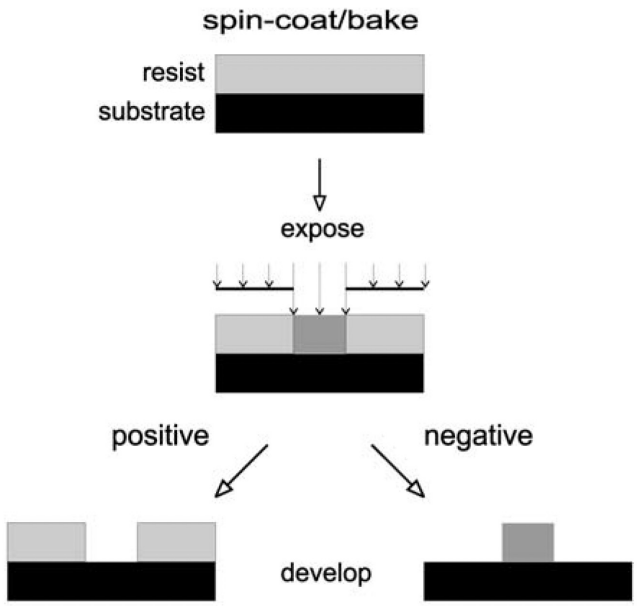


Figure 2.4: A simple photolithography process. Adapted from H. Ito, Chemical Amplification Resists for Microlithography. In: Microlithography · Molecular Imprinting., *Adv. Polym. Sci.*, **172**, (2005) with the permission of Springer Nature. https://link.springer.com/chapter/10.1007/b97574.[88]

To develop patterns through photolithography, the g-line (436 nm) and i-line (365 nm) light sources of mercury arc lamps have been utilized for many years. For example, the i-line technology has utilized diazonaphthoquinone (DNQ)-novolac resists for many years where the photoactive compound is DNQ and the resin material is novolac.[88] Upon exposure to the i-line source, the DNQ compound will form a carbene which is highly reactive and susceptible to undergo a Wolff rearrangement before reacting with water present within the photoresist mixture to generate an indenecarboxylic acid. The formation of this acidic compound from DNQ allows the exposed regions of the photoresist to dissolve quickly in a basic developer solution while the novolac, which serves as a binder, provides high dry

etch resistance, and thermal flow resistance.[88] Figure: 2.5 illustrates the photo-reactive behaviour of DNQ upon exposure to an i-line light source.

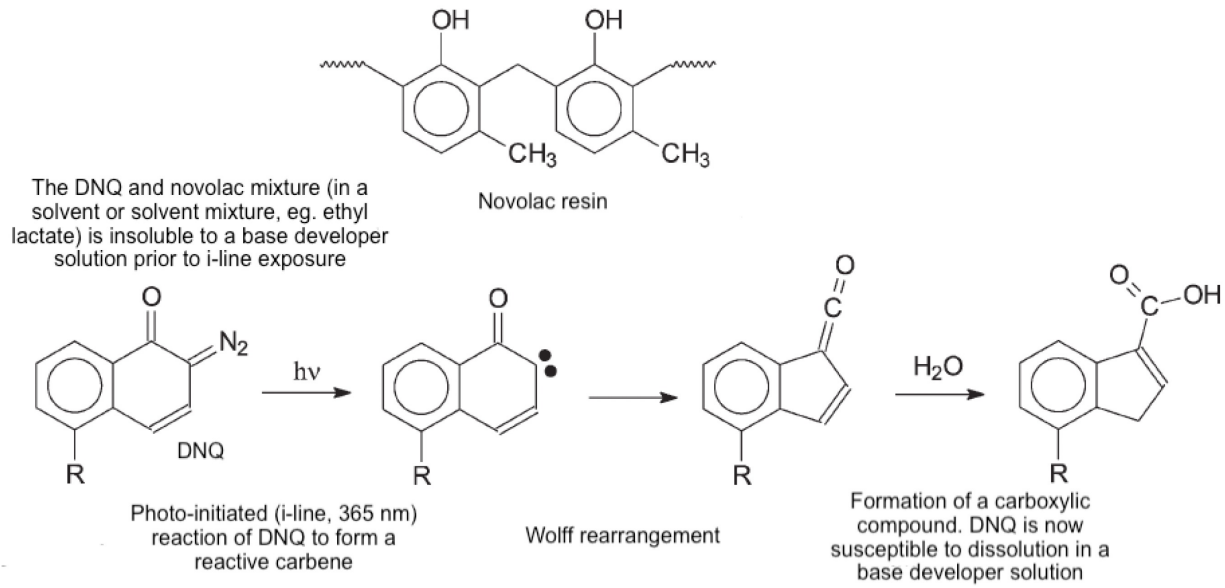


Figure 2.5: The process of exposure for diazonaphthoquinone (DNQ)-novolac based photoresists. The insoluble (to base developer) diazonaphthoquinone (DNQ)-novolac resin becomes soluble (to base developer) in the regions of the photoresist film which were exposed to i-line light (365 nm). Adapted from H. Ito, Chemical Amplification Resists for Microlithography. In: Microlithography · Molecular Imprinting., *Adv. Polym. Sci.*, **172**, (2005) with the permission of Springer Nature. https://link.springer.com/chapter/10.1007/b97574.[88]

As a practical example, the Shipley 1800 series of resists are popular for g-line (436 nm) exposure. More specifically, if one was looking to spin-coat Microposit® S1813® photoresist onto a wafer coated with silicon nitride they would take their wafer and the photoresist to a spin-coater machine and cover roughly 70 % of the surface of the wafer with photoresist in an organized manner (starting from the centre of the wafer) with the wafer vacuum sealed to a spin-coater chuck.

After ensuring that the photoresist was carefully placed into the spin-coater machine, one would then set the spin-coater machine to run the coating process, in which the spin-coater chuck is rotated at a few thousand revolutions per minute (rpm). Refinement and testing of this process is necessary to ensure that the photoresist is evenly coated during the acceleration and deceleration cycles of the spin-coating process. Typically, one could expect a photoresist thickness on the order of a few micrometres.[89] After finishing the coating process, soft-baking (115 °C for 60 seconds) of the photoresist on a hotplate will improve the adhesion of the photoresist onto the wafer surface. Additional baking protocols are possible to improve the quality of the spin-coating process but will not be elaborated upon here. Now that the photoresist has been evenly coated onto the wafer surface, the wafer is then ready for exposure under the g-line with either a photomask or maskless aligner to carefully ensure that only the desired features are exposed. Techniques such as optical proximity correction ensure that effects due to diffraction do not detrimentally impact the sharpness of patterned features during exposure. For the exposure process, the recommended fluence for Microposit ® S1813 ® photoresist is 150 mJ / cm^2 within a photolithography system. This is the energy density which ensures that the photoresist which has been coated onto the wafer surface has been sufficiently exposed to initiate the formation of carboxylic groups in the photoresist (such as the case with DNQ-novolac resists). After completing the exposure process, the wafer is ready to be developed in order

to dissolve the exposed photoresist. For example, for the Microposit ® S1813 ® photoresist, a base developer known as Microposit ® MF-321 ® developer may be utilized through which the exposed wafer is immersed in the developer for 40-60 seconds and subsequently rinsed in deionized water for a comparable period of time.[90] The wafer has now been successfully developed and the photoresist has been removed from the area exposed to the photolithography light source. Specifically, for the nanofabrication of NFCs, this means that the photoresist has been removed from areas in which the researcher is looking to remove silicon nitride for the development of the window membrane. Additional features such as the spacer material and pocket for the o-ring may be developed at a later stage in the nanofabrication process. The next point of discussion will shift to the processes and considerations necessary to expose the silicon substrate surface beneath the silicon nitride and subsequently form the window membranes which will be transmissive to the electron beam in the electron microscope.

Reactive ion etching (RIE) is an anisotropic etching process which is used to remove substrate and thin-film materials through a radio frequency (RF) induced plasma discharge process in which ionic and radical species are generated from etching gases in a low pressure chamber. In RIE, both chemical etching and physical etching processes occur on the wafer surface where chemical reactions between the etchant and target species are enhanced by the bombardment of the target material with ionic species to promote selective anisotropic

etching.[91] RIE achieves an anisotropic etching profile by increasing the etch rate of the target material along the path of the ion bombardment; for this reason, RIE is known as an ion enhanced etching (IEE) process. Although, the physical etching process alone does not substantially etch the target material, the bombardment of ions enhances the removal of the target material by weakening the underlying lattice structure and by releasing byproducts which form on the surface of the target material due to adsorption of etchant species.[91]

The Bosch process is an example of a common etching method to achieve high anisotropy and highly vertical etch profiles. This is typically accomplished through the use of the inductively coupled plasmas of sulfur hexafluoride (SF_6) and octafluorocyclobutane (C_4F_8) gases injected in an alternating sequence into the chamber. SF_6 serves as the etching gas while C_4F_8 deposits onto the target material surface and acts as a passivating layer.[92] Figure: 2.6 illustrates the Bosch process for anisotropic deep silicon etching. Since the photoresist remaining from the spin-coating process is not very selective to etching (as mentioned previously when discussing novolac's resistance to dry etching), the photoresist serves as a mask to protect the material beneath it. For the nanofabrication of NFCs, the RIE process is utilized to remove the silicon nitride in the region where the window membrane will be formed. With the silicon nitride removed, potassium hydroxide (KOH) etching can be utilized to remove the silicon substrate material at a 54.7 ° angle to form the window material. KOH etching will be discussed later in this section of the thesis.

Based on the parameters used, the nitride to silicon etch rate can range from 5:1 to 50:1.[91]

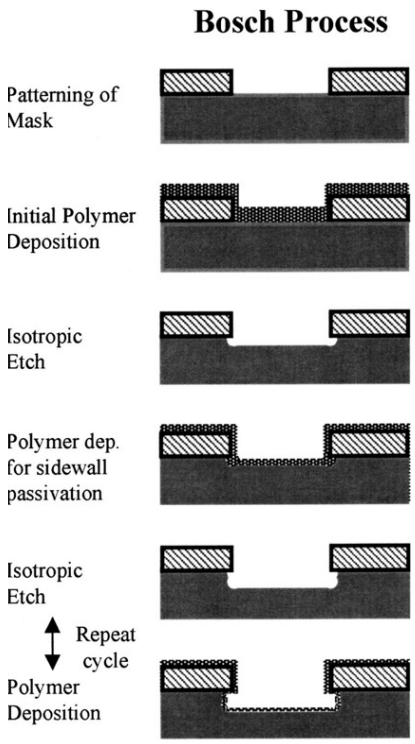


Figure 2.6: A diagram showing the schematic cycling of etching and passivating gases during the Bosch process. Reprinted with permission from C.B. Labelle *et al.*, Investigation of fluorocarbon plasma deposition from c-C_4F_8 for use as passivation during deep silicon etching, *J. Vac. Sci.*, **22**, 2500, (2004). Copyright 2004, American Vacuum Society.[92]

Upon completion of the RIE process, the silicon nitride should be completely removed from the location where the photoresist was exposed during the photolithography process. Before the KOH etching process can be started, the photoresist must first be stripped from the wafer. To accomplish this removal, a variety of methods may be utilized based on the type of photoresist and the baking processes utilized in adhering the photoresist

to the wafer surface. One such example are removal solvents composed of N-methyl-2-pyrrolidone (NMP) such as Remover PG from MicroChem Corporation. The supplier recommends this photoresist for removing g-line, i-line, and deep UV photoresists. The removal of photoresist occurs through the use of multiple baths as follows:[93]

i) Immerse the wafer in a bath of undiluted Remover PG at temperatures between room temperature and 80 °C to remove the bulk of the photoresist. Agitate the wafer as necessary to remove photoresist.

ii) Immerse the wafer in a second bath of undiluted Remover PG at temperatures between room temperature and 80 °C to remove residual photoresist. Agitate the wafer as necessary to remove photoresist.

iii) Immerse the wafer in a bath of isopropyl alcohol (IPA) at room temperature to ensure that no residual photoresist remains on the surface of the wafer. Agitate the wafer as necessary to remove photoresist.

iv) Rinse the wafer with deionized water before blow drying the wafer with filtered dry nitrogen.

In addition to this wet-chemical photoresist removal process, the photoresist may also be removed using an oxygen plasma source. This is also a suitable method of selectively removing the photoresist as exposed silicon and silicon near the photoresist surface is

oxidized and thus etch resistant to the oxygen plasma.[94]

With the photoresist removed, the anisotropic etching process of the silicon substrate may be completed through the use of a KOH solution. The concentration and the temperature of the KOH solution must be modified very accurately to ensure that the etching process occurs optimally to have high preference for the (100) plane of the silicon wafer substrate while also ensuring that the etching process occurs at an optimal rate for nanofabrication. Over a range of concentrations from 10-60 % for aqueous KOH solutions, Seidel *et al.* observed that the etch rate ratio of the crystalline silicon orientations of <110>:<100>:<111> varied from 50:30:1 at 100 °C to approximately 160:100:1 at room temperature.[95] Furthermore, they also discovered that the silicon etch rate could approximately be described by Equation: 2.12 below.

$$R = k_0[\mathrm{H_2O}]^4[\mathrm{KOH}]^{1/4}e^{Ea/kT} \tag{2.12}$$

where the rate constant (Si <100>), k_0 = 2480 micrometres (µm) / hour (h) (moles / litre (L))$^{-4.25}$, the activation energy (Si <100>), E_a = 0.595 electronvolts (eV), k is the Boltzmann constant, and T is the temperature of the KOH solution.[95]

This means that one can achieve very fine control of etching in the <100> crystalline

orientation, however, for a 500 μm silicon wafer immersed in a 10 % solution of KOH (the etching rate was generally found to decrease as concentration increased) at 20 °C, the etching process would take roughly two weeks.[95] Needless to say, a fine balance between crystalline orientation selectivity and the efficiency of the processing time is necessary to achieve practical etching results in KOH solutions. In addition, Seidel *et al.* estimated the upper limit for silicon nitride etching in KOH solutions to be less than 0.1 nm / hour (h), making silicon nitride etching practically negligible during the KOH etching process.[95] However, depending on a number of factors including the concentration and the temperature of the KOH solution used, additional studies have found that this etching may be on the order of a few nanometres per hour, suggesting that careful planning and controls are necessary to maintain the desired thickness of the silicon nitride membrane.[63,96] Lastly, a buffered oxide etch should be considered prior to KOH etching to remove any surface oxide which may have formed on the surface of the silicon in between process steps. This buffered oxide etching process may be completed by dipping the wafer into HF as described in the beginning of this section. If surface oxide remains on the silicon prior to etching the wafer in KOH solution, the etching rate will be reduced until the surface oxide layer has been removed. The etching of silica was also investigated by Seidel *et al.* and they determined that the maximum etching rate of silica was obtained at a KOH concentration of 35 %. For a KOH solution at 80 °C, the etching rate was determined to be 440 nm

/ h, while at 20 °C, the etching rate was determined to be 1.44 nm / h.[95] Considering that the silica layer formed will typically be of a thickness between 0-5 nm, the silica layer will not significantly inhibit the etching of the silicon substrate in high temperature KOH solutions.[97] The buffered oxide etch process may be viable for low temperature and/or low concentration KOH solutions where the etching rate is significantly reduced.[95] Figure: 2.7 summarizes the basic fabrication steps necessary in order to produce NFCs capable of being used in LC-TEM measurements.[63] Of course, to produce commercially practical NFCs, additional features should be present within the NFC such as spacer material, an etched step for an o-ring groove, liquid flow entry / exit ports for flow cells, and dicing / snap lines for ease in LC device separation from the wafer. Many of these features can of course be implemented through the use of the methods already described but with careful consideration of the engineering requirements for the development of these features. Most importantly, the spacer material should be developed to ensure a liquid thickness on the order of tens to hundreds of nanometres in order to avoid the loss of imaging resolution due to scattering of the electron beam.[98]

Although the description of the nanofabrication process of NFCs presented here is brief and is by no means a complete and rigorous detailing of the possibilities of nanofabrication in engineering miniature reaction vessels for LC-TEM, the basic nanofabrication steps for a rudimentary understanding of the science have been outlined so that the processes

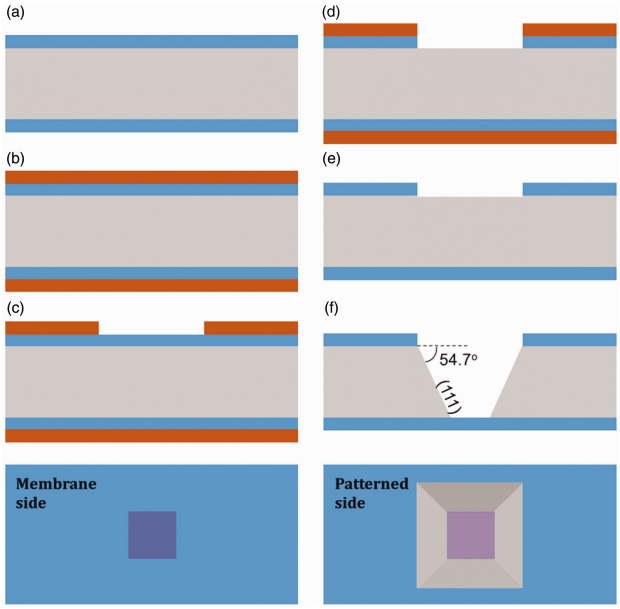


Figure 2.7: A summary of the nanofabrication steps described as illustrated through the development of the wafer structure. a) The deposition of silicon nitride onto a Radio Corporation of America (RCA) cleaned <100> oriented silicon substrate. b) Spin-coating of the silicon nitride coated wafer. c) Photolithography of the spin-coated wafer. d) Reactive ion etching (RIE) of the exposed silicon nitride film. e) Stripping of the photoresist. f) Potassium hydroxide (KOH) etching of the silicon wafer to release the silicon nitride window membrane. Reprinted with permission from J.R. Dwyer and M. Harb, Through a Window, Brightly: A Review of Selected Nanofabricated Thin-Film Platforms for Spectroscopy, Imaging, and Detection, *Appl. Spectrosc.*, **71**, 9, 2051-2075, (2017). Copyright © 2017, J.R. Dwyer and M. Harb.[63]

may be appreciated. Utilizing optimized recipes for NFC production, proprietary NFCs were developed in conjunction with a proprietary loading method to resolve long-standing challenges which have existed within the LC-TEM community as will be shown in chapter 3.

2.3 The evolution of the design of a static NFC assembly kit for LC-TEM

When designing a set of tools for electron microscopy one is met with a series of limitations defined by the electron microscope. The electron microscope holder itself must be designed with attention to the internal dimensions of the electron microscope. Imprecision of the machining of these tools must be minimized as much as possible to avoid damaging the electron microscope while ensuring the sample position is appropriately defined within the stage area. In addition to this, the selection of appropriate materials to be utilized in a high or ultra-high vacuum environment must be considered so that the user is not contaminating the column with the insertion of the holder. In LC-TEM, the design challenges of making a suitable holder for electron microscopy are met with the additional non-trivialities of nanofabricating NFCs for use in a novel holder. In this section I will provide details on the rationale behind the evolution of the design process for the holders and NFCs designed and utilized in this thesis. In the sections which follow, I will discuss the design rationale of the current NFCs and the most recent version of the loading station.

The static NFC assembly kit outlined in this thesis was designed over multiple iterations with multiple batches of NFCs. Original designs provided a proof of concept to test the encapsulation of liquid within an NFC through the use of either a miniature o-ring or epoxy.

Circular NFCs were utilized initially with the ideology that NFCs could be employed in any standard electron microscopy holder. This circular design is highlighted in Figure: 2.8.

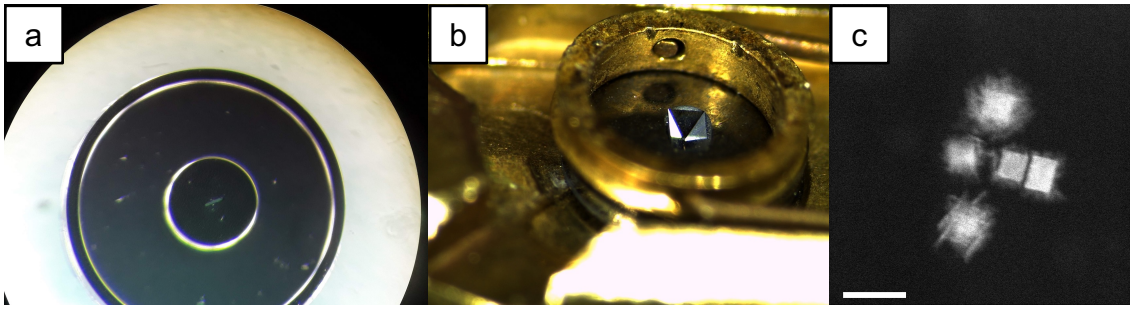


Figure 2.8: A universal circular nanofluidic cell (NFC) for electron microscopy. a) An optical microscopy image of a circular NFC. This circular NFC design was created to be used universally in any electron microscopy holder that can fit a 3 millimeter (mm) copper grid. This cell was developed at the Quantum-Nano Fabrication and Characterization Facility (QNFCF) at the University of Waterloo by the Ultrafast electron Imaging Laboratory (UeIL). b) The circular NFC in a standard single-tilt electron microscopy holder. c) A scanning transmission electron microscopy (STEM) image of 40 nanometre (nm) wide palladium core, ruthenium shell (Pd@Ru) nanoparticles captured inside of a fractured circular NFC, rendering the NFC to be essentially dry. Scalebar: 50 nm

In addition to the NFC devices fabricated here, an early version of the static NFC loading station which was compatible with a custom circular NFC was machined by myself in the student machine shop located in the Physics Department at the University of Waterloo. Although, this circular NFC design was ideal for providing electron microscope users with the flexibility in using almost any standard microscope holder, the assembly of circular NFCs within the electron microscopy holder was limited by this geometry. This lead to complications in the assembly process such as misalignment of windows during the NFC assembly. Assembly of these devices proved to be more challenging than originally anticipated leading to limited success in entrapping liquid within the NFC (Figure: 2.8c).

From this design, it became clear that a rectangular NFC would be ideal for fast and reliable LC-TEM sample loading. For each, new NFC design, a unique electron microscopy holder tip had to be designed and machined to house the NFC. Some of the various NFC designs and electron microscopy holder tips described above and developed by the UeIL can be seen in Figure: 2.9.

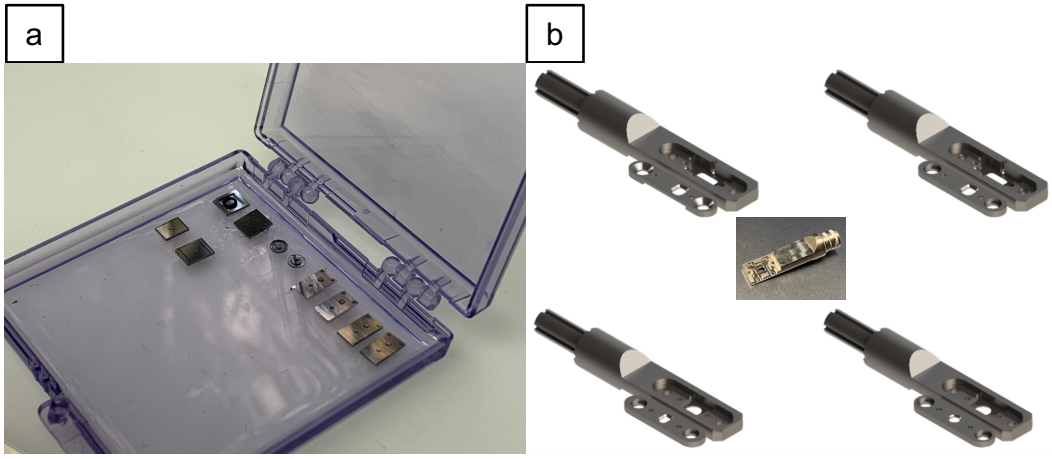


Figure 2.9: Various unique nanofluidic cell (NFC) designs and electron microscopy holder tips developed by the Ultrafast electron Imaging Laboratory (UeIL). a) NFCs developed by the UeIL at the Quantum-Nano Fabrication and Characterization Facility (QNFCF) at the University of Waterloo by the UeIL. b) The corresponding electron microscopy holder tips developed by the UeIL. The circular NFC design utilized a standard electron microscopy holder tip for sample imaging and therefore a unique holder tip was not developed for this design.

Additional batches of NFCs were generated as different processes of photolithography, etching, and dicing were tested and developed to continuously improve upon the previous batch of NFCs. With each additional NFC design, new loading stations were developed to improve the sample loading method. The original loading station design for example relied on a user taking the sealed NFC from the loading station and then placing it into

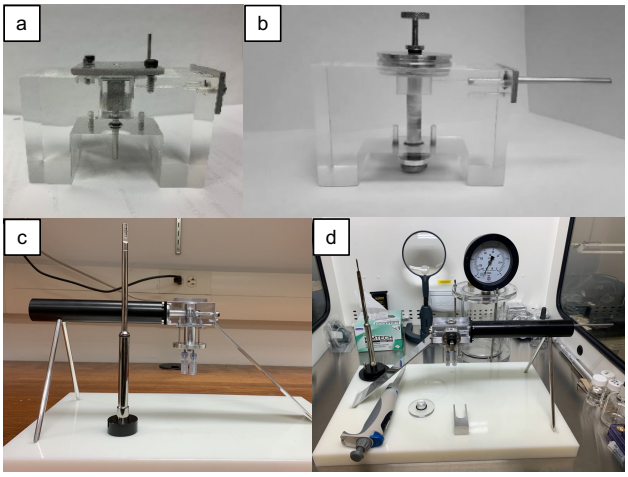


Figure 2.10: The various liquid-cell (LC) loading stations developed for preparing samples for static (LC-TEM) experiments. a) An original prototype for loading square NFCs with an o-ring acting as a hermetic seal. Here NFCs were prepared in the vacuum of the loading station and then transferred to a unique electron microscopy holder. b) The universal circular NFC loading station. Here NFCs were prepared in the vacuum of the loading station and then transferred to a standard electron microscopy holder. c) The first version of a loading station for rectangular LCs where the assembly and sealing of the NFC was done entirely within the loading station. d) An updated version of a loading station for rectangular LCs where the assembly and sealing of the NFC was done entirely within the loading station. This version of the loading station includes a miniature valve for fast vacuum chamber evacuation and improved alignment of the holder during NFC assembly.

the electron microscopy holder (Figure: 2.8b). The main flaw of this design is that the tiny and fragile NFC must be handled by the user after assembly which can cause one to damage the assembled NFC or break the hermetic seal inside of the NFC. Therefore, it became highly important for the NFCs to be assembled within the electron microscopy holder itself. The various loading station designs developed by the UeIL can be seen in Figure: 2.10.

2.4 A novel NFC for static LC-TEM experiments

As discussed previously, the technique of LC-TEM has faced obstacles in imaging due to bulging of the window membrane material. However, another challenge within the community is reliably producing liquid layers which reflect the height of the so called "spacer" material. This is a layer of material (eg. SU-8, gold, silicon dioxide (SiO_2)) which is typically deposited onto the surface of NFCs to define the depth of the cavity which the liquid sample can occupy.[53,99,100] A conventional NFC is shown in Figure: 2.11.

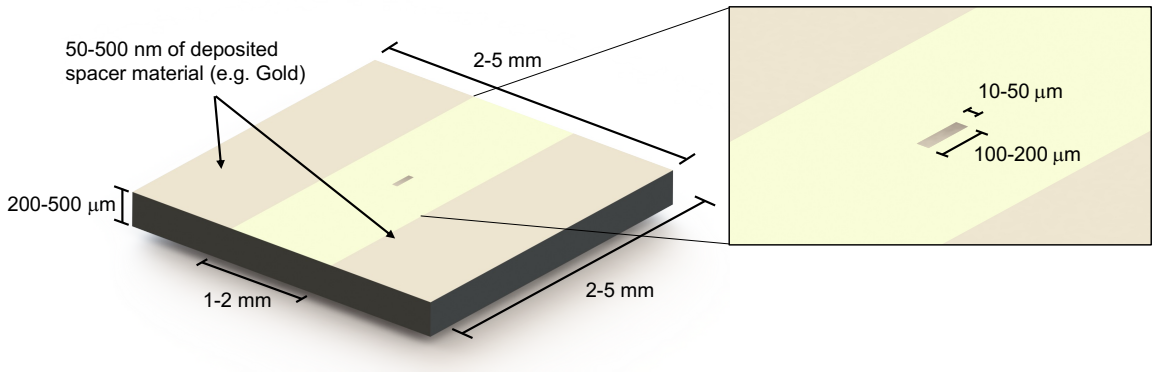


Figure 2.11: The dimensions of a conventional liquid-cell (LC) for liquid-cell transmission electron microscopy (LC-TEM).

Typical static LC-TEM experiments are conducted within flow cells due to a relative absence of static NFC availability in the commercial market. These conventional NFCs typically have dimensions on the order of $\sim$ (2-5) x (2-5) mm^2, with $\sim$ 1-2 mm of channel width within the NFC for liquid flow. A wide variety of spacer thicknesses are typically available, $\sim$ 50-500 nm in thickness. The dimensions of the window membrane material

also typically have an aspect ratio of greater than or equal to four to reduce the bulging of the window membrane material as will be seen in section 2.5. However, the design of these NFCs as seen in Figure: 2.11 consists of a flat NFC geometry where liquid within the flow channel can easily overflow onto the spacer material thus compromising the desired liquid layer thickness as set by the deposited spacer thickness. The typical preparation process for such a NFC might involve dropcasting / depositing a 500 nanolitre (nL) droplet of liquid sample onto a conventional LC and then loading the LC into an electron microscopy holder for imaging after forming a hermetic seal around the NFC assembly. Enclosing liquid within this design in this way has a number of drawbacks. In the ideal scenario, the liquid which is dropcast onto the LC should be confined within the nanofluidic channel and not overlap with the spacer material. However, in reality, since this NFC design utilizes relatively flat NFC geometries, the dropcast liquid spreads from the nanofluidic channel onto the spacer material when the NFC assembly is formed. In combination with the overflowing liquid, the sample itself will contribute to the overall thickness of this newly defined spacer caused by the compromising of the spacer. This behaviour of spacer overflow can be visualized in Figure: 2.12.

For this conventional NFC design, the spacer is compromised in almost every case which does not utilize an ultrasmall volume dropcasting method.[101] In fact, for a typical conventional NFC that has a 200 nm total spacer, with a nanofluidic channel of 1 mm in

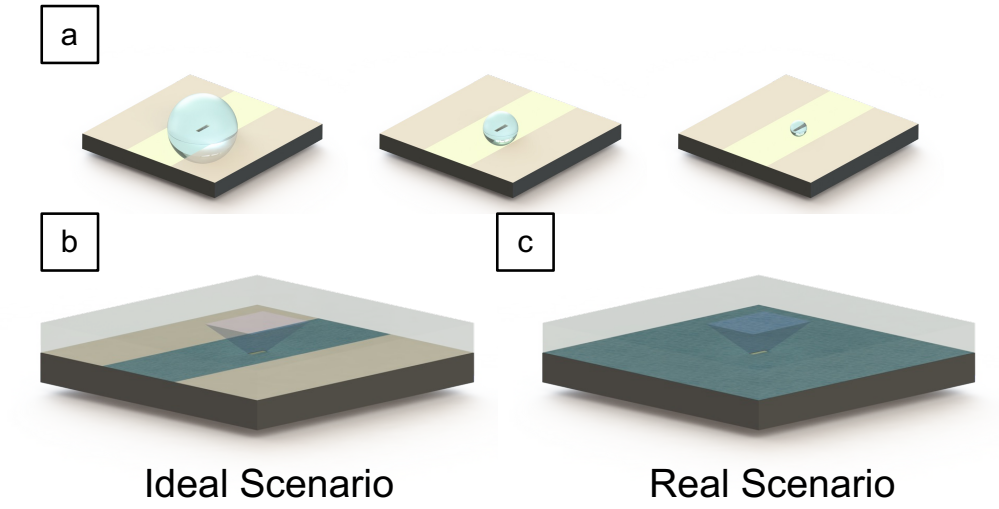


Figure 2.12: Spacer overflow in conventional nanofluidic cells (NFCs). a) A series of computer-aided design (CAD) renders of a conventional liquid-cell (LC) depicted to scale with a 500 nanolitre (nL) sample droplet evaporating to 2.5 nL b) A CAD render of an assembled NFC depicting the ideal scenario of sample loading for liquid-cell transmission electron microscopy (LC-TEM) for this design. In this scenario, liquid is confined within the nanofluidic channel, and the spacer is not compromised. c) A CAD render of an assembled NFC depicting the real scenario of sample loading for LC-TEM for this design where the spacer is overflowing with liquid. In this scenario, liquid spreads from the nanofluidic channel onto the spacer when the NFC assembly is formed and the spacer is therefore compromised.

width, 600 picolitres (pL) is enough liquid volume to cause an overflowing of liquid from the nanofluidic channel to the spacer material. In addition, to the issues with liquid overflow in conventional NFC designs, there is also an additional concern of micro-contamination onto the surface of the spacer material during the handling of the LCs. Regular handling of LCs with typical carbon fibre coated tweezers causes small particulates to break off from the edges of the LCs. In combination with the general preparation of NFCs in non-cleanroom conditions, these micron sized particulates can cause the spacer of the NFC to be compromised before liquid is even introduced to the LC. This micro-contamination

may be visualized in Figure: 2.13. An alternative, design and methodology is necessary to avoid these issues to increase the chances for success in LC-TEM experiments. Therefore, these NFCs should not be utilized for static LC-TEM experiments if spacer reproducibility is desired in the NFC assemblies.

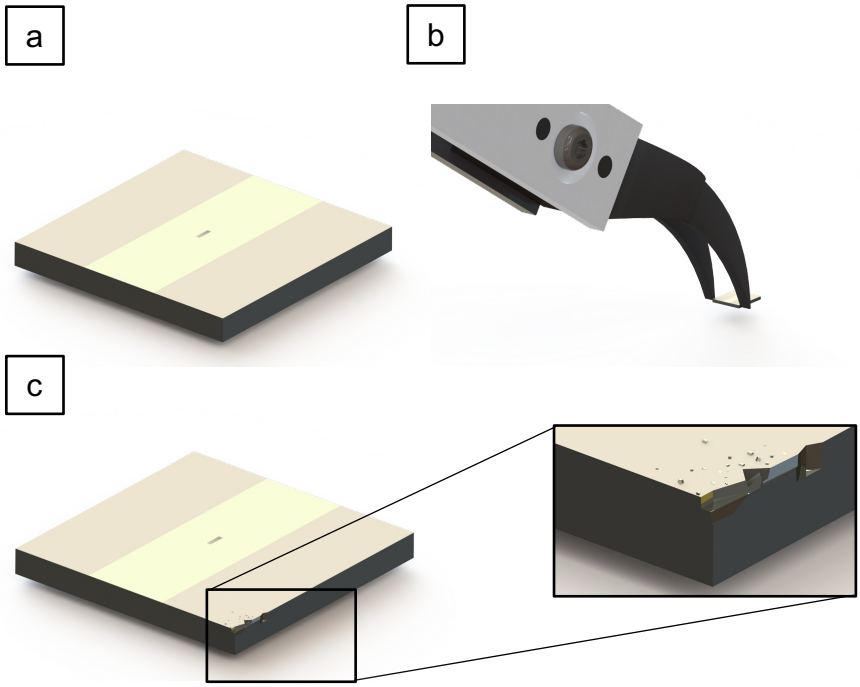


Figure 2.13: Spacer contamination of conventional liquid-cells (LCs) from regular handling. a) A computer-aided design (CAD) render of a pristine LC from the manufacturer. b) A CAD render depicting the handling of a pristine LC with a commonly utilized carbon coated tweezer. c) A CAD render showing an artistically exaggerated visualization of particulate contamination introduced by regular handling of the LC with a carbon coated tweezer.

Due to the issues presented in the typical NFCs which were traditionally utilized to perform static LC-TEM experiments, a new NFC was developed at the Quantum-Nano Fabrication and Characterization Facility (QNFCF) at the University of Waterloo by the

UeIL. These new NFCs were designed to solve the inadequacies of the existing commercial NFCs which had previously been utilized to perform static LC-TEM experiments. To advance upon the design of the essentially flat geometry of commercial NFCs, the newly developed NFCs were shape engineered to ensure that the liquid sample could no longer invade the spacer material. Additionally, this design also combats the inadequacies of the conventional NFCs used for static LC-TEM by minimizing the spacer contact area and therefore limiting the probability of spacer micro-contamination from air-borne particles by more than 300 times. This design also minimizes the chance of contaminating the spacer area by providing users with locations on the LCs for handling, locations that if damaged by regular tweezer usage will not compromise the spacer. This design is illustrated in Figure: 2.14.

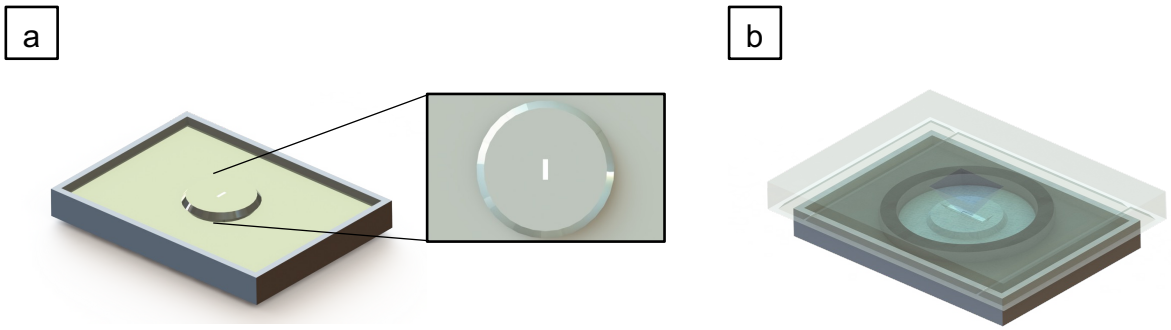


Figure 2.14: New nanofluidic cells (NFCs) developed by the Ultrafast electron Imaging Laboratory (UeIL). a) A computer-aided design (CAD) render of a liquid-cell (LC) engineered for the deposition of liquid samples. Inset: A render of a zoomed perspective of the liquid-cell, focusing on the central pillar where the liquid sample is deposited and positioned. b) A CAD render of an assembled NFC which displays the same LC shown in a) with an o-ring enclosing a liquid sample while being sandwiched against a second chip (transparent). Typical sample droplet volumes are on the order of a few hundred nanolitres (nL).

The NFCs developed by the UeIL are markedly larger in dimensional area (~ 50 %) than the NFCs which are commercially available for conventional static LC-TEM experiments. This enhancement in the size of the NFC offers an ease of handling for the user while introducing beneficial features of a three-dimensional design. As seen in Figure: 2.14b, the newly designed NFCs offer a region of dead volume for liquid sample deposition which is enclosed by the o-ring. This feature ensures that the liquid sample does not escape from the defined area which is not the case for conventional NFCs. Therefore, blotting of the sample with tissue paper or extended waiting times for sample evaporation is not necessary if the correct sample volume is deposited as dictated for the employed o-ring and etch depth in the LCs. In addition, the spacer material itself is located far from the deposited sample location. Therefore, liquid cannot spread from the central pillar to the perimeter of the LC where the spacer is located and precisely defined. The use of a proprietary loading station is a necessity of this NFC design. Attempting to assemble an NFC for LC-TEM measurements without the removal of air from the loading station vacuum chamber will result in air being trapped between the two LCs. This entrapment of air will subsequently result in the rupture of the window membranes due to the pressure differential between the internal cavity for the liquid sample and the vacuum of the electron microscope.

2.5 Development of a novel method for LC-TEM sample loading

In order to address the challenges which still remain in LC-TEM despite improvements to NFC design, a novel static NFC assembly kit (Figure: 2.15) was developed to prepare proprietary NFC assemblies for liquid phase imaging in the electron microscope. The NFC assembly kit includes a novel NFC design as previously described in section 2.4, a unique NFC electron microscope sample holder, and a loading station for the fast loading of static NFC samples. In combination with the NFCs, the loading station ensures that LC-TEM samples are prepared in the absence of air, therefore ensuring that the pressure differential between the inside of the cell and the column of the electron microscope is reduced. This reduction in the pressure differential essentially eliminates bulging within the window membrane when the adhesive and cohesive forces of the thin liquid layer are considered in the absence of air.

Prior to assembling the NFC inside of the loading station, one chip which forms the NFC assembly is placed into the NFC electron microscope sample holder while another chip is placed inside of a lid loading tool (piston). The sample holder is then inserted into the loading station chamber and a liquid sample is drop-cast onto the chip within the lid loading tool. To prepare the NFC assembly in the absence of air, the loading station

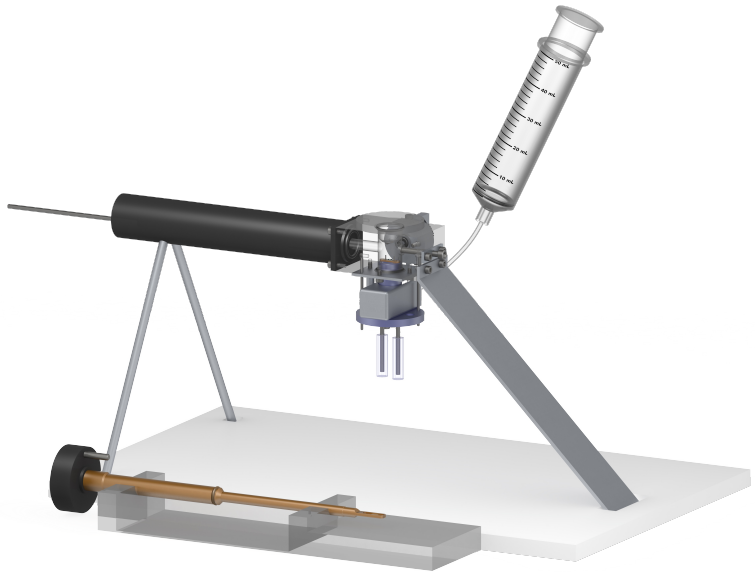


Figure 2.15: The liquid-cell transmission electron microscopy (LC-TEM) electron microscope sample holder and loading station. A novel NFC assembly kit for the loading of samples for LC-TEM. Samples are prepared in the absence of air. The holder and holder lid are coloured orange, while the sample loading piston is coloured blue here for clarity.

is evacuated with a simple Luer-Lok™ syringe or a small rotary vane pump to remove atmospheric air. The NFC is then assembled in the evacuated environment of the chamber and sealed hermetically within the NFC sample holder. The assembly process takes 10 minutes or less to complete, to go from sample delivery to the electron microscope for imaging. The process is briefly outlined in Figure: 2.16.

In Figure: 2.16 the design and assembly method of the assembly kit are illustrated to highlight the importance of the alignment of the electron microscopy holder lid with the body of the holder, as well as the evacuation of the loading station vacuum chamber

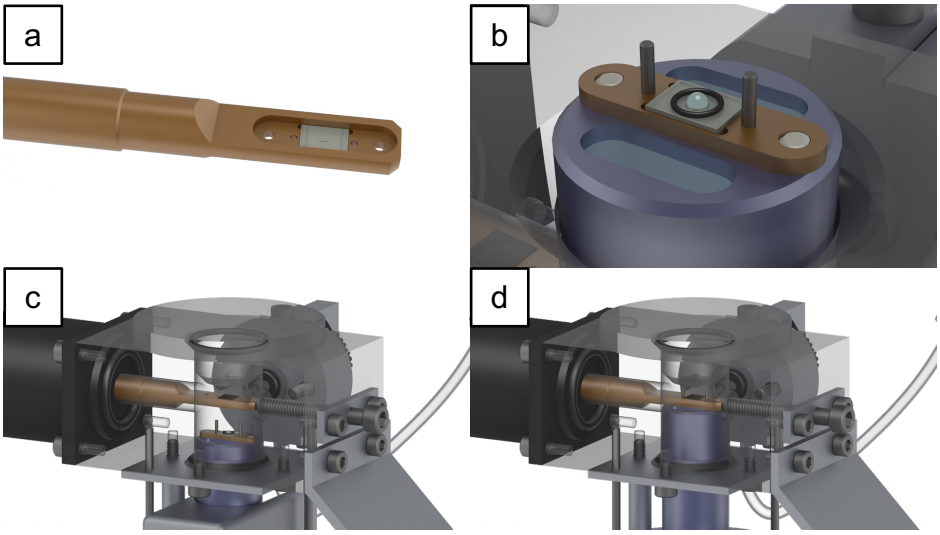


Figure 2.16: The preparation of the nanofluidic cell (NFC) assembly using the novel assembly kit. a. The sample holder is fitted with an NFC chip. b. The second NFC chip is placed into the lid of the sample holder before a sample is drop-cast onto the NFC. c. The loading station is evacuated of air using a Luer-Lok™ syringe or a rotary vane pump before bringing the two NFC chips into contact to form the NFC assembly. d. The two NFC chips are brought together to form the assembly before the loading station is vented and the NFC holder is removed for imaging in the electron microscope.

(Figure: 2.16c) before the NFC assembly can be formed (Figure: 2.16d). This method reduces the pressure in which the NFC assembly is established therefore reducing the pressure differential in which imaging is conducted at (eg. ∼760 Torr to ∼20 Torr at room temperature conditions).[102] In addition, multiple evacuation cycles can be conducted in the case of using a syringe to remove air from the loading station vacuum chamber. This may be appreciated through Equation: 2.13 below.

$$p_{air,f}\left(n\right) = p_{air,i}\left(\frac{V_S}{V_S + V_R}\right)^n \tag{2.13}$$

where $p_{air,f}$ is the final pressure inside of the loading station vacuum chamber after the air evacuation process is repeated n times, $p_{air,i}$ is the initial pressure in the loading station vacuum chamber, V_S is the dead volume inside the loading station, and V_R is the internal volume of the syringe.

From Equation: 2.13 it also follows that the chemical potential of the water utilized in the sample droplet is of key interest. By saturating the loading stage vacuum chamber and the syringe with water vapour we can further discourage the evaporation of the liquid sample droplet before the NFC has been sealed for imaging. Saturation of the loading stage through the implemented utilization of surrounding bodies of water ensures that mass transfer from the liquid sample droplet does not occur to a significant degree. In this way, the loading station vacuum chamber is saturated with water vapour and the pressure within the loading station after the evacuation of air is equal to ∼20 Torr at room temperature conditions.[102] Without saturation in this manner, considering the ideal gas law, dropcast samples of less than a microlitre of volume are at risk of evaporation during the evacuation process. Figure: 2.5 summarizes the evacuation process outlined above in Equation: 2.13.

To illustrate the consequences of the equations and theory introduced above, we consider a loading station vacuum chamber, V_S, with a volume of 3 mL, and a syringe with a volume

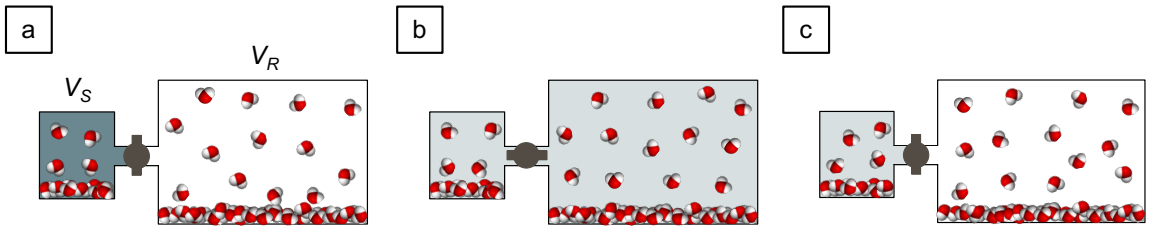


Figure 2.17: A cartoon illustration of the evacuation of the loading station in the preparation of a nanofluidic cell (NFC) assembly. a. The loading station, with a volume of V_S, is originally full of air within the standard laboratory environment. A vacuum syringe, with a volume of V_R, is connected to the loading station with its plunger extended. At this time, the valve which separates the loading station and the vacuum syringe is closed. b. The valve which separates the loading station and the vacuum syringe is opened allowing air from the loading station to move into the syringe to form an equilibrium. c. The valve which separates the loading station and the vacuum syringe is closed and the air within the syringe is vented, before extending the plunger of the syringe again in preparation for another cycle of air evacuation. Note that the loading station and syringe are saturated with water in this process, where wells of water surround the NFC in the loading station and the tubing which connects the syringe to the vacuum valve is filled with water to ensure that air is not trapped in the syringe during the evacuation process. Reproduced with permission from T. S. Lott *et al.*, Robust Fully Controlled Nanometer Liquid Layers for High Resolution Liquid-Cell Electron Microscopy, *Lab Chip*, **23**, 3217-3225, (2023).[57]

of 60 mL, V_R. If one were to evacuate the loading station vacuum chamber three times, defining $n = 3$ from Equation: 2.13, $p_{air,f}$ would be equal to ∼0.08 Torr which is well below the minimum attainable internal NFC pressure of ∼20 Torr which is given by the vapour pressure of pure water at room temperature conditions.[102]

Now that the NFC has been assembled in a relative absence of air, the anticipated bulging of the silicon nitride films has been reduced substantially. What was once expected to bulge on the order of hundreds to thousands of nanometres has now been reduced to tens of nanometres or less when considering the adhesive and cohesive forces of the ultrathin liquid water layers. Figure: 2.18 illustrates the geometry of a typical NFC assembly and introduces Equation: 2.14 to discuss some of the critical variables which must be examined.

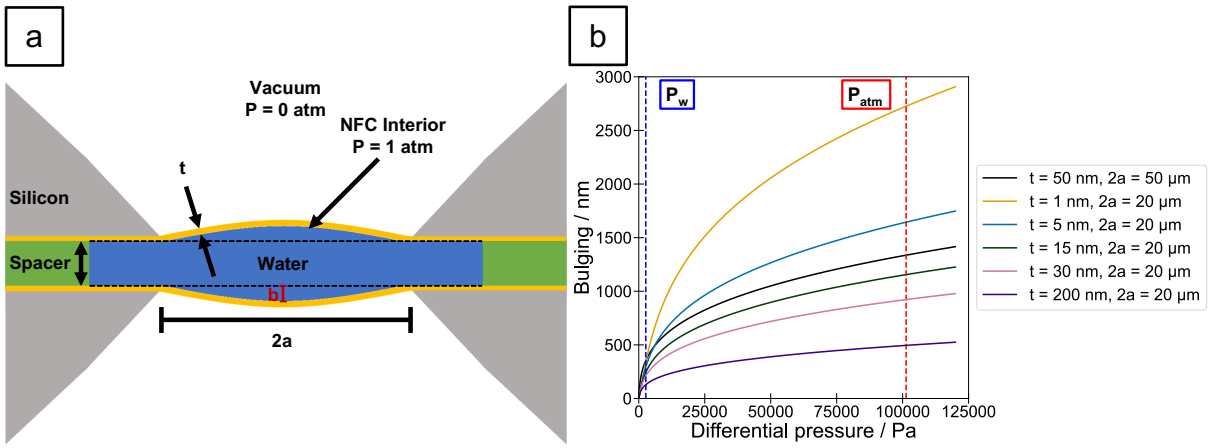


Figure 2.18: Bulging of nanofluidic cell assemblies (NFC) under an applied pressure differential. a) A cartoon side cross-section view of a typical NFC. Within this assembled NFC the window membrane is seen to bulge due to the pressure differential ($\sim$ 1 standard atmosphere (atm)) between the interior of the NFC and the high-vacuum column of the electron microscope. The black dashed lines in the region of the water indicate the expected liquid layer thickness in the absence of bulging as defined by the spacer material. b) A plot showing the relationship that NFC assembly bulging has with pressure differential between the interior of the NFC and the column of the electron microscope. P_w is the vapour pressure of water ($\sim$ 20 Torr at room temperature conditions)[102] and P_{atm} is the atmospheric pressure. Calculations were performed utilizing Equation: 2.14. In this figure, the variables a, b, t are defined as the the half-length of the short side of the window membrane, the bulging of both of the window membranes, and the thickness of the window membrane respectively. Calculations were performed for low stress silicon nitride films with the following parameters: $\sigma_0 = 147$ MPa, $E = 222$ GPa, and $\nu = 0.28$.[64]

Figure: 2.18 also emphasizes the importance of minimizing the pressure differential when introducing LC-TEM samples into the electron microscope. In the high-vacuum of the electron microscope column, the NFC contains a mixture of liquid water and air which was trapped during the NFC assembly process. The trapped air which can be assumed to be trapped within the NFC at a pressure of 1 standard atmosphere (atm) causes significant bulging of the window membrane substantially reducing the imaging resolution of the subsequent LC-TEM experiment. Thin window membranes can be utilized in LC-TEM

but as the thickness of the membrane decreases, the bulging of the membrane increases substantially. However, as membrane thickness increases, the transmission of the electron beam is diminished as seen in subsection 2.1.1. When conducting an LC-TEM experiment one must carefully employ thin window membranes to ensure that bulging is minimized. Looking at Figure: 2.18b, it becomes clear that thin window membranes and hybrid NFCs would benefit greatly from following the sample loading method of the discussed assembly kit.

Equation: 2.14 shown below introduces the critical variables which must be considered for minimizing window membrane bulging in NFCs as illustrated in Figure: 2.18.[64]

$$\Delta P = \frac{ct\sigma_0}{a^2}b + \frac{8Et}{6a^2\left(1-\nu^2\right)}b^3 \tag{2.14}$$

where ΔP is the pressure differential which is acting on the membrane, c is a constant defined as 3.4 for square membranes or 2 for membrane aspect ratios greater than 4, t is defined as the thickness of the membrane, σ_0 is defined as the residual stress of the silicon nitride membrane, a is defined as half of the length of the short side of the window membrane, b is the bulging of the membrane, E and ν are defined as the Young's modulus and Poisson ratio respectively for a silicon nitride membrane.[64]

Equation: 2.14 highlights an important detail of NFC engineering in that the short side of the window membrane (a) should be minimized in order to minimize the amount of bulging that the membrane will experience in the presence of an applied pressure differential acting on the membrane.[64,103] Therefore, when designing a new NFC for LC-TEM experiments, it is critical that the width of the LC window membrane be minimized sufficiently to achieve an aspect ratio greater than four which is the case for all membranes presented in this thesis. It is also important to realize that the width of the window membrane will define the viewing area during an LC-TEM experiment; this is because LCs are generally assembled to form an NFC in a geometry such that the windows of each LC are perpendicular to one another. This ensures that the windows are aligned sufficiently when attempting to view through the windows of the NFC assembly in the electron microscope. This is a necessary requirement of the assembly process as machining tolerances of NFC microscope holders are typically larger than the width of typical LC windows which are designed to keep membrane bulging at a minimum.

Ideally, one should completely fill an NFC cavity with liquid water after first evacuating the entirety of the NFC of air. While this may be accomplished to a degree in a flow cell setup, this is complicated in a static NFC design where the liquid is enclosed within an o-ring. Therefore, for practical, fast assembly of NFCs, the static NFC assembly kit is a reliable solution. Lastly, even though thinner window membranes are more susceptible to

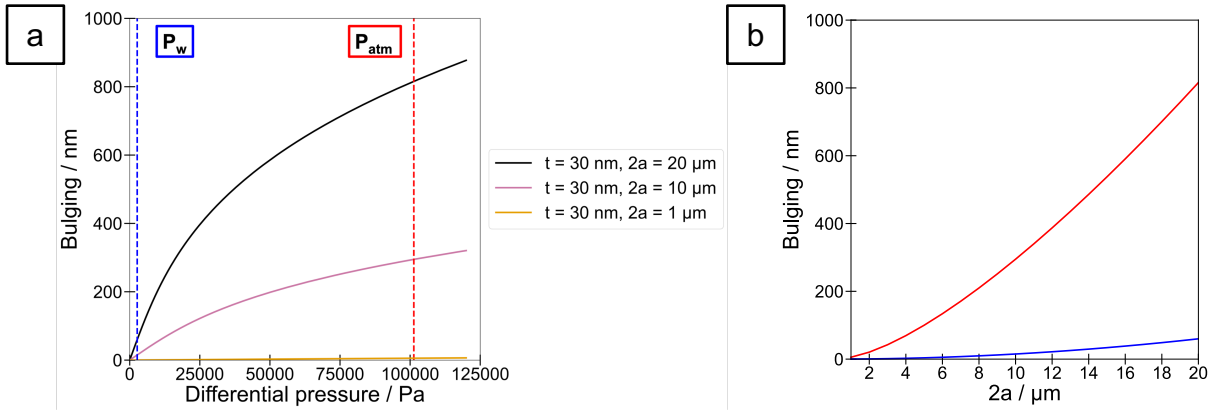


Figure 2.19: Reducing the bulging of nanofluidic cell assemblies (NFC) by reducing the short length of the silicon nitride (SiN_x) window membrane. a) A plot illustrating that NFC assembly bulging can be reduced by reducing the short length of the window membrane in the NFC design. b) A plot of NFC bulging at fixed pressures of P_w (blue) and P_{atm} (red) where bulging is a function of the short length of the window membrane which has a thickness of 30 nanometres (nm). P_w is the vapour pressure of water ($\sim$ 20 Torr at room temperature conditions)[102] and P_{atm} is the atmospheric pressure. Calculations were performed utilizing Equation: 2.14. In this figure, the variables a and t are defined as the the half-length of the short side of the window membrane and the thickness of the window membrane respectively. Calculations were performed for low stress silicon nitride films with the following parameters: $\sigma_0 = 147$ MPa, $E = 222$ GPa, and $\nu = 0.28$.[64]

bulging, this behaviour can be reduced by decreasing the length of the short side (a) of the window membrane. Figure: 2.19 highlights how the short side (a) of the silicon nitride window membrane can be varied to minimize bulging in a NFC.

The loading station for this LC-TEM sample loading method was designed with a number of key features to ensure that sample assembly is fast, efficient, and reproducible. A unique electron microscopy NFC holder was designed in tandem with the loading station for each generation of NFCs. The loading station ensures that samples are prepared in the absence of air with precise alignment of the LCs. Due to machining tolerances (typically,

at best two thousandths of an inch or $\sim$ 50 µm), a number of features were added to the loading station to ensure that samples are prepared consistently. This begins with the proper design and machining of the electron microscopy holder that will be used to contain the NFCs. These holders as well as the loading stations are designed at the UeIL with precision machining completed by Science Technical Services (STS) at the University of Waterloo. The design of the holder takes the key internal features of the electron microscope into account and allows for safe internal clearance of the holder. The holder tip is carefully designed and machined to seat the nanofabricated LCs, while ensuring that the sample will be located on the optical axis of the electron microscope. Imprecision in this step of the design can result in the sample being located outside of the range of the sample stage of the electron microscope leading to an inability to acquire data. The handle of the holder is designed with a through-hole to allow for a pin located at the end of the loading station to align the holder with the loading station. The alignment of the LCs for the assembly process is then further aided by two smaller pins located on a piston (lid loading tool) which sits within the loading station vacuum chamber. This piston acts to hold the lid of the electron microscopy holder tip and one of the LCs. A detailed assembly process is highlighted in Figure: 2.20. The assembly process is completed through a series of simple steps designed to ensure that the LCs are properly aligned within the electron microscopy holder, as well as to ensure that the liquid sample does not evaporate during the formation

of vacuum within the loading station vacuum chamber. Materials were chosen on the basis of durability, compatibility (chemical and physical), and ease / practicality of machining. For example, titanium alloys are high strength materials which typically display a good compatibility with the high-vacuum of the electron microscope. Although this material is typically more difficult to precision machine than a material such as aluminum, the strength of titanium alloys makes them very desirable for producing both small and large components which will be exposed to repetitive usage. Polyether ether ketone (PEEK) screws have low out-gassing suitable for the high-vacuum of the electron microscope while being compatible with the titanium thread located in the holder tip. Materials employed within the loading station design are selected for their ease in machining such as aluminum 6061, polyoxymethylene, and polycarbonate. All of these materials are durable and readily employed for repetitive usage making them ideal for the task of assembling NFCs.

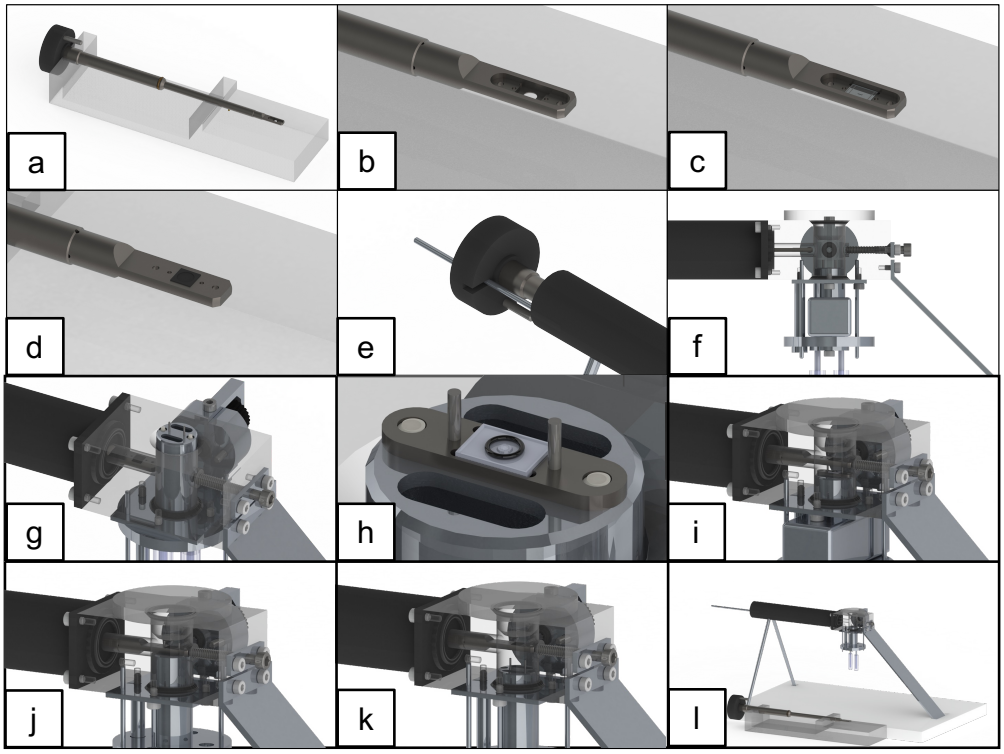


Figure 2.20: A detailed assembly process of the loading station designed to assemble liquid-cells (LCs) for liquid-cell transmission electron microscopy (LC-TEM). a) The electron microscopy holder is put in place in preparation for the assembly process. b-c) Starting from an empty holder tip, the first LC is placed into the holder. c) Carbon tape for electron microscopy is utilized to keep the LC in place within the holder tip. d) The electron microscopy holder with the LC is placed into the loading station with the aid of a guiding pin which is attached to the loading station. f) The holder is partially inserted to ensure that the lid loading piston can be pushed above the vacuum chamber for the loading of the second LC. Two wells which reside inside of the piston are filled with water to ensure the the vacuum chamber is saturated with water vapour after evacuation. h) A second chip is placed into position with the appropriate miniature o-rings for hermetic sealing, the holder tip lid, and Polyether ether ketone (PEEK) screws which are used to seal the assembled nanofluidic cell (NFC) within the electron microscopy holder. The sample is then dropcast onto the surface of the chip. i) The piston of the loading station is lowered and a stopper is placed on top of it, the holder is fully inserted to ensure alignment of the holder tip with the pins of the piston, and a lid is placed on top of the loading station vacuum chamber. The loading station vacuum chamber is then evacuated of air using a vacuum syringe or a rough vacuum pump. j) The two LCs are brought together to form a hermetically sealed NFC assembly. k) The loading station vacuum chamber is vented and the piston is lowered. l) The holder is removed from the loading station and the NFC assembly is now ready to be imaged.

During the NFC assembly process, the formation of vacuum within the vacuum chamber of the loading station is a key step in ensuring that NFC assemblies do not bulge within the electron microscope. To accomplish this task a specialized miniature valve was designed at the UeIL. Typical valves include a large dead volume of air which would reduce the ability of one to reach the necessary final pressures for assembled NFCs as outlined in Equation: 2.13. Although high-vacuum valves are utilized in a wide variety of instrument designs, finding miniature high-vacuum valves which are directly attachable to instruments such as the loading station can be a challenge. With the use of fluorocarbon or simple nitrile rubber o-rings, a high-vacuum of 10^{-7} Torr can be readily established. Figure: 2.21a illustrates a computer-aided design (CAD) rendered exploded view of the vacuum valve.

The valve is easily constructed with a small number of components which need to be machined, while other components such as screws and o-ring seals are readily available from commercial hardware suppliers. As with the loading station, the material selection for the valve was chosen on the basis of material abundance and machinability. Therefore, aluminum 6061 is an excellent choice for material selection. The dimensions of the valve are roughly $38 \times 30 \times 36$ mm which makes it ideal for sealing against the loading station or for use with any other application which requires dynamic sealing within a confined area. The valve is easily modifiable to scale in size for specific applications. In addition, since the design of this valve is modular, the components are easily replaced as necessary making it

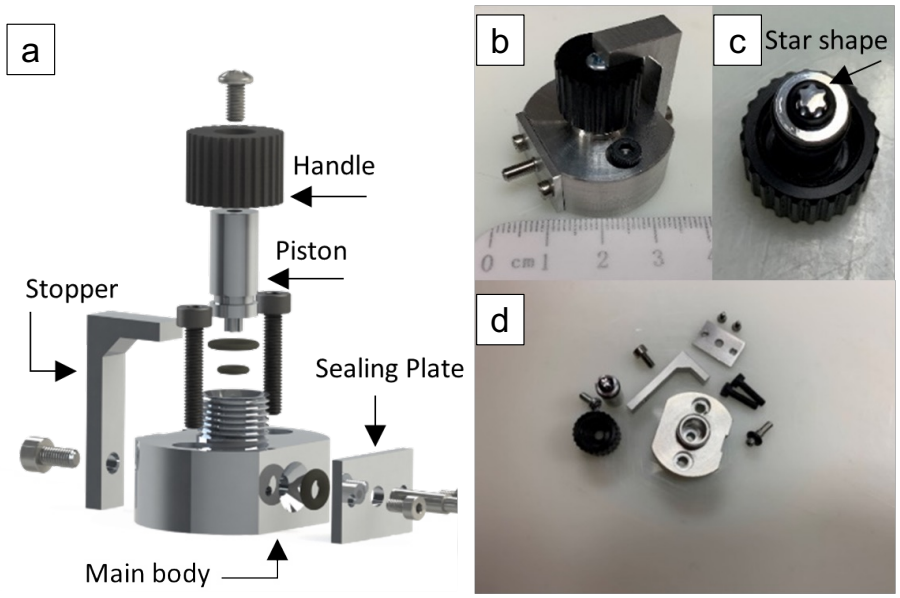


Figure 2.21: A miniature high-vacuum valve developed by the Ultrafast electron Imaging Laboratory (UeIL). a) An exploded three-dimensional computer-aided design (CAD) render of the high-vacuum valve with the main components labelled. b) A machined vacuum valve. All of the metal components shown here were machined from aluminum 6061, the handle was machined from polyoxymethylene, while o-rings and screws were purchased from a commercial retailer. The star shaped design on the bottom of the sealing piston ensures that gas can pass through when the valve is in the open position. d) The machined valve shown in b), disassembled. Reproduced with permission from T. S. Lott *et al.*, A miniature high-vacuum valve, *engrXiv*, (2021).[104]

ideal for prolonged usage with various applications. O-rings in the valve can be replaced when required based on the frequency of usage. Figure: 2.21b-d illustrate the design and structure of a machined valve. The piston component which is shown in Figure: 2.21c provides a glimpse at the star-shaped feature at the bottom. This feature ensures that the o-ring which seals the valve in the closed position is centered and remains centered during the dynamic movement of the piston during regular usage. This star-shaped feature also ensures that the decompression process during the opening of the valve occurs without any

inhibition of gas flow. The sharp edges of within the valve must be removed during the machining process to guarantee that the o-ring is not damaged during usage of the valve. The sealing process itself is attained through the use of two o-rings which are positioned on the piston of the valve. By rotating the handle of the valve, the piston can be raised or lowered so that the bottom o-ring decompresses or compresses, respectively. A cross-section view of the valve can be seen in Figure: 2.22.

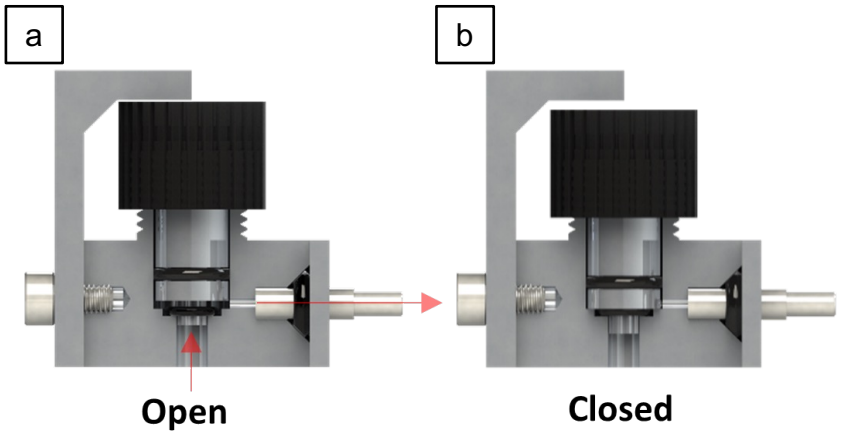


Figure 2.22: The sealing process of the miniature high-vacuum valve. a) The valve is in the open-position, here the valve allows gas-flow to occur without inhibition. b) The valve is in the closed-position, here the o-ring is compressed by roughly 30 % of its cross-section, inhibiting gas flow and subsequently sealing the valve. Reproduced with permission from T. S. Lott *et al.*, A miniature high-vacuum valve, *engrXiv*, (2021).[104]

To ensure that the valve is easy to use, a stopper is attached to the valve to provide the user with a defined open-position for the valve. This open-position allows a vacuum line to evacuate the chamber which this valve is attached to. Gas flow direction is shown with red arrows in Figure: 2.22a. In the case of the loading station, this is the loading

station vacuum chamber where the NFC assembly occurs. The valve can easily seal against any flat surface to form a seal against an external o-ring, and therefore this valve is easily integrated into many high-vacuum applications beyond the use of the loading station.

Improvements continue to be made to the LC-TEM loading station and NFC design. Throughout the course of this Ph.D. project I have had the opportunity to design loading stations and NFC holders for the Hitachi HD-2000, FEI, Hitachi 3300 / 9500, and JEOL microscopes. Currently, we are utilizing the most recent version of the loading station (Figure: 2.23a) to image samples at the Canadian Centre for Electron Microscopy (CCEM). This loading station may be used universally with specialized LC-TEM holders for imaging in FEI, JEOL, and Hitachi electron microscopes (Figure: 2.23b).

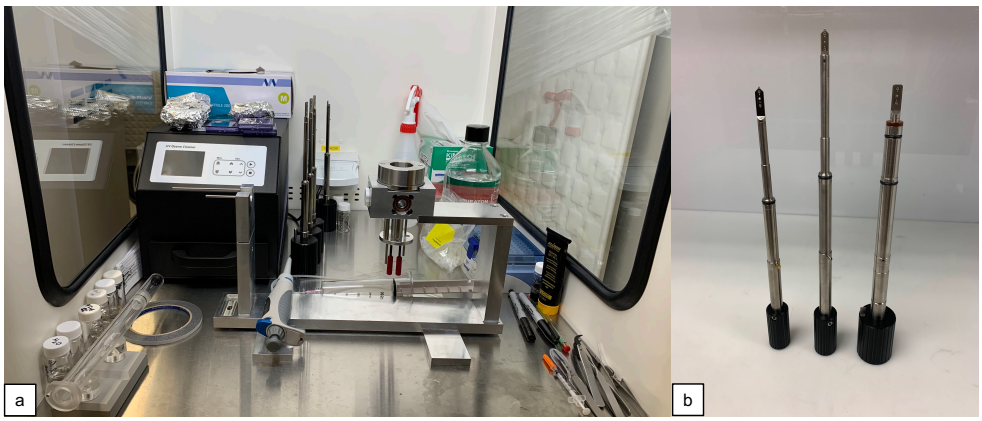


Figure 2.23: Recently developed instrumentation for liquid-cell transmission electron microscopy (LC-TEM) experiments. a) A universal loading station for FEI, JEOL, and Hitachi electron microscopes infront of multiple nanofluidic cell (NFC) holders for FEI microscopes. b) Left to right: An NFC holder for the Hitachi HD-2000 microscope, an NFC holder for the Hitachi 3300 / 9500 microscope, an NFC holder for JEOL microscopes.

Chapter 3

Results and discussion

In this chapter I will discuss the results obtained with the static liquid-cell loading station which was outlined in the section 2.5. Here I discuss the EELS measurements which were conducted to characterize the liquid layer thickness and the model samples which were utilized to determine the resolution capabilities of the developed system.

3.1 Instrumentation and model sample specimens utilized in this thesis

3.1.1 Transmission electron microscopy

In this thesis a number of electron microscopes were utilized to test the developed instrumentation and obtain data for analysis. All LC-TEM experiments were performed at the CCEM in Hamilton, Ontario. At this facility, two primary TEMs were utilized, a Talos 200X and a Titan HB.

The CCEM's Talos 200X is equipped with a high-brightness Schottky-type X-FEG and was operated at 200 keV for all experiments. This microscope is equipped with a CETA 16M complementary metal-oxide semiconductor (CMOS) camera and a Gatan imaging filter (GIF) Continuum S EELS and energy filtered transmission electron microscope (EFTEM) detector system which is equipped with a high dynamic range CMOS detector.

The CCEM's Titan HB was equipped with an X-FEG electron gun and was operated at 300 keV for all experiments. This microscope was outfitted with an UltiMono monochromator, with probe and image aberration correctors from Corrected Electron Optical Systems (CEOS). An Ultrascan charge-coupled device (CCD) camera and a GIF Quantum from Gatan was installed in this tool. This tool has since been replaced with a Thermo-Fisher

Spectra Ultra microscope.

3.1.2 Instrumentation for liquid-cell transmission electron microscopy measurements

The loading station, NFC electron microscope sample holder, and NFCs were developed at the UeIL at the University of Waterloo. Design of the loading station and NFC electron microscope sample holder was done personally with the use of Solidworks CAD software under the advisory supervision of Dr. Ariel Petruk and Prof. Germán Sciaini. Machining was performed and completed by precision machinists at STS at the University of Waterloo. NFCs were nanofabricated at the University of Waterloo QNFCF by Dr. Ariel Petruk, with assistance from myself and Nicki Shaw. The NFCs utilized for the presented images and data were produced with defined spacers of approximately 100 nm, 180 nm, 550 nm, and 630 nm. The SiN_x windows were produced with window dimensions of $\approx$ 20 µm $\times$ 300 µm and a thickness of 30 nm. Individual chips were always assembled to form a complete NFC, ensuring that the length of one window always overlapped perpendicularly with the width of the other. To counter alignment errors imposed by machining tolerances, this assembly process ensures that the two NFC windows are always overlapped in the formed NFC.

3.1.3 Model systems for measurements

Gold (Au) nanorods: 1 optical density (OD) nanoXact monodisperse Au nanorods (40 nm × 15 nm, sodium citrate capping agent) dispersed in United States Pharmacopeia (USP) grade purified water were purchased from nanoComposix Inc. (San Diego, CA) and were used as prepared without dilution. Approximately 400 nL (nominal volume) of this solution was dispensed onto the surface of a small nanofluidic chip (placed in the lid of the NFC holder during the loading process). The sample was sealed within the NFC assembly using the loading station and method described herein.

Polystyrene (PS) nanospheres: 10 milligrams (mg) per millilitre (mL) colloidal PS nanospheres (100 nm diameter, non-functionalized surface) dispersed in Milli-Q ultrapure water were purchased from ALPHA Nanotech (Vancouver, B.C.) and were diluted prior to imaging (1:25) in 18.2 megaohm (MΩ)-centimetre (cm) ultra-purified water. This solution was aspirated with a micropipette before sample delivery. Approximately 400 nL (nominal volume) of this solution was dispensed onto the surface of a small nanofluidic chip (placed in the lid of the NFC holder during the loading process). The sample was sealed within the NFC assembly using the loading station and method described herein.

DOPC Liposomes: 1,2-dioleoyl-sn-glycero-3-phosphocholine (DOPC) phospholipid was purchased from Avanti Polar Lipids (Alabaster, AL). 4-(2-hydroxyethyl)-1-piperazine-

ethanesulfonic acid (HEPES) was purchased from Sigma-Aldrich. Sodium chloride (NaCl) was purchased from Mandel Scientific (Guelph, ON). Milli-Q ultrapure water was used to prepare all samples. DOPC liposomes were prepared using the standard extrusion method. DOPC lipid (2.5 mg) was dissolved in chloroform (100 microlitres (µL)). After evaporating chloroform by gently blowing with nitrogen to form a thin film, the film was dried in a vacuum oven at room temperature overnight to fully remove residual chloroform. The dried lipid film was stored at -20 °C in a nitrogen atmosphere prior to use. To prepare liposomes, the lipid films were hydrated with 0.5 mL buffer (10 millimolar (mM) HEPES, pH 7.6, with 100 mM NaCl) yielding a lipid concentration of 5 mg per mL. The resulting cloudy suspension was extruded 21 times through two stacked polycarbonate membranes with a pore size of 100 nm to yield a clear liposome suspension. Approximately 400 nL (nominal volume) of this solution was dispensed onto the surface of a small nanofluidic chip (placed in the lid of the NFC holder during the loading process). The sample was sealed within the NFC assembly using the loading station and method described herein. Liposome samples were prepared and provided by Yibo Liu and Juewen Liu.

3.2 Electron beam transmission through liquids

In subsection 2.1.1, Equation: 2.1 - Equation: 2.3 provided a means to relate the transmission of the electron beam to material thickness. From these equations it can be shown that 10 nm of Si_3N_4 equates to approximately 40 nm of H_2O for acceleration voltages in the range of 100 to 300 keV as seen in Figure: 3.1.

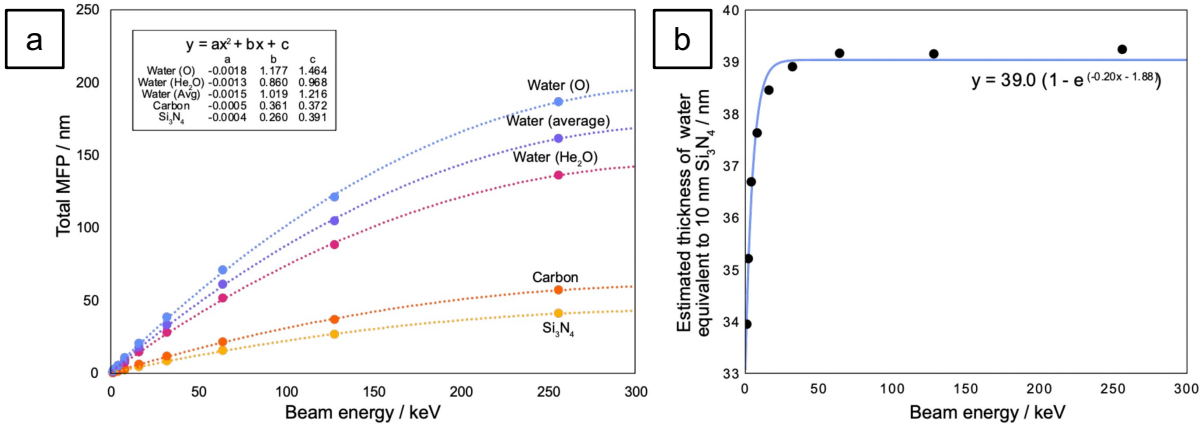


Figure 3.1: The contribution of water to electron beam transmission losses from total scattering cross section approximations. a) The total electron mean free path as a function of the electron beam energy.[63,67] The inset shows the parameters for the second order polynomial fits for each trendline (dotted lines). The Water (O) data was calculated using experimental oxygen data (assuming no contribution of hydrogen), where Water (He_2O) was modelled with experimental helium data in the place of hydrogen data.[67] Both were calculated using the number density of water of 1.0 gram cubic centimetre (g cm^{-3}). The density values of Carbon and Silicon Nitride (Si_3N_4) were taken to be 2.0 g cm^{-3}, and 3.2 g cm^{-3} respectively.[63,105] b) Calculated thickness of Water (average) equivalent in electron beam transmission to 10 nm Si_3N_4 as a function of electron beam energy. The blue line and equation depict the trend of the data. Reproduced with permission from T. S. Lott *et al.*, Robust Fully Controlled Nanometer Liquid Layers for High Resolution Liquid-Cell Electron Microscopy, *Lab Chip*, **23**, 3217-3225, (2023).[57]

These calculations highlight the importance of this method to not only minimize the thickness of the window membrane but more importantly the thickness of the liquid layer.

As we will see, optimization of the liquid layer is of key importance to achieving high transmission and resultantly high-resolution in LC-TEM experiments.

3.3 Membrane deformation and liquid layer thickness measurements

As outlined in subsection 2.1.2, EELS may be used to quantify the liquid layer thickness within an LC-TEM experiment. Previous measurements have been conducted to characterize the membrane bulging and the thickness of the assembled NFCs while abiding by the aspect ratio guidelines discussed earlier in section 2.5. In order to accomplish this task, compressed gas and a contact profilometer were utilized to determine the maximum deformation which occurs at the centre of a 25 nm thick SiN_x membrane as a function of the width of the membrane and the pressure differential across the membrane area. These deformation measurements are illustrated in Figure: 3.2.[56,57]

These measurements confirm that the width of the SiN_x window must be regulated to minimize deformation under an applied differential such as the one experienced by the NFCs within the column of the electron microscope.[64,103] Additionally, these measurements were utilized as a guide for the development of future generations of the NFCs so that a compromise could be made between limiting membrane bulging and maximizing the

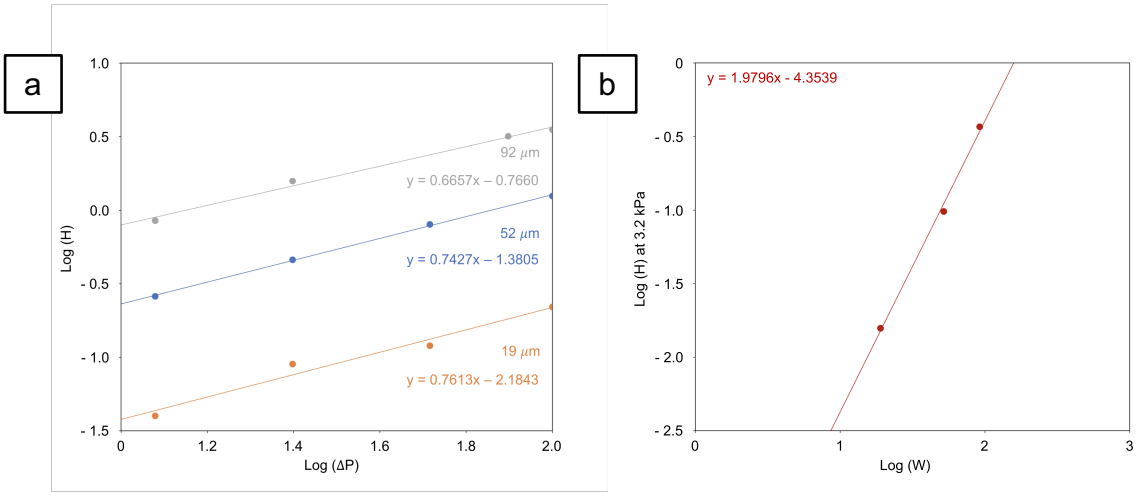


Figure 3.2: Silicon nitride window membrane deformation measurements for 25 nanometre (nm) thick membranes. a) A base-10 logarithmic plot illustrating the maximum deformation (H) in microns for windows wih widths (W) of 92 micrometres (μm) (grey), 52 μm (blue), and 19 μm (orange). b) A base-10 logarithmic plot with ΔP = 3.2 kilopascals (kPa) (the vapour pressure of pure water at 25 °C) showing the dependence of the maximum deformation on the width of the window membrane.[102] Reproduced with permission from T. S. Lott *et al.*, Robust Fully Controlled Nanometer Liquid Layers for High Resolution Liquid-Cell Electron Microscopy, *Lab Chip*, **23**, 3217-3225, (2023).[57]

viewable area within the NFC during the course of an experiment. The conclusion of these measurements is that an approximately 20 μm wide SiN_x membrane was found to have a maximum deformation of approximately 15 nm under a pressure differential equal to the vapour pressure of water at 25 °C (ΔP = 3.2 kilopascals (kPa)). Comparatively, the maximum deformation was found to be approximately 220 nm in the standard pressure of the laboratory environment at 25 °C (ΔP = 100 kPa). Therefore, finding a means to reduce the pressure differential between the interior of the NFC and microscope column where LC-TEM experiments take place is of primary importance. Despite these results being obtained for single films and not complete NFC assemblies, they are indeed comparable with the

calculations shown in Figure: 2.18 with the caveat that these pressurized air measurements are upper limits of the expected deformation which could occur in a liquid saturated NFC. Together, these results suggest that the maximum membrane bulging due to the pressure differential can be reduced from hundreds of nanometres to tens of nanometres with the use of the developed technology and the loading station method.

To provide confirmation that the developed instrumentation for LC-TEM measurements indeed confers negligible window membrane bulging and to quantify the effective liquid layer thickness, EELS measurements were conducted in the electron microscope. Utilizing the log-ratio method discussed in subsection 2.1.2, the thickness of liquid layers was characterized using EELS line scans in the corners of assembled NFCs which contained ultrapure water. An electron micrograph which illustrates the typical line scan region utilized for thickness measurements is shown in Figure: 3.3.

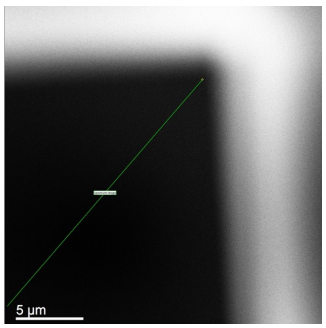


Figure 3.3: A high-angle annular dark field image showing a representative line scan region for liquid thickness measurements. The green line indicates the position of the line scan within the area indicated in the electron micrograph. Reproduced with permission from T. S. Lott *et al.*, Robust Fully Controlled Nanometer Liquid Layers for High Resolution Liquid-Cell Electron Microscopy, *Lab Chip*, **23**, 3217-3225, (2023).[57]

EELS spectra are shown in Figure: 3.4 where the electron intensities utilized for the log-ratio method for liquid layer thickness determination are highlighted. EELS measurements to determine the liquid layer thickness were conducted as line scans in order to illustrate the high degree of uniformity present across the viewing area.

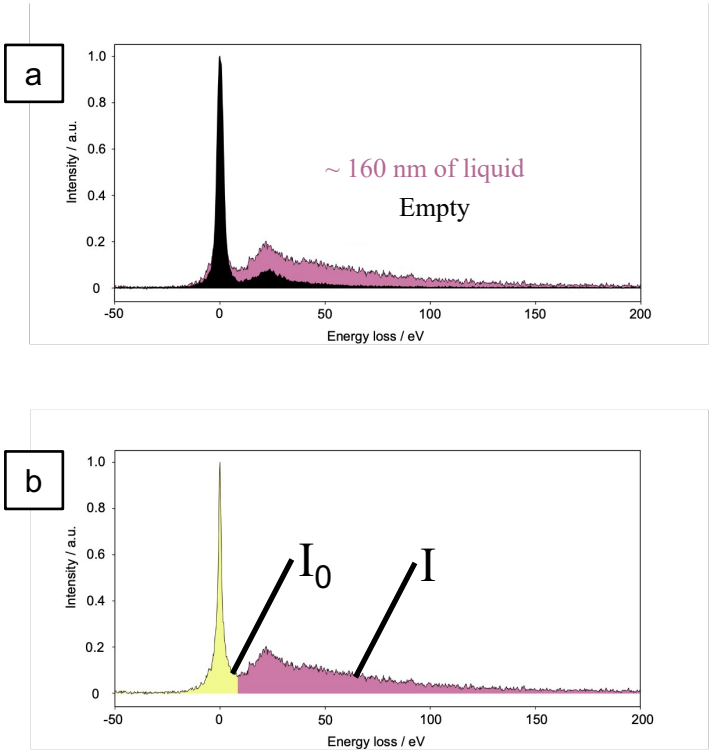


Figure 3.4: Using the log-ratio method to determine the liquid layer thickness in a liquid-cell transmission electron microscopy (LC-TEM) experiment. a) Electron energy loss spectroscopy (EELS) spectra obtained in a Titan HB showing the intensity difference in a nanofluidic cell (NFC) filled with ~ 160 nm of liquid water (pink) and an empty (black) NFC. b) The liquid-layer thickness was determined using the log-ratio method with the zero-loss peak (ZLP) and full spectrum areas calculated using Simpson's method. The area of the ZLP was determined by integrating the spectrum in the area indicated in yellow. Similar results were obtained by fitting the ZLP with a Gaussian function. Reproduced with permission from T. S. Lott *et al.*, Robust Fully Controlled Nanometer Liquid Layers for High Resolution Liquid-Cell Electron Microscopy, *Lab Chip*, **23**, 3217-3225, (2023).[57]

Four independent measurements were conducted for NFCs with various nominal liquid layer thicknesses as defined by the spacer height. These results are highlighted in Figure: 3.5. The obtained liquid layer thicknesses were in the range of 40 nm to 160 nm which is ideal for high-resolution LC-TEM measurements. In each of these four cases, it was observed that the thickness of the liquid layer was below the nominal liquid layer thickness as set by the spacer height. Furthermore, a small degree of membrane bulging occurred for smaller spacers (eg. spacer heights less than 200 nm) and negligible bulging for larger spacers (eg. spacer heights greater than 500 nm).

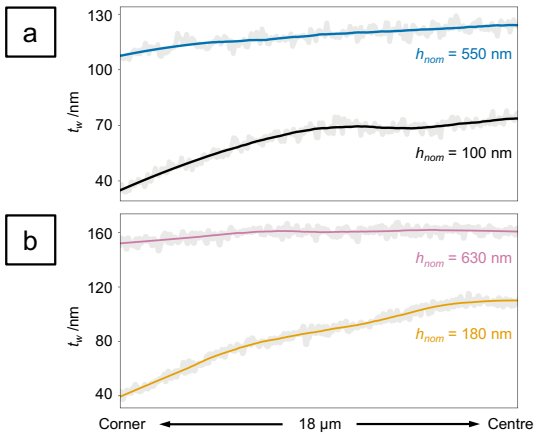


Figure 3.5: Liquid layer thickness measurements conducted with ultrapure water. a), b) Electron energy loss spectroscopy (EELS) line scan profiles quantifying the thickness (t_w) of ultrapure water layers performed from the corner of the viewing area to the centre as a function of the nominal liquid layer thickness as set by the spacer height (h_{nom}) of the nanofluidic cells (NFCs). Grey traces correspond to the raw acquired data while coloured traces correspond to Savitzky-Golay data-smoothing of the raw data. a) Data for these line scans were collected using a Talos 200X at 200 kiloelectron volts (keV) with an h_{nom} of 100 nanometres (nm) and 550 nm. b) Data for these line scans were collected using a Titan HB at 300 keV with an h_{nom} of 180 nm and 630 nm. Reproduced with permission from T. S. Lott *et al.*, Robust Fully Controlled Nanometer Liquid Layers for High Resolution Liquid-Cell Electron Microscopy, *Lab Chip*, **23**, 3217-3225, (2023).[57]

This was unexpected behaviour but it can be explained by investigating the assembled structure of the NFCs as seen in Figure: 3.6.

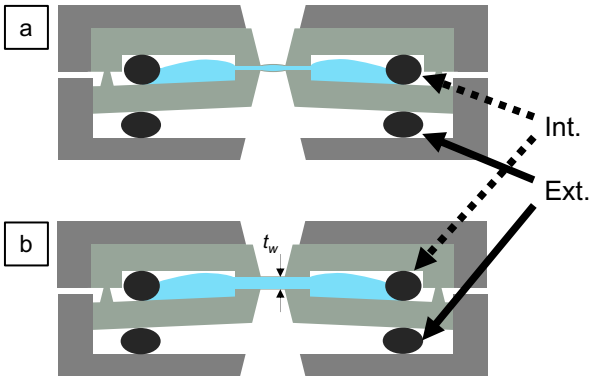


Figure 3.6: Bowing of nanofluidic cells (NFCs) observed through electron energy loss spectroscopy (EELS) measurements. a), b) Illustration of the cross-sectional view of the assembled NFC in the tip of the electron microscopy holder. The external o-ring (Ext.) has a higher durometer than the internal o-ring (Int.) and is compressed to a larger extent in this design to ensure the contact between the surfaces which define h_{nom}. Due to the difference in durometer and the compression imposed on the external o-ring, there is a net force which causes bowing of the bottom NFC chip and leads to $t_w > h_{nom}$. As seen in a), for small spacers (eg. $h_{nom} < 200$ nanometres (nm)) this bowing of the chip leads to liquid encapsulation and a slight amount of membrane bulging. As seen in b), for larger spacers (eg. $h_{nom} < 500$ nm) this bowing of the chip is negligible. Reproduced with permission from T. S. Lott *et al.*, Robust Fully Controlled Nanometer Liquid Layers for High Resolution Liquid-Cell Electron Microscopy, *Lab Chip*, **23**, 3217-3225, (2023).[57]

The NFC design relies on the contact of the spacer material which is embedded in each chip in order to enclose the desired amount of liquid for a given experiment. In this design, it is critical to ensure that the surfaces defining the spacer height get into contact as the internal o-ring compresses into a predefined cavity. Therefore, an external o-ring was chosen such that it would experience a higher degree of compression while also possessing a higher durometer than the o-ring which is internally hermetically sealing the

NFC. Additionally, this high compression of the external o-ring ensured that tolerances in the machining (eg. two thousandths of an inch or $\sim$ 50 μm) and commercial o-rings (eg. three thousandths of an inch or $\sim$ 75 μm) did not create a situation where the NFC would be insufficiently sealed. Once the NFC assembly has been formed using the loading station, the compression of this external o-ring leads to a net force that causes bowing in the chip which rests in the tip of the electron microscopy holder. This force leads to the trapping of liquid within the SiN_x membranes for spacer heights less than 200 nm. This behaviour led to the observation of enhanced nanoparticle motion in the centre of the viewing area versus the corner of the viewing area for the particles imaged in Figure: 3.7. For larger spacers, the maximum amount of bowing in the chip appears to be 400 - 500 nm. Given the tolerances in machining and the cross-sections of the miniature o-rings this number is prone to some degree of variation. The thinnest liquid layers of roughly 40 nm are perhaps limited by the compression of the liquid in this configuration. Surface treatments as discussed earlier, can influence the hydrophilicity of the SiN_x surface. For these measurements, in addition to external plasma cleaning of the holder, only the chip which resides in the lid of the electron microscope holder had its window membrane plasma cleaned. This cleaning procedure was found to produce desirable positioning of the sample liquid droplet during dropcasting in addition to conferring high-resolution images across the complete viewing area of the NFC. These results also agree with the expected deformation as predicted from Figure: 2.18 and

Figure: 3.2 where window membrane bulging is of the order of tens of nanometres.

3.4 Imaging model sample specimens in situ

To test the efficacy of the developed NFCs and loading station system, a handful of model sample specimens were selected for observation in the electron microscope. Citrate stabilized gold (Au) nanorods with a diameter of 15 nm and a length of 40 nm were chosen for imaging on account of gold's well known ability to give high contrast images. Gold is often selected as a calibrant for high-resolution imaging, especially STEM where the high atomic number of gold is ideal for HAADF imaging. The synthesis of these particles is also refined to provide in-plane atomic lattice resolution. Polystyrene (PS) nanospheres with a diameter of 100 nm were implemented as a model sample specimen for low atomic number materials to illustrate that high-contrast imaging for this type of material is possible in LC-TEM if the liquid layer thickness is comparable to the size of the particle being imaged. Lastly, 1,2-dioleoyl-sn-glycero-3-phosphocholine (DOPC) liposomes were imaged to demonstrate the potential for bio-imaging in LC-TEM with the system developed here. All samples were loaded as discussed in section 2.5 and thereafter immediately taken to the electron microscope for imaging.

To illustrate that the developed method affords high-resolution imaging across the

complete viewing area of the NFC, images near the edge and the centre of the viewing area were captured using an NFC with a nominal spacer height of 180 nm. This result is illustrated in Figure: 3.7.

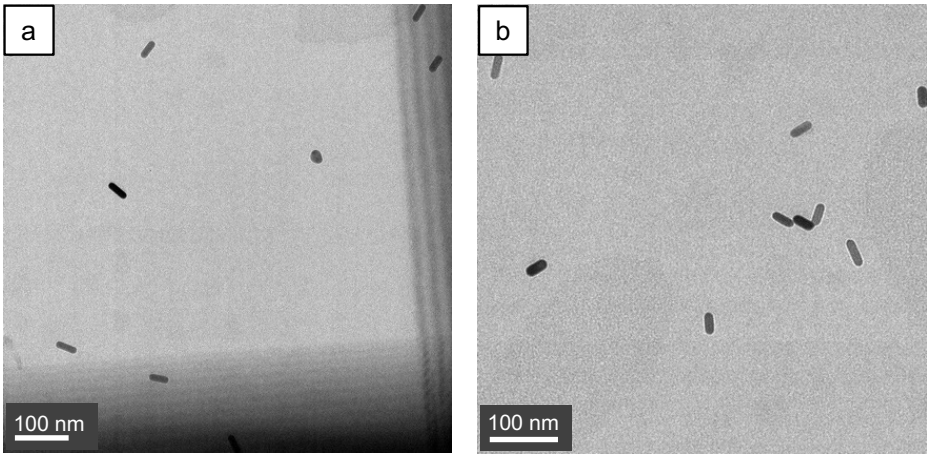


Figure 3.7: Demonstrating the uniformity of the liquid layer thickness across the viewing area of the nanofluidic cell (NFC). a) An *in-situ* transmission electron micrograph of gold nanorods obtained near the corner of an assembled NFC. This image was taken near the corner of the viewing area at a magnification of 74 thousand times (kx) under a dose rate of approximately 15 electrons angstroms squared per second ($Å^2$ s^{-1}). b) An *in-situ* transmission electron micrograph of gold nanorods obtained near the centre of an assembled NFC. This image was taken near the centre of the viewing area at a magnification of 94 kx under a dose rate of approximately 25 electrons $Å^2$ s^{-1}. Both images were obtained in a Talos 200X operating at 200 kiloelectron volts (keV). NFC chips utilized in this experiment had silicon nitride (SiN_x) windows with a thickness of 30 nanometres (nm) and a viewing area of approximately 20 micrometres (µm) × 20 µm. Reproduced with permission from T. S. Lott *et al.*, Robust Fully Controlled Nanometer Liquid Layers for High Resolution Liquid-Cell Electron Microscopy, *Lab Chip*, **23**, 3217-3225, (2023).[57]

Line profiles taken of the gold nanorods in Figure: 3.7 indicate a resolution of ∼ 1 nm across the complete viewing area of the NFC. As discussed in chapter 2, the presence of bulging due to conventional NFC assembly methods is known to degrade the image quality in the centre of the viewing area. As expected with the designed instrumentation and methodology, any bulging present is negligible and does not contribute to significant

degradation of image quality. These results correlate with the results obtained in section 3.3 where the bulging observed is minimal and a significant improvement from conventional NFCs. Of note here is the observation of enhanced particle motion when observations were made moving from the edge to the centre of the viewing area. This observation again correlates with the slight increases in the liquid layer thickness which is ascribed to the liquid encapsulation that was observed for nominal spacer heights less than 200 nm in this generation of NFCs, a behaviour which may be improved in future generations of the technology.

However, regardless of the nominal spacer height (100 nm - 630 nm) utilized for experiments, high-quality images were obtained using both TEM and STEM imaging. HAADF-STEM images are shown in Figure: 3.8. Therefore, the developed method can successfully be utilized to image both nanomaterials and biospecimens in the STEM imaging mode which is generally more sensitive to high atomic number materials. In addition, Figure: 3.8b displays a bright contrast around each collection of PS nanospheres. This behaviour has not been thoroughly investigated but it is possible that the observed contrast is due to charging of the PS insulating material which also explains the degradation in resolution in the image.[106]

To quantify the obtainable spatial resolution of the developed method and instrumentation in a high-acceleration voltage instrument, line intensity profile measurements were

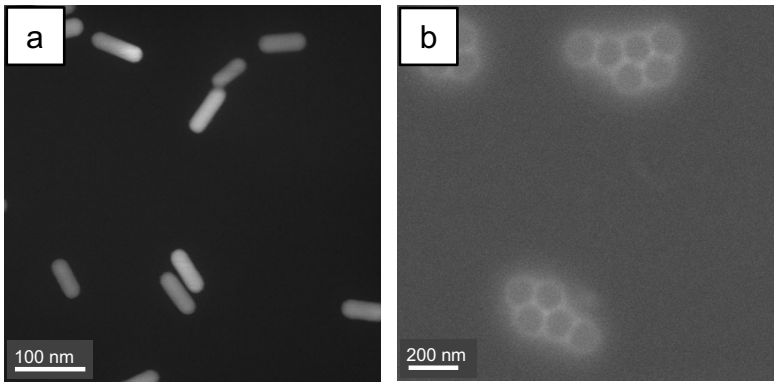


Figure 3.8: Demonstrating high-resolution scanning transmission electron microscopy (STEM) imaging *in situ*. a) High-angle annular dark field (HAADF) STEM images of gold nanorods obtained near the centre of the viewing area of the developed nanofluidic cell (NFC) assembly with a nominal spacer height of 100 nanometres (nm). b) High-angle annular dark field (HAADF) STEM images of polystyrene (PS) nanospheres obtained near the centre of the viewing area of the developed NFC assembly with a nominal spacer height of 550 nm. Both images were obtained in a Talos 200X operating at 200 kiloelectron volts (keV). NFC chips utilized in this experiment had silicon nitride (SiN_x) windows with a thickness of 30 nm and a viewing area of approximately 20 micrometres (µm) × 20 µm. Reproduced with permission from T. S. Lott *et al.*, Robust Fully Controlled Nanometer Liquid Layers for High Resolution Liquid-Cell Electron Microscopy, *Lab Chip*, **23**, 3217-3225, (2023).[57]

conducted on a gold nanorod *in-situ*, imaged in the centre of a NFC assembly in the TEM mode. These results are illustrated in Figure: 3.9. The measured 20 - 80 % line-intensity profile indicates that a resolution of approximately 0.9 nm was obtained as an upper limit of the spatial resolution where a relatively slow CCD camera with a frame rate of 500 ms was utilized.

Images of unstained DOPC liposomes were also obtained at 200 kV. This model sample is of particular interest as it normally necessitates the use of contrast agents for imaging in conventional TEM measurements.[107,108] Often materials such as this one are imaged through cryo-electron microscopy (Cryo-EM) but the use of LC-TEM for the imaging of

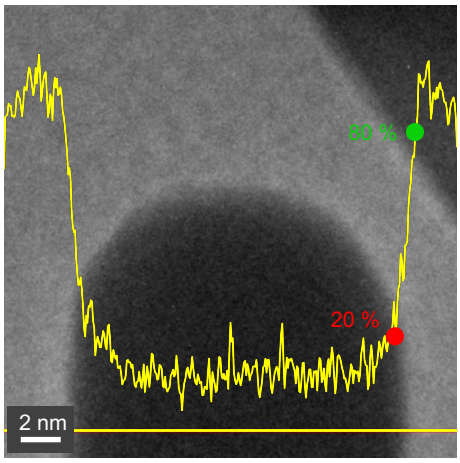


Figure 3.9: A line-intensity profile measurement of a gold nanorod located at the centre of the nanofluidic cell (NFC) assembly. This image was obtained in a Titan HB operating at 300 kiloelectron volts (keV). NFC chips utilized in this experiment had silicon nitride (SiN_x) windows with a thickness of 30 nanometres (nm) and a viewing area of approximately 20 micrometres (µm) × 20 µm. The spacer height of this NFC assembly was 100 nm. This image was taken near the centre of the viewing area at a magnification of 450 thousand times (kx) under a dose rate of approximately 7000 electrons angstroms squared per second ($Å^2\ s^{-1}$). Reproduced with permission from T. S. Lott *et al.*, Robust Fully Controlled Nanometer Liquid Layers for High Resolution Liquid-Cell Electron Microscopy, *Lab Chip*, **23**, 3217-3225, (2023).[57]

these specimens is quickly growing.[109–112] However, the preparation of liposome samples in conventional LC-TEM approaches generally does not confer uniform liquid layer thicknesses across the complete viewing area to offer well-defined liquid layer thicknesses for imaging. Electron beam induced sample damage occurs over a timescale of roughly a minute from the start of imaging to the disappearance of liposomes. DOPC liposomes imaged with the developed method are indicated in Figure: 3.10.

The liposomes appeared to remain relatively stationary throughout the imaging period which is attributed to confinement of the sample within the thin liquid layer which had a thickness comparable to the 100 nm diameter of the liposomes. This behaviour is similar

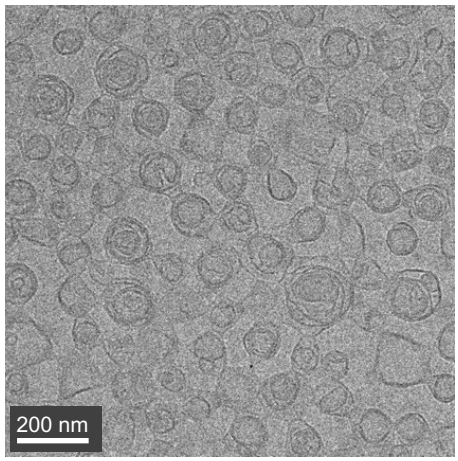


Figure 3.10: Imaging unstained liposomes *in situ*. Imaging was performed on a Talos 200X operating at 200 kiloelectron volts (keV). NFC chips utilized in this experiment had silicon nitride (SiN_x) windows with a thickness of 30 nanometres (nm) and a viewing area of approximately 20 micrometres (µm) × 20 µm. The spacer height of this NFC assembly was 100 nm. This image was taken near the centre of the viewing area at a magnification of 22 thousand times (kx) under a dose rate of approximately 1.5 electrons angstroms squared per second ($Å^2\ s^{-1}$). Reproduced with permission from T. S. Lott *et al.*, Robust Fully Controlled Nanometer Liquid Layers for High Resolution Liquid-Cell Electron Microscopy, *Lab Chip*, **23**, 3217-3225, (2023).[57]

to behaviour observed by others researching liposomes *in situ*.[111] Also worth noting is the appearance of a multi-layered structure which can perhaps be attributed to the relatively low energy barrier for membrane fusion for phosphocholine lipids.[113]

To further illustrate the capabilities of the developed technology and method, we conducted further measurements in the TEM mode to observe the atomic lattice of gold nanorods in solution. In order to capture lattice resolution images in LC-TEM, extremely thin layers are required such that the electron scattering of the beam is significantly reduced and the specimen of interest is forced into a pseudo-stationary position where Brownian motion is minimized. These conditions were successfully satisfied for the gold nanorods

imaged in Figure: 3.11. Confinement of the gold nanorods in this experiment was accomplished by utilizing a nominal spacer height of 100 nm. It is likely that the gold nanorods experienced enhanced interaction with one of the windows upon electron beam induced disruption of the stabilizing citrate capping agent which coats the gold nanorods.[114]

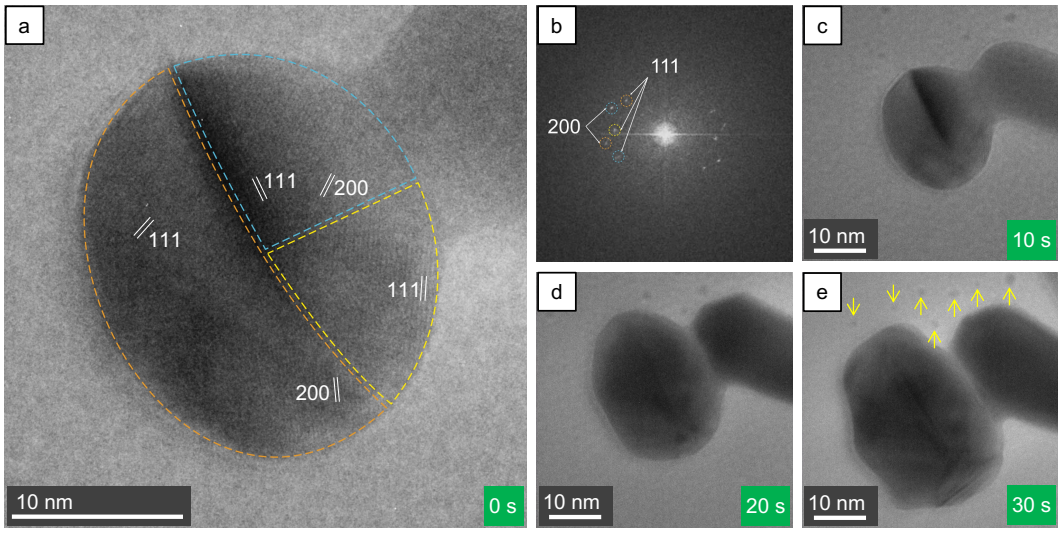


Figure 3.11: High-resolution images of gold nanorods in solution. a) A transmission electron micrograph of gold nanorods where the (200) and (111) lattice planes of gold were identified with interplane distances of approximately 0.20 nanometres (nm) and 0.23 nm respectively. Analysis revealed that this particular nanorod is comprised of three crystallites with their approximate interfaces delineated by dashed lines. To define the time origin, this image was arbitrarily selected. b) A fast Fourier transform of the image shown in a) with the diffraction spots corresponding to the (200) and (111) gold lattice planes. The colours indicated here correlate with the crystallites shown in a). c)-e) A sequence of transmission electron micrographs of the same gold nanorod shown in a) depicting nanoparticle growth. Yellow arrows in e) indicate small gold clusters on the order of 1-2 nm. Timestamps for all images are indicated in the bottom right corner of each image. Imaging was performed on a Titan HB operating at 300 kiloelectron volts (keV). Nanofluidic cell (NFC) chips utilized in this experiment had silicon nitride (SiN_x) windows with a thickness of 30 nm and a viewing area of approximately 20 micrometres (µm) × 20 µm. The spacer height of this NFC assembly was 100 nm. This image was taken near the centre of the viewing area at a magnification of 600 thousand times (kx) under a dose rate of approximately 12000 electrons angstroms squared per second ($Å^2\ s^{-1}$). Reproduced with permission from T. S. Lott *et al.*, Robust Fully Controlled Nanometer Liquid Layers for High Resolution Liquid-Cell Electron Microscopy, *Lab Chip*, **23**, 3217-3225, (2023).[57]

Despite the limited frame rate and signal to noise of the employed CCD electron detector compared to more advanced detectors such as a direct electron detector, the (200) and (111) gold lattice planes with interplane distances of approximately 0.20 nm and 0.23 nm respectively were clearly observed. As imaging progressed, the lattice planes were found to appear and disappear due to the electron beam induced motion of the gold nanorods. The observation of crystallite regions on the gold nanorods indicates that high-resolution data acquisition is obtainable in solution in a matter of minutes, following the methodology presented here. Multiple crystallites in these images also suggest that the electron beam induced particle-particle sintering and particle dissolution over the course of imaging. In addition, the presence of 1-2 nm gold clusters were clearly observed in this experiment. The Au_{13} cluster has a size of approximately 0.85 nm.[61,115] Thus, the demonstrated method and technology therefore has the ability to resolve nanoclusters which may be seed for the observed growth shown in Figure: 3.11.[61,115,116]

Chapter 4

Conclusion

4.1 Conclusion

In this thesis a complete suite of instrumentation was presented which was designed and produced for the preparation of NFCs with the absence of bulging for LC-TEM. Using SolidWorks CAD software, a unique LC-TEM NFC holder and sample loading station was designed and produced to be used in conjunction with proprietary NFCs. The work in this thesis has led to the development of prototypes of the described technology for FEI, Hitachi, and JEOL electron microscopes. Using this instrumentation, the challenge of producing thin liquid layers for observation in the TEM was resolved, achieving lattice resolution and uniform thin liquid layers across the complete viewing area of the NFC.

Using EELS measurements on ultrapure water within NFCs assembled using the designed instrumentation and methodology, the liquid layer thickness was characterized to confirm that the developed NFCs confer uniform thin liquid layers for imaging. Liquid layers with thicknesses of approximately 40 nm to 160 nm were established in NFCs with nominal spacer heights of 100 nm, 180 nm, 550 nm, and 630 nm. Furthermore, the technology demonstrated the ability to form uniform liquid layers across the complete viewing area of the developed NFCs with negligible bulging. The resolution capabilities of this method were tested with model sample specimens of gold nanorods, PS nanospheres, and DOPC liposomes. Lattice resolution images were obtained in imaging the gold nanorods, while the imaging of PS nanospheres and DOPC liposomes provided confirmation that low contrast materials and biospecimens are suitable for imaging in LC-TEM if imaging is performed in highly uniform thin liquid layers. This development solves a long-lasting issue which has impacted the attainable resolution in the field of LC-TEM.

Chapter 5

Outlook

5.1 Outlook

The technology developed in this thesis opens up new opportunities to perform high-resolution imaging in LC-TEM by removing a key barrier on the path to obtaining high-quality data. In addition, the enhanced through-put provided by this technology will open opportunities for researchers to perform more experiments and collect more data during a standard TEM imaging session. Furthermore, this air-free sample preparation methodology is broadly applicable to facilitate the assembly of not only SiN_x based NFC designs but also other types of NFCs such as those made with graphene windows, which are also susceptible to air encapsulation and bulging. The impact of this method on the observation

of sample specimens is particularly promising in the case of bio-imaging as seen with the preliminary results of DOPC liposome imaging. These results are poised to improve with the implementation of thinner SiN_x window membranes which are already in development and initial testing at the UeIL. In combination with the development of novel approaches in data analysis and image processing in the field of LC-TEM,[3] the instrumentation and methodology presented in this thesis provides an approach to producing ideal conditions for LC-TEM, with the ambition to advance the field in the elucidation of natural processes occurring at the nanoscale and below.

On-going work in the field of LC-TEM continues to focus on minimizing the role that the electron beam has on influencing the interpretation of natural processes of interest occurring *in situ*. To further aid these efforts, researchers will require not only faster electron detectors and the rapid availability of aberration-corrected lenses, but in addition, pulsed electron sources should be utilized.[117,118] The utilization of phase plates and the advancement in this technology will allow for an improved imaging toolkit, particularly in the case of bio-imaging.[119] These efforts will not only improve the obtainable spatial resolutions of objects in the liquid phase but also reduce the required electron dose for sufficient resolution of desired features.[119]

References

(1) Yuk, J. M.; Park, J.; Ercius, P.; Kim, K.; Hellebusch, D. J.; Crommie, M. F.; Lee, J. Y.; Zettl, A.; Alivisatos, A. P. High-Resolution EM of Colloidal Nanocrystal Growth Using Graphene Liquid Cells. *Science* **2012**, *336*, Publisher: American Association for the Advancement of Science, 61–64.

(2) Jokisaari, J. R.; Hachtel, J. A.; Hu, X.; Mukherjee, A.; Wang, C.; Konecna, A.; Lovejoy, T. C.; Dellby, N.; Aizpurua, J.; Krivanek, O. L.; Idrobo, J.-C.; Klie, R. F. Vibrational Spectroscopy of Water with High Spatial Resolution. *Advanced Materials* **2018**, *30*, 1802702.

(3) Yao, L.; Ou, Z.; Luo, B.; Xu, C.; Chen, Q. Machine Learning to Reveal Nanoparticle Dynamics from Liquid-Phase TEM Videos. *ACS Central Science* **2020**, *6*, Publisher: American Chemical Society, 1421–1430.

(4) Gilmore, B. L.; Showalter, S. P.; Dukes, M. J.; Tanner, J. R.; Demmert, A. C.; McDonald, S. M.; Kelly, D. F. Visualizing viral assemblies in a nanoscale biosphere. *Lab on a Chip* **2012**, *13*, Publisher: The Royal Society of Chemistry, 216–219.

(5) Khelfa, A.; Nelayah, J.; Amara, H.; Wang, G.; Ricolleau, C.; Alloyeau, D. Quantitative In Situ Visualization of Thermal Effects on the Formation of Gold Nanocrystals in Solution. *Advanced Materials* **2021**, *33*, 2102514.

(6) Ianiro, A.; Wu, H.; van Rijt, M. M. J.; Vena, M. P.; Keizer, A. D. A.; Esteves, A. C. C.; Tuinier, R.; Friedrich, H.; Sommerdijk, N. A. J. M.; Patterson, J. P. Liquid–liquid phase separation during amphiphilic self-assembly. *Nature Chemistry* **2019**, *11*, Number: 4 Publisher: Nature Publishing Group, 320–328.

(7) Abbe, E. Beiträge zur Theorie des Mikroskops und der mikroskopischen Wahrnehmung. *Archiv für Mikroskopische Anatomie* **1873**, *9*, 413–468.

(8) Rayleigh, L. XII. On the manufacture and theory of diffraction-gratings. *The London, Edinburgh, and Dublin Philosophical Magazine and Journal of Science* **1874**, *47*, 81–93.

(9) Prakash, K.; Diederich, B.; Heintzmann, R.; Schermelleh, L. Super-resolution microscopy: a brief history and new avenues. *Philosophical Transactions of the Royal*

Society A: Mathematical, Physical and Engineering Sciences **2022**, *380*, Publisher: Royal Society, 20210110.

(10) Ortega Arroyo, J.; Cole, D.; Kukura, P. Interferometric scattering microscopy and its combination with single-molecule fluorescence imaging. *Nature Protocols* **2016**, *11*, Number: 4 Publisher: Nature Publishing Group, 617–633.

(11) Lelek, M.; Gyparaki, M. T.; Beliu, G.; Schueder, F.; Griffié, J.; Manley, S.; Jungmann, R.; Sauer, M.; Lakadamyali, M.; Zimmer, C. Single-molecule localization microscopy. *Nature Reviews Methods Primers* **2021**, *1*, Number: 1 Publisher: Nature Publishing Group, 1–27.

(12) Schermelleh, L.; Ferrand, A.; Huser, T.; Eggeling, C.; Sauer, M.; Biehlmaier, O.; Drummen, G. P. C. Super-resolution microscopy demystified. *Nature Cell Biology* **2019**, *21*, Number: 1 Publisher: Nature Publishing Group, 72–84.

(13) Taylor, R. W.; Sandoghdar, V. Interferometric Scattering Microscopy: Seeing Single Nanoparticles and Molecules via Rayleigh Scattering. *Nano Letters* **2019**, *19*, 4827–4835.

(14) Prozorov, T.; Almeida, T. P.; Kovács, A.; Dunin-Borkowski, R. E. Off-axis electron holography of bacterial cells and magnetic nanoparticles in liquid. *Journal of The Royal Society Interface* **2017**, *14*, 20170464.

(15) Zeng, Z.; Zhang, X.; Bustillo, K.; Niu, K.; Gammer, C.; Xu, J.; Zheng, H. In Situ Study of Lithiation and Delithiation of MoS $_2$ Nanosheets Using Electrochemical Liquid Cell Transmission Electron Microscopy. *Nano Letters* **2015**, *15*, 5214–5220.

(16) Sutter, E. A.; Sutter, P. W. In situ liquid cell electron microscopy of Ag–Au galvanic replacement reactions. *Nanoscale* **2017**, *9*, Publisher: The Royal Society of Chemistry, 1271–1278.

(17) Creemer, J. F.; Helveg, S.; Kooyman, P. J.; Molenbroek, A. M.; Zandbergen, H. W.; Sarro, P. M. A MEMS Reactor for Atomic-Scale Microscopy of Nanomaterials Under Industrially Relevant Conditions. *Journal of Microelectromechanical Systems* **2010**, *19*, Conference Name: Journal of Microelectromechanical Systems, 254–264.

(18) Grogan, J. M.; Schneider, N. M.; Ross, F. M.; Bau, H. H. The Nanoaquarium: A New Paradigm in Electron Microscopy. *Journal of the Indian Institute of Science* **2012**, *92*, Number: 2, 295–308.

(19) Broglie, L. d. XXXV. A tentative theory of light quanta. *The London, Edinburgh, and Dublin Philosophical Magazine and Journal of Science* **1924**, *47*, 446–458.

(20) Chen, X.; Zheng, B.; Liu, H. Optical and Digital Microscopic Imaging Techniques and Applications in Pathology. *Analytical Cellular Pathology* **2011**, *34*, 5–18.

(21) Kohl, H.; Reimer, L., *Transmission Electron Microscopy: Physics of Image Formation, 5e*, 5th ed.; Springer Series in Optical Sciences; Springer: New York, NY, 2008.

(22) Thomas, R.; Gibson, J.; Haas, G.; Abrams, R. Thermionic sources for high-brightness electron beams. *IEEE Transactions on Electron Devices* **1990**, *37*, Conference Name: IEEE Transactions on Electron Devices, 850–861.

(23) Gomer, R. Field emission, field ionization, and field desorption. *Surface Science* **1994**, *299-300*, 129–152.

(24) Rosenauer, A.; Krause, F. F.; Müller, K.; Schowalter, M.; Mehrtens, T. Conventional Transmission Electron Microscopy Imaging beyond the Diffraction and Information Limits. *Physical Review Letters* **2014**, *113*, Publisher: American Physical Society, 096101.

(25) Chen, Z.; Jiang, Y.; Shao, Y.-T.; Holtz, M. E.; Odstrčil, M.; Guizar-Sicairos, M.; Hanke, I.; Ganschow, S.; Schlom, D. G.; Muller, D. A. Electron ptychography achieves atomic-resolution limits set by lattice vibrations. *Science* **2021**, *372*, Publisher: American Association for the Advancement of Science, 826–831.

(26) Rose, H. H.; Wan, W. Aberration Correction in Electron Microscopy. **2005**, Proceedings of 2005 Particle Accelerator Conference, Knoxville, Tennessee, 44–48.

(27) Kimoto, K. Practical aspects of monochromators developed for transmission electron microscopy. *Microscopy* **2014**, *63*, 337–344.

(28) Krivanek, O. L.; Lovejoy, T. C.; Dellby, N.; Aoki, T.; Carpenter, R. W.; Rez, P.; Soignard, E.; Zhu, J.; Batson, P. E.; Lagos, M. J.; Egerton, R. F.; Crozier, P. A. Vibrational spectroscopy in the electron microscope. *Nature* **2014**, *514*, Number: 7521 Publisher: Nature Publishing Group, 209–212.

(29) Scherzer, O. Über einige Fehler von Elektronenlinsen. *Zeitschrift für Physik* **1936**, *101*, 593–603.

(30) Rose, H. H. Optics of high-performance electron microscopes*. *Science and Technology of Advanced Materials* **2008**, *9*, 014107.

(31) Smith, D. J. Ultimate resolution in the electron microscope? *Materials Today* **2008**, *11*, 30–38.

(32) Shang, T.-T.; Liu, X.-Y.; Gu, L. Interface of transition metal oxides at the atomic scale. *Science China Physics, Mechanics & Astronomy* **2016**, *59*, 697001.

(33) Egerton, R., *Electron Energy-Loss Spectroscopy in the Electron Microscope*; Springer US: Boston, MA, 2011.

(34) Malis, T.; Cheng, S. C.; Egerton, R. F. EELS log-ratio technique for specimen-thickness measurement in the TEM. *Journal of Electron Microscopy Technique* **1988**, *8*, 193–200.

(35) Trebbia, P.; Bonnet, N. EELS elemental mapping with unconventional methods I. Theoretical basis: Image analysis with multivariate statistics and entropy concepts. *Ultramicroscopy* **1990**, *34*, 165–178.

(36) Ferrell, R. A. Characteristic Energy Loss of Electrons Passing through Metal Foils. II. Dispersion Relation and Short Wavelength Cutoff for Plasma Oscillations. *Physical Review* **1957**, *107*, 450–462.

(37) Hofer, F.; Schmidt, F. P.; Grogger, W.; Kothleitner, G. Fundamentals of electron energy-loss spectroscopy. *IOP Conference Series: Materials Science and Engineering* **2016**, *109*, Publisher: IOP Publishing, 012007.

(38) Bogner, A.; Jouneau, P. .-.; Thollet, G.; Basset, D.; Gauthier, C. A history of scanning electron microscopy developments: Towards "wet-STEM" imaging. *Micron* **2007**, *38*, 390–401.

(39) Haguenau, F.; Hawkes, P.; Hutchison, J.; Satiat–Jeunemaître, B.; Simon, G.; Williams, D. Key Events in the History of Electron Microscopy. *Microscopy and Microanalysis* **2003**, *9*, 96–138.

(40) De Jonge, N.; Ross, F. M. In *Liquid Cell Electron Microscopy*, Ross, F. M., Ed.; Advances in Microscopy and Microanalysis; Cambridge University Press: Cambridge, 2016, pp 3–34.

(41) Ruska, E. Beitrag zur übermikroskopischen Abbildung bei höheren Drucken. *Kolloid-Zeitschrift* **1942**, *100*, 212–219.

(42) Abrams, I. M.; McBain, J. W. A Closed Cell for Electron Microscopy. *Journal of Applied Physics* **1944**, *15*, Publisher: American Institute of Physics, 607–609.

(43) Williamson, M. J.; Tromp, R. M.; Vereecken, P. M.; Hull, R.; Ross, F. M. Dynamic microscopy of nanoscale cluster growth at the solid–liquid interface. *Nature Materials* **2003**, *2*, Number: 8 Publisher: Nature Publishing Group, 532–536.

(44) Barshack, I.; Polak-Charcon, S.; Behar, V.; Vainshtein, A.; Zik, O.; Ofek, E.; Hadani, M.; Kopolovic, J.; Nass, D. Wet SEM: A Novel Method for Rapid Diagnosis of Brain Tumors. *Ultrastructural Pathology* **2004**, *28*, 255–260.

(45) Krueger, M.; Berg, S.; Stone, D.; Strelcov, E.; Dikin, D. A.; Kim, J.; Cote, L. J.; Huang, J.; Kolmakov, A. Drop-Casted Self-Assembling Graphene Oxide Membranes for Scanning Electron Microscopy on Wet and Dense Gaseous Samples. *ACS Nano* **2011**, *5*, Publisher: American Chemical Society, 10047–10054.

(46) Zheng, H.; Smith, R. K.; Jun, Y.-w.; Kisielowski, C.; Dahmen, U.; Alivisatos, A. P. Observation of Single Colloidal Platinum Nanocrystal Growth Trajectories. *Science* **2009**, *324*, Publisher: American Association for the Advancement of Science, 1309–1312.

(47) Keskin, S.; Pawell, C.; de Jonge, N. Verification of water presence in graphene liquid cells. *Micron* **2021**, *149*, 103109.

(48) Hutzler, A.; Schmutzler, T.; Jank, M. P. M.; Branscheid, R.; Unruh, T.; Spiecker, E.; Frey, L. Unravelling the Mechanisms of Gold–Silver Core–Shell Nanostructure Formation by in Situ TEM Using an Advanced Liquid Cell Design. *Nano Letters* **2018**, *18*, Publisher: American Chemical Society, 7222–7229.

(49) Peckys, D. B.; Veith, G. M.; Joy, D. C.; Jonge, N. d. Nanoscale Imaging of Whole Cells Using a Liquid Enclosure and a Scanning Transmission Electron Microscope. *PLOS ONE* **2009**, *4*, Publisher: Public Library of Science, e8214.

(50) Hummingbird Scientific | In-Situ TEM Specimen Holders, Hummingbird Scientific https://hummingbirdscientific.com/ (accessed 09/14/2023).

(51) DENSsolutions - In situ Microscopy Innovative Solutions, DENSsolutions https://denssolutions.com/ (accessed 09/14/2023).

(52) Protochips | Advanced in situ TEM Solutions & Sample Supports, Protochips https://www.protochips.com/ (accessed 09/14/2023).

(53) Jensen, E.; Mølhave, K. In *Liquid Cell Electron Microscopy*, Ross, F. M., Ed.; Advances in Microscopy and Microanalysis; Cambridge University Press: Cambridge, 2016, pp 35–55.

(54) Holtz, M. E.; Yu, Y.; Gao, J.; Abruña, H. D.; Muller, D. A. In Situ Electron Energy-Loss Spectroscopy in Liquids. *Microscopy and Microanalysis* **2013**, *19*, Publisher: Cambridge University Press, 1027–1035.

(55) Jungjohann, K. L.; Evans, J. E.; Aguiar, J. A.; Arslan, I.; Browning, N. D. Atomic-Scale Imaging and Spectroscopy for In Situ Liquid Scanning Transmission Electron Microscopy. *Microscopy and Microanalysis* **2012**, *18*, Publisher: Cambridge University Press, 621–627.

(56) Petruk, A. A.; Allen, C.; Rivas, N.; Pichugin, K.; Sciaini, G. High flow rate nanofluidics for in-liquid electron microscopy and diffraction. *Nanotechnology* **2019**, *30*, Publisher: IOP Publishing, 395703.

(57) Lott, T. S.; Petruk, A. A.; Shaw, N. A.; Hamada, N.; Andrei, C. M.; Liu, Y.; Liu, J.; Sciaini, G. Robust fully controlled nanometer liquid layers for high resolution

liquid-cell electron microscopy. *Lab on a Chip* **2023**, *23*, Publisher: The Royal Society of Chemistry, 3217–3225.

(58) Parent, L. R.; Bakalis, E.; Proetto, M.; Li, Y.; Park, C.; Zerbetto, F.; Gianneschi, N. C. Tackling the Challenges of Dynamic Experiments Using Liquid-Cell Transmission Electron Microscopy. *Accounts of Chemical Research* **2018**, *51*, Publisher: American Chemical Society, 3–11.

(59) Zhu, G.; Jiang, Y.; Huang, W.; Zhang, H.; Lin, F.; Jin, C. Atomic resolution liquid-cell transmission electron microscopy investigations of the dynamics of nanoparticles in ultrathin liquids. *Chemical Communications* **2013**, *49*, Publisher: The Royal Society of Chemistry, 10944–10946.

(60) Serra-Maia, R.; Kumar, P.; Meng, A. C.; Foucher, A. C.; Kang, Y.; Karki, K.; Jariwala, D.; Stach, E. A. Nanoscale Chemical and Structural Analysis during In Situ Scanning/Transmission Electron Microscopy in Liquids. *ACS Nano* **2021**, *15*, Publisher: American Chemical Society, 10228–10240.

(61) Jin, B.; Wang, Y.; Jin, C.; De Yoreo, J. J.; Tang, R. Revealing Au13 as Elementary Clusters During the Early Formation of Au Nanocrystals. *The Journal of Physical Chemistry Letters* **2021**, *12*, 5938–5943.

(62) 14:00-17:00 ISO 14644-1:2015, ISO https://www.iso.org/standard/53394.html (accessed 04/16/2023).

(63) Dwyer, J. R.; Harb, M. Through a Window, Brightly: A Review of Selected Nanofabricated Thin-Film Platforms for Spectroscopy, Imaging, and Detection. *Applied Spectroscopy* **2017**, *71*, Publisher: SAGE Publications Ltd STM, 2051–2075.

(64) Vlassak, J. J.; Nix, W. D. A new bulge test technique for the determination of Young's modulus and Poisson's ratio of thin films. *Journal of Materials Research* **1992**, *7*, Publisher: Cambridge University Press, 3242–3249.

(65) Li, S.; Chang, Y.; Wang, Y.; Xu, Q.; Ge, B. A review of sample thickness effects on high-resolution transmission electron microscopy imaging. *Micron* **2020**, *130*, 102813.

(66) Mkrtchyan, M. M.; Liddle, J. A.; Novembre, A. E.; Waskiewicz, W. K.; Watson, G. P.; Harriott, L. R.; Muller, D. A. Electron scattering and transmission through SCALPEL masks. *Journal of Vacuum Science & Technology B: Microelectronics and Nanometer Structures Processing, Measurement, and Phenomena* **1998**, *16*, 3385–3391.

(67) Riley, M. E.; MacCallum, C. J.; Biggs, F. Theoretical electron-atom elastic scattering cross sections: Selected elements, 1 keV to 256 keV. *Atomic Data and Nuclear Data Tables* **1975**, *15*, 443–476.

(68) Shaw, N. Improving Biospecimen Imaging in Liquid Phase Electron Microscopy, MSc Thesis, University of Waterloo, 2023.

(69) Yesibolati, M. N.; Laganá, S.; Kadkhodazadeh, S.; Mikkelsen, E. K.; Sun, H.; Kasama, T.; Hansen, O.; Zaluzec, N. J.; Mølhave, K. Electron inelastic mean free path in water. *Nanoscale* **2020**, *12*, Publisher: The Royal Society of Chemistry, 20649–20657.

(70) Woehl, T. J.; Moser, T.; Evans, J. E.; Ross, F. M. Electron-beam-driven chemical processes during liquid phase transmission electron microscopy. *MRS Bulletin* **2020**, *45*, 746–753.

(71) Woehl, T. J.; Jungjohann, K. L.; Evans, J. E.; Arslan, I.; Ristenpart, W. D.; Browning, N. D. Experimental procedures to mitigate electron beam induced artifacts during in situ fluid imaging of nanomaterials. *Ultramicroscopy* **2013**, *127*, 53–63.

(72) Grogan, J. M.; Schneider, N. M.; Ross, F. M.; Bau, H. H. Bubble and Pattern Formation in Liquid Induced by an Electron Beam. *Nano Letters* **2014**, *14*, Publisher: American Chemical Society, 359–364.

(73) Schneider, N. M.; Norton, M. M.; Mendel, B. J.; Grogan, J. M.; Ross, F. M.; Bau, H. H. Electron–Water Interactions and Implications for Liquid Cell Electron Microscopy. *The Journal of Physical Chemistry C* **2014**, *118*, Publisher: American Chemical Society, 22373–22382.

(74) Egerton, R. F.; Li, P.; Malac, M. Radiation damage in the TEM and SEM. *Micron* **2004**, *35*, 399–409.

(75) McGilvery, C. M.; Goode, A. E.; Shaffer, M. S. P.; McComb, D. W. Contamination of holey/lacey carbon films in STEM. *Micron (Oxford, England: 1993)* **2012**, *43*, 450–455.

(76) Griffiths, A. J. V.; Walther, T. Quantification of carbon contamination under electron beam irradiation in a scanning transmission electron microscope and its suppression by plasma cleaning. *Journal of Physics: Conference Series* **2010**, *241*, 012017.

(77) Hansen, R. W. C.; Bissen, M.; Wallace, D.; Wolske, J.; Miller, T. Ultraviolet/ozone cleaning of carbon-contaminated optics. *Applied Optics* **1993**, *32*, Publisher: Optica Publishing Group, 4114–4116.

(78) Abellan, P.; Woehl, T. J.; Parent, L. R.; Browning, N. D.; Evans, J. E.; Arslan, I. Factors influencing quantitative liquid (scanning) transmission electron microscopy.

Chemical Communications **2014**, *50*, Publisher: The Royal Society of Chemistry, 4873–4880.

(79) Fisher, G.; Seacrist, M. R.; Standley, R. W. Silicon Crystal Growth and Wafer Technologies. *Proceedings of the IEEE* **2012**, *100*, Conference Name: Proceedings of the IEEE, 1454–1474.

(80) Kern, W.; Puotinen, D. A. Cleaning Solution Based on Hydrogen Peroxide for Use in Silicon Semiconductor Technology. *RCA Rev.* **1970**, *31*, 187–206.

(81) Kern, W. The Evolution of Silicon Wafer Cleaning Technology. *Journal of The Electrochemical Society* **1990**, *137*, Publisher: IOP Publishing, 1887.

(82) Gardeniers, J. G. E.; Tilmans, H. a. C.; Visser, C. C. G. LPCVD silicon-rich silicon nitride films for applications in micromechanics, studied with statistical experimental design*. *Journal of Vacuum Science & Technology A* **1996**, *14*, Publisher: American Vacuum Society, 2879–2892.

(83) Yang, C.; Pham, J. Characteristic Study of Silicon Nitride Films Deposited by LPCVD and PECVD. *Silicon* **2018**, *10*, 2561–2567.

(84) Korkin, A. A.; Cole, J. V.; Sengupta, D.; Adams, J. B. On the Mechanism of Silicon Nitride Chemical Vapor Deposition from Dichlorosilane and Ammonia. *Journal of The Electrochemical Society* **1999**, *146*, Publisher: IOP Publishing, 4203.

(85) Hu, S.-W.; Wang, Y.; Wang, X.-Y.; Chu, T.-W.; Liu, X.-Q. Gas-Phase Reactions between Silane and Ammonia: A Theoretical Study. *The Journal of Physical Chemistry A* **2003**, *107*, Publisher: American Chemical Society, 9189–9196.

(86) Atluri, V.; Herbots, N.; Dagel, D.; Bhagvat, S.; Whaley, S. Hydrogen passivation of Si(100) wafers as templates for low temperature (T $<$ 600°C) epitaxy. *Nuclear Instruments and Methods in Physics Research Section B: Beam Interactions with Materials and Atoms* **1996**, *118*, 144–150.

(87) Koseki, S.; Ishitani, A. Theoretical study on silicon-nitride film growth: Ab initio molecular orbital calculations. *Journal of Applied Physics* **1992**, *72*, Publisher: American Institute of Physics, 5808–5813.

(88) Ito, H. In *Chemical Amplification Resists for Microlithography. In: Microlithography · Molecular Imprinting.* Advances in Polymer Science; Springer: Berlin, Heidelberg, 2005, pp 37–245.

(89) Shipley Microposit® S1800® series photo resists data sheet.

(90) Shipley Microposit® MF®-321 developer data sheet.

(91) Franssila, S.; Sainiemi, L. In *Encyclopedia of Microfluidics and Nanofluidics*, Li, D., Ed.; Springer US: Boston, MA, 2008, pp 1772–1781.

(92) Labelle, C. B.; Donnelly, V. M.; Bogart, G. R.; Opila, R. L.; Kornblit, A. Investigation of fluorocarbon plasma deposition from c-C4F8 for use as passivation during deep silicon etching. *Journal of Vacuum Science & Technology A* **2004**, *22*, Publisher: American Vacuum Society, 2500–2507.

(93) Technical Data Sheet: Remover PG.

(94) Hartney, M. A.; Hess, D. W.; Soane, D. S. Oxygen plasma etching for resist stripping and multilayer lithography. *Journal of Vacuum Science & Technology B: Microelectronics Processing and Phenomena* **1989**, *7*, Publisher: American Institute of Physics, 1–13.

(95) Seidel, H.; Csepregi, L.; Heuberger, A.; Baumgärtel, H. Anisotropic Etching of Crystalline Silicon in Alkaline Solutions: I . Orientation Dependence and Behavior of Passivation Layers. *Journal of The Electrochemical Society* **1990**, *137*, Publisher: IOP Publishing, 3612.

(96) Han, J.; Yin, Y. J.; Han, D.; Dong, L. Improved PECVD SixNy film as a mask layer for deep wet etching of the silicon. *Materials Research Express* **2017**, *4*, Publisher: IOP Publishing, 096301.

(97) Stoneham, A. M.; Grovenor, C. R. M.; Cerezo, A. Oxidation and the structure of the silicon/oxide interface. *Philosophical Magazine B* **1987**, *55*, 201–210.

(98) Mueller, C.; Harb, M.; Dwyer, J. R.; Miller, R. J. D. Nanofluidic Cells with Controlled Pathlength and Liquid Flow for Rapid, High-Resolution In Situ Imaging with Electrons. *The Journal of Physical Chemistry Letters* **2013**, *4*, Publisher: American Chemical Society, 2339–2347.

(99) Zhang, Y.; Keller, D.; Rossell, M. D.; Erni, R. Formation of Au Nanoparticles in Liquid Cell Transmission Electron Microscopy: From a Systematic Study to Engineered Nanostructures. *Chemistry of Materials* **2017**, *29*, Publisher: American Chemical Society, 10518–10525.

(100) Li, X.; Mitsuishi, K.; Takeguchi, M. Fabrication of a liquid cell for in situ transmission electron microscopy. *Microscopy* **2021**, *70*, 327–332.

(101) Patterson, J. P.; Parent, L. R.; Cantlon, J.; Eickhoff, H.; Bared, G.; Evans, J. E.; Gianneschi, N. C. Picoliter Drop-On-Demand Dispensing for Multiplex Liquid Cell Transmission Electron Microscopy. *Microscopy and Microanalysis* **2016**, *22*, 507–514.

(102) Lemmon, E. W. In *"Vapor Pressure and Other Saturation Properties of Water", in CRC Handbook of Chemistry and Physics, 103rd Edition (Internet Version 2022)*; John R. Rumble, ed., CRC Press/Taylor & Francis, Boca Raton, FL.

(103) Yang, J.; Paul, O. Fracture properties of LPCVD silicon nitride thin films from the load–deflection of long membranes. *Sensors and Actuators A: Physical* **2002**, *97-98*, 520–526.

(104) Lott, T. S.; Sciaini, G.; Petruk, A. A. A miniature high-vacuum valve. *engrXiv* **2021**.

(105) Yen, B. K.; White, R. L.; Waltman, R. J.; Dai, Q.; Miller, D. C.; Kellock, A. J.; Marchon, B.; Kasai, P. H.; Toney, M. F.; York, B. R.; Deng, H.; Xiao, Q.-F.; Raman, V. Microstructure and properties of ultrathin amorphous silicon nitride protective coating. *Journal of Vacuum Science & Technology A* **2003**, *21*, 1895–1904.

(106) Reimer, L., *Image Formation in Low-voltage Scanning Electron Microscopy*; SPIE Press: 1993; 162 pp.

(107) Li, T.; Nowell, C. J.; Cipolla, D.; Rades, T.; Boyd, B. J. Direct Comparison of Standard Transmission Electron Microscopy and Cryogenic-TEM in Imaging Nanocrystals Inside Liposomes. *Molecular Pharmaceutics* **2019**, *16*, Publisher: American Chemical Society, 1775–1781.

(108) Liu, Y.; Liu, J. Cu2+-Directed Liposome Membrane Fusion, Positive-Stain Electron Microscopy, and Oxidation. *Langmuir* **2018**, *34*, Publisher: American Chemical Society, 7545–7553.

(109) Piffoux, M.; Ahmad, N.; Nelayah, J.; Wilhelm, C.; Silva, A.; Gazeau, F.; Alloyeau, D. Monitoring the dynamics of cell-derived extracellular vesicles at the nanoscale by liquid-cell transmission electron microscopy. *Nanoscale* **2018**, *10*, Publisher: The Royal Society of Chemistry, 1234–1244.

(110) Gnanasekaran, K.; Chang, H.; Smeets, P. J. M.; Korpanty, J.; Geiger, F. M.; Gianneschi, N. C. In Situ Ni2+ Stain for Liposome Imaging by Liquid-Cell Transmission Electron Microscopy. *Nano Letters* **2020**, *20*, Publisher: American Chemical Society, 4292–4297.

(111) Alam, S. B.; Yang, J.; Bustillo, K. C.; Ophus, C.; Ercius, P.; Zheng, H.; Chan, E. M. Hybrid nanocapsules for in situ TEM imaging of gas evolution reactions in confined liquids. *Nanoscale* **2020**, *12*, Publisher: The Royal Society of Chemistry, 18606–18615.

(112) Jabbari, V.; Sawczyk, M.; Amiri, A.; Král, P.; Shahbazian-Yassar, R. Unveiling growth and dynamics of liposomes by graphene liquid cell-transmission electron microscopy. *Nanoscale* **2023**, *15*, Publisher: The Royal Society of Chemistry, 5011–5022.

(113) François-Martin, C.; Rothman, J. E.; Pincet, F. Low energy cost for optimal speed and control of membrane fusion. *Proceedings of the National Academy of Sciences* **2017**, *114*, Publisher: Proceedings of the National Academy of Sciences, 1238–1241.

(114) Woehl, T. J.; Prozorov, T. The Mechanisms for Nanoparticle Surface Diffusion and Chain Self-Assembly Determined from Real-Time Nanoscale Kinetics in Liquid. *The Journal of Physical Chemistry C* **2015**, *119*, Publisher: American Chemical Society, 21261–21269.

(115) Qiao, L.; Pollard, N.; Senanayake, R. D.; Yang, Z.; Kim, M.; Ali, A. S.; Hoang, M. T.; Yao, N.; Han, Y.; Hernandez, R.; Clayborne, A. Z.; Jones, M. R. Atomically precise nanoclusters predominantly seed gold nanoparticle syntheses. *Nature Communications* **2023**, *14*, Number: 1 Publisher: Nature Publishing Group, 4408.

(116) Woehl, T.; Abellan, P. Defining the radiation chemistry during liquid cell electron microscopy to enable visualization of nanomaterial growth and degradation dynamics. *Journal of Microscopy* **2017**, *265*, 135–147.

(117) Sciaini, G.; Miller, R. J. D. Femtosecond electron diffraction: heralding the era of atomically resolved dynamics. *Reports on Progress in Physics* **2011**, *74*, 096101.

(118) Sciaini, G. Recent Advances in Ultrafast Structural Techniques. *Applied Sciences* **2019**, *9*, Number: 7 Publisher: Multidisciplinary Digital Publishing Institute, 1427.

(119) Malac, M.; Hettler, S.; Hayashida, M.; Kano, E.; Egerton, R. F.; Beleggia, M. Phase plates in the transmission electron microscope: operating principles and applications. *Microscopy* **2021**, *70*, 75–115.

APPENDICES

Appendix A

Python Code for Data Analysis

A.1 Conversion of image stacks to video

A set of scripts to convert an image stack to video and provide text labelling.

These scripts were developed in the following environment:

Python 3.9.7

opencv-python 4.5.5.62

tk 8.6.11

pillow 7.2.0

matplotlib 3.4.3

numpy 1.20.3

```
"""
Created on Tue Jan 31 20:16:15 2023

```

```
@author: tyler

A short script to label an image stack before video conversion

MIT License

Copyright (c) 2023 Tyler Lott

Permission is hereby granted, free of charge, to any person obtaining a copy
of this software and associated documentation files (the "Software"), to deal
in the Software without restriction, including without limitation the rights
to use, copy, modify, merge, publish, distribute, sublicense, and/or sell
copies of the Software, and to permit persons to whom the Software is
furnished to do so, subject to the following conditions:
The above copyright notice and this permission notice shall be included in all
copies or substantial portions of the Software.
THE SOFTWARE IS PROVIDED "AS IS", WITHOUT WARRANTY OF ANY KIND, EXPRESS OR
IMPLIED, INCLUDING BUT NOT LIMITED TO THE WARRANTIES OF MERCHANTABILITY,
FITNESS FOR A PARTICULAR PURPOSE AND NONINFRINGEMENT. IN NO EVENT SHALL THE
AUTHORS OR COPYRIGHT HOLDERS BE LIABLE FOR ANY CLAIM, DAMAGES OR OTHER
LIABILITY, WHETHER IN AN ACTION OF CONTRACT, TORT OR OTHERWISE, ARISING FROM,
OUT OF OR IN CONNECTION WITH THE SOFTWARE OR THE USE OR OTHER DEALINGS IN THE
SOFTWARE.
"""

import os
import tkinter as tk
from tkinter import filedialog
from PIL import Image
from PIL import ImageDraw
from PIL import ImageFont
import matplotlib as mpl
import numpy as np
import copy

root = tk.Tk()
root.withdraw()

image_folder = filedialog.askdirectory()

```

```
images = [img for img in os.listdir(image_folder) if img.endswith(".tif")]
int_images= []
num = ["0","1","2","3","4","5","6","7","8","9"]
new_lst = []

test_lst = []
file_name_lst = []
count = 0
while count < len(images):
    for i in images[count]:
        if i in num:
            new_lst.append(i)
        elif count == 0:
            test_lst.append(i)
    val = ''.join(new_lst)
    if len(val) == 1:
        int_images.append("%01d" % int(val))
    elif len(val) == 2:
        int_images.append("%02d" % int(val))
    elif len(val) == 3:
        int_images.append("%03d" % int(val))
    elif len(val) == 4:
        int_images.append("%04d" % int(val))
    elif len(val) == 5:
        int_images.append("%05d" % int(val))
    elif len(val) == 6:
        int_images.append("%06d" % int(val))
    new_lst = []
    count += 1

int_images.sort()

final_lst = []
count = 0

while count < len(int_images):
    text_lst = copy.deepcopy(test_lst)
    text_lst.insert(test_lst.index('.'),int_images[count])
    count += 1
    final_lst.append(text_lst)
```

```
84
85
86  final_lst_adjusted = []
87  count = 0
88
89
90  while count < len(final_lst):
91      filename_adjusted = ''.join(str(final_lst[count]))
92      filename_adjusted = filename_adjusted.replace("'","")
93      filename_adjusted = filename_adjusted.replace("[","")
94      filename_adjusted = filename_adjusted.replace("]","")
95      filename_adjusted = filename_adjusted.replace(",","")
96      filename_adjusted = filename_adjusted.replace(" ", "")
97      final_lst_adjusted.append(filename_adjusted)
98      count += 1
99
100 path_to_tif = image_folder.count("/") # Counting the number of sub-folders
        within the root folder
101 def remove_last(s):
102     num_removed = 0
103     while s.count("/") == path_to_tif:
104         try:
105             s = s[0:-1]
106             if s.count('/') == path_to_tif:
107                 num_removed += 1
108                 continue
109             else:
110                 return [s,num_removed]
111
112         except ValueError:
113             return ""
114
115 initial_file_path = remove_last(image_folder)[0] # Finding the root file path
116 image_ID = image_folder[len(image_folder)-remove_last(image_folder)[1]:-4] #
        Finding the name of the file ("linescan ID")
117 print(initial_file_path)
118 main_path = str(initial_file_path) + "/" + str(image_ID)
119
120 # First we check to see whether the specified path exists or not
121
```

```
122 isExist = os.path.exists(main_path)
123
124 if not isExist:
125   # We create a new directory because it does not exist
126   os.makedirs(main_path)
127
128 path = str(main_path) + "/" + str(image_ID) + str("Testing")
129
130 system_fonts = mpl.font_manager.findSystemFonts(fontpaths=None, fontext='ttf')
      ### List of system fonts
131
132 value_array = [0]
133 frame_time = 0.8402035
134 count = 0
135 time = 0
136
137 while count < len(images):
138     time += frame_time
139     value_array.append(round(time)) # Rounding to the nearest integer
140     count += 1
141 count = 0
142
143 with open(str(path), "w") as output:
144     for image in final_lst_adjusted:
145         # Call draw Method to add 2D graphics in an image
146         img = Image.open(str(image_folder)+ "/" + str(image))
147         I1 = ImageDraw.Draw(img)
148
149         # Custom font style and font size
150         myFont =
              ImageFont.truetype('/System/Library/Fonts/Supplemental/Arial.ttf',
              size=60)
151         myFont2 =
              ImageFont.truetype('/System/Library/Fonts/Supplemental/Arial.ttf',
              size=40)
152
153         # Add Text to an image
154         I1.text((10, 10), str(str(value_array[count])+str(" seconds")), fill =
              "#FFFFFF", font=myFont)
155         # Add Text to an image
```

```
        I1.text((800, 35), "10x speed", fill = "#FFFFFF", font=myFont2)
        I1.text((250, 900), "Unstained Liposomes", fill = "#FFFFFF", font=myFont)
        # Display edited image
        if count == 0:
            img.show()

        # Save the edited image
        img.save(path + str(count) + ".tif")
        count += 1
```

```
"""
Created on Tue Jan 31 20:07:11 2023

@author: tyler

A short script to convert an image stack to video

MIT License

Copyright (c) 2023 Tyler Lott

Permission is hereby granted, free of charge, to any person obtaining a copy
of this software and associated documentation files (the "Software"), to deal
in the Software without restriction, including without limitation the rights
to use, copy, modify, merge, publish, distribute, sublicense, and/or sell
copies of the Software, and to permit persons to whom the Software is
furnished to do so, subject to the following conditions:
The above copyright notice and this permission notice shall be included in all
copies or substantial portions of the Software.
THE SOFTWARE IS PROVIDED "AS IS", WITHOUT WARRANTY OF ANY KIND, EXPRESS OR
IMPLIED, INCLUDING BUT NOT LIMITED TO THE WARRANTIES OF MERCHANTABILITY,
FITNESS FOR A PARTICULAR PURPOSE AND NONINFRINGEMENT. IN NO EVENT SHALL THE
AUTHORS OR COPYRIGHT HOLDERS BE LIABLE FOR ANY CLAIM, DAMAGES OR OTHER
LIABILITY, WHETHER IN AN ACTION OF CONTRACT, TORT OR OTHERWISE, ARISING FROM,
OUT OF OR IN CONNECTION WITH THE SOFTWARE OR THE USE OR OTHER DEALINGS IN THE
SOFTWARE.
"""
import cv2
import os
```

```
import tkinter as tk
from tkinter import filedialog
import copy

root = tk.Tk()
root.withdraw()

choose_dir = filedialog.askdirectory()

image_folder = choose_dir

video_name = 'test.avi'

images = [img for img in os.listdir(image_folder) if img.endswith(".tif")]
int_images= []
num = ["0","1","2","3","4","5","6","7","8","9"]
new_lst = []

test_lst = []
file_name_lst = []
count = 0
while count < len(images):
    for i in images[count]:
        if i in num:
            new_lst.append(i)
        elif count == 0:
            test_lst.append(i)
    val = ''.join(new_lst)
    int_images.append(int(val))
    new_lst = []
    count += 1

int_images.sort()

final_lst = []
count = 0

while count < len(int_images):
    text_lst = copy.deepcopy(test_lst)
    text_lst.insert(test_lst.index('.'),int_images[count])
```

```
    count += 1
    final_lst.append(text_lst)


final_lst_adjusted = []
count = 0


while count < len(final_lst):
    filename_adjusted = ''.join(str(final_lst[count]))
    filename_adjusted = filename_adjusted.replace("'","")
    filename_adjusted = filename_adjusted.replace("[","")
    filename_adjusted = filename_adjusted.replace("]","")
    filename_adjusted = filename_adjusted.replace(",","")
    filename_adjusted = filename_adjusted.replace(" ", "")
    final_lst_adjusted.append(filename_adjusted)
    count += 1

frame = cv2.imread(os.path.join(image_folder, images[0]))
height, width, layers = frame.shape

fps = (10*1.1901878532998256)

# Window name in which image is displayed
window_name = 'Image'

# Font
font = cv2.FONT_HERSHEY_SIMPLEX

frame_count = 0
time = float(frame_count)/fps
cv2.putText(frame, str(time), (10,500), font, 4, (255,255,255), 2, cv2.LINE_AA)
video = cv2.VideoWriter(video_name, 0, fps, (width,height))

frame_count = 0
for image in final_lst_adjusted:
    video.write(cv2.imread(os.path.join(image_folder, image)))

cv2.destroyAllWindows()
video.release()
```

A.2 EMD file type conversion

A set of scripts to convert .emd files into image files.

These scripts were developed in the following environment:

Python 3.9.7

hyperspy 1.6.5

tk 8.6.11

pillow 7.2.0

numpy 1.20.3

matplotlib 3.4.3

h5py 3.6.0

```
"""
Created on Tue Jan 31 19:40:56 2023

@author: tyler

A script to convert single .emd files into image files.

MIT License

Copyright (c) 2023 Tyler Lott

Permission is hereby granted, free of charge, to any person obtaining a copy
of this software and associated documentation files (the "Software"), to deal
in the Software without restriction, including without limitation the rights
to use, copy, modify, merge, publish, distribute, sublicense, and/or sell
copies of the Software, and to permit persons to whom the Software is
furnished to do so, subject to the following conditions:
The above copyright notice and this permission notice shall be included in all
copies or substantial portions of the Software.
THE SOFTWARE IS PROVIDED "AS IS", WITHOUT WARRANTY OF ANY KIND, EXPRESS OR
IMPLIED, INCLUDING BUT NOT LIMITED TO THE WARRANTIES OF MERCHANTABILITY,
FITNESS FOR A PARTICULAR PURPOSE AND NONINFRINGEMENT. IN NO EVENT SHALL THE
AUTHORS OR COPYRIGHT HOLDERS BE LIABLE FOR ANY CLAIM, DAMAGES OR OTHER
LIABILITY, WHETHER IN AN ACTION OF CONTRACT, TORT OR OTHERWISE, ARISING FROM,
```

```
25 OUT OF OR IN CONNECTION WITH THE SOFTWARE OR THE USE OR OTHER DEALINGS IN THE
26 SOFTWARE.
27 """
28
29 import os
30 import hyperspy.api as hs
31 import tkinter as tk
32 from tkinter import filedialog
33 from PIL import Image
34 import numpy as np
35 import h5py
36 import json
37
38 root = tk.Tk()
39 root.withdraw()
40
41 file = filedialog.askopenfilename()
42 print(file)
43 file_path2 = os.rename(file, file[0:-4].replace(".","_")+".emd") # Auto-renaming
       of the folder to prevent mis-reading later in the file
44 file_path2 = file[0:-4].replace(".","_")+".emd"
45 file_path = open(os.path.expanduser(str(file_path2)))
46 s = hs.load(file_path.name, lazy = True, stack = True) # lazy = True, A Lazy
       Signal instance that delays computation until explicitly saved (assuming
       storing the full result of computation in memory is not feasible)
47 print("Hyperspy API load complete.")
48 num_imgs = len(s)
49
50 ### Save all of the metadata to a text file for a single image ###
51 def save_pet(pet):
52     filename = "Image_MD.txt"
53     with open(filename, 'w') as f:
54         f.write(json.dumps(pet))
55
56 ############################### Metadata storage
       ###################################
57
58 f = h5py.File(file, 'r')
59 class navigate:
60
```

```
61      @staticmethod
62      def getGroupsNames(group):
63          items = []
64          for item in group:
65              if group.get(item, getclass=True) == h5py._hl.group.Group:
66                  items.append(group.get(item).name)
67
68      @staticmethod
69      def getGroup(group, item):
70          if group.get(item, getclass=True) == h5py._hl.group.Group:
71              return group.get(item)
72
73      @staticmethod
74      def getSubGroup(group, path):
75          return group[path]
76
77      @staticmethod
78      def getDirectoryMap(group):
79          for item in group:
80              # check if group
81              if group.get(item, getclass=True) == h5py._hl.group.Group:
82                  item = group.get(item)
83                  # process subgroups
84                  if type(item) is h5py._hl.group.Group:
85                      navigate.getDirectoryMap(item)
86
87      @staticmethod
88      def getMemberName(group, path):
89          members = list(group[path].keys())
90          if len(members) == 1:
91              return str(members[0])
92          else:
93              return members
94
95  class decode:
96
97      @staticmethod
98      def convertASCII(ascii_meta):
99          metadata_text = ''.join(chr(i) for i in ascii_meta)
100         return metadata_text.replace("\0", '')
```

```
101
102 # Get metadata.
103 metalocation = navigate.getMemberName(f, '/Data/Image/')
104 #options = navigate.getMemberName(f, '/Data/Image/' + metalocation) # shows name
    for metadata subdir.
105
106 if num_imgs > 1:
107     print(str(num_imgs)+" images")
108 else:
109     print(str(num_imgs)+" image")
110 s_metadata = []
111
112 ### Saving selected metadata parameters to txt ###
113 if num_imgs > 1:
114     img_num = 0
115     while img_num < len(s):
116         ascii_meta = f['/Data/Image/' + str(metalocation) +
              '/Metadata'][:][:,img_num] # frame
117         jsonmeta = decode.convertASCII(ascii_meta)
118         result = json.loads(jsonmeta)
119         pixel_size_width = float(result['BinaryResult']['PixelSize']['width'])
120         pixel_size_height = float(result['BinaryResult']['PixelSize']['height'])
121         frame_time = float(result['Scan']['FrameTime'])
122         magnification = float(result['Optics']['NominalMagnification'])
123         screen_current = float(result['Optics']['LastMeasuredScreenCurrent'])
124         image_metadata = {"Pixel size height (m):": pixel_size_height,"Pixel size
              width (m):": pixel_size_width, "Frame time (s):": frame_time,
              "Magnification:": magnification, "Screen current (A):":
              screen_current}
125         s_metadata.append(image_metadata)
126         img_num += 1
127
128 else:
129     img_num = 0
130     ascii_meta = f['/Data/Image/' + str(metalocation) +
          '/Metadata'][:][:,img_num] # frame
131     jsonmeta = decode.convertASCII(ascii_meta)
132     result = json.loads(jsonmeta)
133     pixel_size_width = float(result['BinaryResult']['PixelSize']['width'])
134     pixel_size_height = float(result['BinaryResult']['PixelSize']['height'])
```

```
135     frame_time = float(result['Scan']['FrameTime'])
136     screen_current = float(result['Optics']['LastMeasuredScreenCurrent'])
137     #magnification = float(result['Optics']['NominalMagnification'])
138     #frame_time = float(s.original_metadata.Scan.FrameTime)
139     image_metadata = {"Pixel size height (m)": pixel_size_height,"Pixel size
            width (m)": pixel_size_width}#, "Magnification": magnification}#, "Frame
            time (s)": frame_time}
140     s_metadata.append(image_metadata)
141 
142 img_lst = []
143 imarray = np.array(s)
144 img_num = 0
145 
146 ### Placeholder boolean to choose PIL, OpenCV could also be implemented here
        (not included)
147 
148 if num_imgs > 1:
149     while img_num < num_imgs: # Converting the image arrays in Hyperspy format
            to numpy array, then placing the array in a list
150         img_lst.append(imarray[img_num])
151         img_num += 1
152 
153     img_norm_lst = []
154     img_num = 0
155 
156     ### File saving
157     save_input = input("Would you like to save? (Y/N)? ")
158     if save_input == "Y" or save_input == "Yes" or save_input == "yes" or
            save_input == "y":
159         save_path = filedialog.asksaveasfilename(initialfile = "frame")
160         file_ext = save_path[save_path.rfind("."):] # rfind finds the last
                occurrence of a substring within a string
161         if save_path[-1] == file_ext: # Defaults to save as a tif if the user
                does not specify the file extension, also possible through Tkinter
162             save_path = str(save_path) + ".tif"
163             file_ext = ".tif"
164         file_dir = save_path[0:save_path.rfind(".")]
165         with open(str(file_dir)+"_s_metadata.txt", "w") as output:
166             MD_count = 1
167             for i in s_metadata:
```

```
                output.write("["+str(MD_count)+"]"+str(i)+"\n")
                MD_count += 1
        print("END OF PROGRAM")
        root.destroy()
    else:
        print("END OF PROGRAM")

else:  # Dealing with single image EMD files
    #imarray *= 255/imarray.max() # Commented out to remove 8-bit conversion
        which appeared to create artifacts
    PIL_image = Image.fromarray(imarray) # Changed
        Image.fromarray(np.uint8(imarray)) to Image.fromarray(imarray) to
        maintain the 16 bit file size which reduces artifacts

### File saving
    save_input = input("Would you like to save? (Y/N)? ")
    if save_input == "Y" or save_input == "Yes" or save_input == "yes" or
        save_input == "y":
        save_path = filedialog.asksaveasfilename(initialfile = "frame")
        file_ext = save_path[save_path.rfind("."):]
        if save_path[-1] == file_ext: # Defaults to save as a tif if the user
            does not specify the file extension
            save_path = str(save_path) + ".tif"
            file_ext = ".tif"
        file_dir = save_path[0:save_path.rfind(".")]
        with open(str(file_dir)+"_s_metadata.txt", "w") as output:
            output.write(str(s_metadata)+"\n")
        PIL_image.save((save_path))
        root.destroy()
    else:
        print("END OF PROGRAM")
        root.destroy()

save_pet(result)
```

```
"""
Created on Tue Jan 31 19:47:17 2023

@author: tyler
```

```
5
6  A script to batch convert .emd files into image files.
7
8  MIT License
9
10 Copyright (c) 2023 Tyler Lott
11
12 Permission is hereby granted, free of charge, to any person obtaining a copy
13 of this software and associated documentation files (the "Software"), to deal
14 in the Software without restriction, including without limitation the rights
15 to use, copy, modify, merge, publish, distribute, sublicense, and/or sell
16 copies of the Software, and to permit persons to whom the Software is
17 furnished to do so, subject to the following conditions:
18 The above copyright notice and this permission notice shall be included in all
19 copies or substantial portions of the Software.
20 THE SOFTWARE IS PROVIDED "AS IS", WITHOUT WARRANTY OF ANY KIND, EXPRESS OR
21 IMPLIED, INCLUDING BUT NOT LIMITED TO THE WARRANTIES OF MERCHANTABILITY,
22 FITNESS FOR A PARTICULAR PURPOSE AND NONINFRINGEMENT. IN NO EVENT SHALL THE
23 AUTHORS OR COPYRIGHT HOLDERS BE LIABLE FOR ANY CLAIM, DAMAGES OR OTHER
24 LIABILITY, WHETHER IN AN ACTION OF CONTRACT, TORT OR OTHERWISE, ARISING FROM,
25 OUT OF OR IN CONNECTION WITH THE SOFTWARE OR THE USE OR OTHER DEALINGS IN THE
26 SOFTWARE.
27 """
28
29 import os
30 import hyperspy.api as hs
31 import tkinter as tk
32 from tkinter import filedialog
33 from PIL import Image
34 import numpy as np
35 from pathlib import Path
36 import h5py
37 import json
38
39 root = tk.Tk()
40 root.withdraw()
41
42 ### Iterate through all of the emd files within a directory
43 choose_dir = filedialog.askdirectory()
44 mydir = Path(str(choose_dir))
```

```
for file in mydir.glob('*.emd'):
    if file.name[0:2] == "._": # If the h5py files are improperly downloaded
        they will leave a corrupted "ghost" file with "._" at the beginning of
        the filename, this for loop acts as a filter for this miswrite
        continue
    else:
        print(file.name)

        s = hs.load(str(file), lazy = True) # lazy = True, A Lazy Signal instance
            that delays computation until explicitly saved (assuming storing the
            full result of computation in memory is not feasible)
        s_name = file.name
        print("Hyperspy API load complete.")
        num_imgs = len(s)

        ############################## Metadata storage
            ###################################

        f = h5py.File(str(file), 'r')

        class navigate:

            @staticmethod
            def getGroupsNames(group):
                items = []
                for item in group:
                    if group.get(item, getclass=True) == h5py._hl.group.Group:
                        items.append(group.get(item).name)
                print(items)

            @staticmethod
            def getGroup(group, item):
                if group.get(item, getclass=True) == h5py._hl.group.Group:
                    return group.get(item)

            @staticmethod
            def getSubGroup(group, path):
                return group[path]

            @staticmethod
```

```
80              def getDirectoryMap(group):
81                  for item in group:
82                      # check if group
83                      if group.get(item, getclass=True) == h5py._hl.group.Group:
84                          item = group.get(item)
85                          # process subgroups
86                          if type(item) is h5py._hl.group.Group:
87                              navigate.getDirectoryMap(item)
88              @staticmethod
89              def getMemberName(group, path):
90                  members = list(group[path].keys())
91                  if len(members) == 1:
92                      return str(members[0])
93                  else:
94                      return members
95
96          class decode:
97
98              @staticmethod
99              def convertASCII(ascii_meta):
100                 metadata_text = ''.join(chr(i) for i in ascii_meta)
101                 return metadata_text.replace("\0", '')
102
103         # Get metadata.
104         metalocation = navigate.getMemberName(f, '/Data/Image/')
105         #options = navigate.getMemberName(f, '/Data/Image/' + metalocation) #
                shows name for metadata subdir.
106
107         if num_imgs > 1:
108             print(str(num_imgs)+" images")
109         else:
110             print(str(num_imgs)+" image")
111         s_metadata = []
112
113         if num_imgs > 1:
114             img_num = 0
115             while img_num < len(s):
116                 ascii_meta = f['/Data/Image/' + str(metalocation) +
                        '/Metadata'][:][:,img_num] # frame
117                 jsonmeta = decode.convertASCII(ascii_meta)
```

```
            result = json.loads(jsonmeta)
            pixel_size_width =
                float(result['BinaryResult']['PixelSize']['width'])
            pixel_size_height =
                float(result['BinaryResult']['PixelSize']['height'])
            frame_time = float(result['Scan']['FrameTime'])
            screen_current =
                float(result['Optics']['LastMeasuredScreenCurrent'])
            image_metadata = {"Pixel size height (m)":
                pixel_size_height,"Pixel size width (m)": pixel_size_width,
                "Frame time (s)": frame_time}
            s_metadata.append(image_metadata)
            img_num += 1

    else:
        img_num = 0
        ascii_meta = f['/Data/Image/' + str(metalocation) +
            '/Metadata'][:][:,img_num] # frame
        jsonmeta = decode.convertASCII(ascii_meta)
        result = json.loads(jsonmeta)
        pixel_size_width = float(result['BinaryResult']['PixelSize']['width'])
        pixel_size_height =
            float(result['BinaryResult']['PixelSize']['height'])
        #frame_time = float(s.original_metadata.Scan.FrameTime)
        image_metadata = {"Pixel size height (m)": pixel_size_height,"Pixel
            size width (m)": pixel_size_width}#, "Frame time (s)": frame_time}
        s_metadata.append(image_metadata)

    img_lst = []
    imarray = np.array(s)
    img_num = 0

    if num_imgs > 1:
        while img_num < num_imgs: # Converting the image arrays in Hyperspy
            format to numpy array, then placing the array in a list
            img_lst.append(imarray[img_num])
            img_num += 1


    ### File saving
```

```
149             save_input = "Y" # Defaulted to yes
150             if save_input == "Y" or save_input == "Yes" or save_input == "yes" or
                    save_input == "y":
151                 initial_file_name =
                        s_name[0:len(s_name)-len(s_name[s_name.find("."):])]
152                 initial_file_name = initial_file_name.replace(" ", "_")
153                 path = str(mydir) + "/" + str(initial_file_name)
154                 print(path)
155                 # Check whether the specified path exists or not
156                 isExist = os.path.exists(path)
157 
158                 if not isExist:
159                   # Create a new directory because it does not exist
160                   os.makedirs(path)
161                   print("The new directory is created!")
162                 path = str(path)+"/"+str(initial_file_name)
163                 with open(str(path)+"_s_metadata.txt", "w") as output:
164                     MD_count = 1
165                     for i in s_metadata:
166                         output.write("["+str(MD_count)+"]"+str(i)+"\n")
167                         MD_count += 1
168                 print("Analyzing image stack...")
169                 #root.destroy()
170             else:
171                 print("END OF PROGRAM")
172                 #root.destroy()
173                 img_num = 0
174 
175             file_ext = ".tif"
176             file_dir = path
177             for i in img_lst:
178                    img_num += 1
179                    imarray = i
180                    PIL_image = Image.fromarray(imarray)
181                    PIL_image.save((f"{file_dir}{img_num}{file_ext}"))
182 
183         else:  # Dealing with single image EMD files
184             PIL_image = Image.fromarray(imarray)
185 
186         ### File saving
```

```
            save_input = "Y"
            if save_input == "Y" or save_input == "Yes" or save_input == "yes" or
                save_input == "y":
                initial_file_name =
                    s_name[0:len(s_name)-len(s_name[s_name.find("."):])]
                initial_file_name = initial_file_name.replace(" ", "_")
                path = str(mydir) + "/" + str(initial_file_name)
                print(path)
                # Check whether the specified path exists or not
                isExist = os.path.exists(path)

                if not isExist:
                  # Create a new directory because it does not exist
                  os.makedirs(path)
                  print("The new directory is created!")
                path = str(path)+"/"+str(initial_file_name)
                with open(str(path)+"_s_metadata.txt", "w") as output:
                    for i in s_metadata:
                        output.write(str(s_metadata)+"\n")
                PIL_image.save((str(path) + ".tif"))
                print("END OF PROGRAM")
                #root.destroy()
            else:
                print("END OF PROGRAM")
                #root.destroy()
            img_num = 0

print("END OF PROGRAM")
```

A.3 EELS Analysis

A short script to extract and analyze EELS linescan data from .dm4 files. This script can be utilized to determine the thickness of materials from EELS linescan data. For more information regarding the theory of EELS, please see the following resources:

Egerton, R. F. Electron Energy-Loss Spectroscopy in the Electron Microscope. (Springer US, 2011). doi:10.1007/978-1-4419-9583-4

Malis, T., Cheng, S. C. Egerton, R. F. EELS log-ratio technique for specimen-thickness measurement in the TEM. J. Electron Microsc. Tech. 8, 193–200 (1988).

doi:10.1002/jemt.1060080206

This script was developed in the following environment:

Python 3.9.7

hyperspy 1.6.5

tk 8.6.11

numpy 1.20.3

matplotlib 3.4.3

scipy 1.8.0

lmfit 1.0.3

```
"""
Created on Tue Jan 31 19:31:30 2023

@author: tyler

A short script to extract and analyze EELS linescan data from .dm4 files

MIT License

Copyright (c) 2023 Tyler Lott

Permission is hereby granted, free of charge, to any person obtaining a copy
of this software and associated documentation files (the "Software"), to deal
in the Software without restriction, including without limitation the rights
to use, copy, modify, merge, publish, distribute, sublicense, and/or sell
copies of the Software, and to permit persons to whom the Software is
furnished to do so, subject to the following conditions:

The above copyright notice and this permission notice shall be included in all
copies or substantial portions of the Software.

THE SOFTWARE IS PROVIDED "AS IS", WITHOUT WARRANTY OF ANY KIND, EXPRESS OR
IMPLIED, INCLUDING BUT NOT LIMITED TO THE WARRANTIES OF MERCHANTABILITY,
FITNESS FOR A PARTICULAR PURPOSE AND NONINFRINGEMENT. IN NO EVENT SHALL THE
```

```
AUTHORS OR COPYRIGHT HOLDERS BE LIABLE FOR ANY CLAIM, DAMAGES OR OTHER
LIABILITY, WHETHER IN AN ACTION OF CONTRACT, TORT OR OTHERWISE, ARISING FROM,
OUT OF OR IN CONNECTION WITH THE SOFTWARE OR THE USE OR OTHER DEALINGS IN THE
SOFTWARE.
"""

import os
import hyperspy.api as hs
import tkinter as tk
from tkinter import filedialog
import numpy as np
import matplotlib.pyplot as plt
from scipy.integrate import simps
from lmfit.models import Model

### Using Tkinter to open file dialogs for file selection by the user
root = tk.Tk()
root.withdraw()

##### MICROSCOPE SELECTION #####
microscope_select = 2 # A variable which can be changed depending on which
    microscope was used to acquire the data. Input the desired value
    corresponding to the microscopes listed below.
if microscope_select == 1:
    print("TALOS 200X Selected")
    set_acceleration_voltage = 200
    set_collection_angle = 23
    t_over_lamda = 0.400036406988378 # Talos two linescans (within the same
        cell): 0.400036406988378
elif microscope_select == 2:
    print("Titan 80-300HB Selected")
    set_acceleration_voltage = 300
    set_collection_angle = 55
    t_over_lamda = 0.39191442410 # Talos two linescans (within the same cell)::
        0.39191442410
################################

##### DATA STORAGE ARRAYS #####

### x and y ###
```

```
x_data_array = []
y_data_array = []

### Arrays for the LMFIT best fit data ###
thickness_array = []
intensity_ratio_array = []

if microscope_select == 2:
    silicon_nitride_line_scan = input("Is the linescan for an empty nanofluidic cell (no liquid)? ") # Prompt the user to determine if the linescan is for an empty or a hydrated nanofluidic cell assembly
    if silicon_nitride_line_scan == "Y" or silicon_nitride_line_scan == "Yes" or silicon_nitride_line_scan == "yes" or silicon_nitride_line_scan == "y":
        silicon_nitride_line_scan = True # A boolean which establishes that the linescan was performed on an empty nanofluidic cell assembly
    else:
        silicon_nitride_line_scan = False # A boolean which establishes that the linescan was performed on a hydrated nanofluidic cell assembly
    print("Please open the file for the linescan")
    file_path = filedialog.askopenfilename() # The user will select the .dm4 file which holds the EELS data
    print(file_path)
    ##### This variable and the subsequent function allow for the creation of folders within the path of the data files #####
    path_to_dm4 = file_path.count("/") # Counting the number of sub-folders within the root folder
    def remove_last(s):
        num_removed = 0
        while s.count("/") == path_to_dm4:
            try:
                s = s[0:-1]
                if s.count('/') == path_to_dm4:
                    num_removed += 1
                    continue
                else:
                    return [s,num_removed]

            except ValueError:
                return ""
```

```
92      initial_file_path = remove_last(file_path)[0] # Finding the root file path
93      linescan_ID = file_path[len(file_path)-remove_last(file_path)[1]:-4] #
            Finding the name of the file ("linescan ID")
94      print(initial_file_path)
95      s = hs.load(file_path) # Using the Hyperspy API to open the .dm4 file
96      s_array = np.array(s) # Converting the filetype from H5py to a numpy array
            for easy manipulation
97      main_path = str(initial_file_path) + "/" + str(linescan_ID) # Creating a
            root folder for the linescan
98      # Check whether the specified path exists or not
99      isExist = os.path.exists(main_path)
100
101     if not isExist:
102       # Create a new directory because it does not exist
103       os.makedirs(main_path)
104
105     path = str(main_path) + "/" + str(linescan_ID) +
            str("_EELS_linescan_thickness")
106
107     isExist = os.path.exists(path)
108
109     if not isExist:
110       # Create a new directory because it does not exist
111       os.makedirs(path)
112
113     ##### ANALYSIS OF THE SELECTED .dm4 FILE #####
114     count = 0 # First we establish a counter as a means to select where we
            would like to begin data analysis within the linescan
115     with open(str(path)+"/"+"EELS_thickness_calculation_results.txt", "w") as
            output: # Within the text file that we have created in the newly
            established path, we will conduct data analysis and save the results
116         while count < len(s_array): # While the counter is less then the length
                of the collected data file, we will perform data analysis, change
                this parameter to select individual spectra or groups of spectra
                from a larger dataset
117             output.write(str("#####"+str(s_array[count])+ "#####" + "\n")) # A
                    label to easily search the text file which will be generated
118             data_y = s_array[count] # The intensity of the EELS linescan, this
                    will change as we iterate through the while loop with the counter
119             data_x = np.arange(0, len(data_y), 1) # The x-axis is created as a
```

```
    counter of the step within the linescan
max_y = np.max(data_y) # Finding the maximum intensity within the
    spectrum
max_y_index = np.where(data_y == max_y)[0][0] # Finding the index in
    the numpy array where the spectrum is at an intensity maximum
# if max_y_index < 100: # This conditional is used if outliers exist
    at the beginning of the linescan, eg. a false maximum in the EELS
    spectrum
#     max_y = np.max(data_y[100:])
#     max_y_index = np.where(data_y == max_y)[0][0]
half_max = max_y/2
data_x_corrected = []
data_x_counter = 0
while data_x_counter < max_y_index:
    data_x_corrected.append(-max_y_index+data_x_counter)
    data_x_counter += 1
data_x_corrected.append(0)
data_x_counter = 1
while len(data_x_corrected) < len(data_y):
    data_x_corrected.append(data_x_counter)
    data_x_counter += 1

dispersion_value = \
    s.original_metadata.ImageList.TagGroup0.\
        ImageTags.EELS_Spectrometer.Dispersion_eVch # Channel is
            apparently capitalized for the Talos software but not for
            the Titan software
data_x_corrected = \
    np.linspace(data_x_corrected[0]*dispersion_value,\
                (len(data_x_corrected)-max_y_index)\
                    *dispersion_value-dispersion_value,\
                        num=len(data_x_corrected))
xdata = np.array(data_x_corrected)
ydata = data_y

### Since the half-maximum changes quite substantially from each
    measurement, here we roughly define the half-maximum value on
    either side of the ZLP, which gives a pseudo FWHM for the
    construction of the Gaussian function
def find_nearest(array, value):
```

```
150             array = np.asarray(array)
151             idx = (np.abs(array - value)).argmin()
152             return array[idx]
153
154         approximate_half_max_left_point =
                (find_nearest(ydata[max_y_index-100:max_y_index+1],
                value=half_max)) # Here we confine the selection of the nearest
                left data point (in relation to the global maximum) to within 100
                data points
155         approximate_half_max_right_point =
                (find_nearest(ydata[max_y_index:max_y_index+100],
                value=half_max)) # Here we confine the selection of the nearest
                right data point (in relation to the global maximum) to within
                100 data points
156         nearest_left_index = np.where(ydata ==
                approximate_half_max_left_point)[0][0] # Here we define the index
                which corresponds to the approximate values set above
157         nearest_right_index = np.where(ydata ==
                approximate_half_max_right_point)[0][0]
158
159         # Defining the Gaussian function (unnormalized)
160         def gaussian(x, a, b, sig):
161             return a*np.exp(-((x-b)**2)/(2*sig**2))
162
163         gmod = Model(gaussian)
164         ### Fitting the defined Gaussian function above to a selected range
                of data ###
165         result = gmod.fit(ydata[0:max_y_index+35],
                x=xdata[0:max_y_index+35], a=max_y, b=xdata[max_y_index],
                sig=xdata[nearest_left_index:nearest_right_index+1].std())
166
167       ##### Data for figure construction #####
168         x_data_array.append(data_x_corrected)
169         y_data_array.append(ydata)
170       ### Select the first plot shown for the linescan
171         if count == 0:
172             data_x_plot_0 = data_x_corrected
173             data_y_plot_0 = data_y
174             lmfit_x_plot_0 = xdata
175             lmfit_y_plot_0 = result.best_fit[0:]
```

```
176             path_first_plot = str(main_path) + "/" + str(linescan_ID) +
                    str("_Raw_data_first_plot")
177             isExist = os.path.exists(path_first_plot)
178             if not isExist:
179               # Create a new directory because it does not exist
180               os.makedirs(path_first_plot)
181
182         ### Select a spectrum of interest
183          elif count == 179:
184             data_x_plot_233 = data_x_corrected
185             data_y_plot_233 = data_y
186             lmfit_x_plot_233 = xdata
187             lmfit_y_plot_233 = result.best_fit[0:]
188             path_233_plot = str(main_path) + "/" + str(linescan_ID) +
                    str("_Raw_data_179_plot")
189             isExist = os.path.exists(path_233_plot)
190             if not isExist:
191               # Create a new directory because it does not exist
192               os.makedirs(path_233_plot)
193
194         ### Select the last plot shown for the linescan
195          elif count == len(s_array)-1:
196             data_x_plot_1 = data_x_corrected
197             data_y_plot_1 = data_y
198             lmfit_x_plot_1 = xdata
199             lmfit_y_plot_1 = result.best_fit[0:]
200             path_last_plot = str(main_path) + "/" + str(linescan_ID) +
                    str("_Raw_data_last_plot")
201             isExist = os.path.exists(path_last_plot)
202             if not isExist:
203               # Create a new directory because it does not exist
204               os.makedirs(path_last_plot)
205
206         ########################################
207
208          # Compute the areas using the composite Simpson's rule.
209          entire_spectrum_area = simps(data_y, dx=dispersion_value)
210          EELS_area = simps(ydata[0:max_y_index+35],xdata[0:max_y_index+35],\
211                          dx=dispersion_value)
212
```

```
213             #### Parameters from the lmfit method ####
214
215             a = result.params['a'].value # The height of the curve's peak
216             b = result.params['b'].value # The position of the centre of the peak
217             x1 = xdata[0] # Lower bound
218             x2 = xdata[len(xdata)-1] # Upper bound
219             sig = result.params['sig'].value # The standard deviation
220             n_steps = 100000 # Selecting how finely we would like to perform the
                    integration. Many points are added here to clearly show the shape
                    of the Gaussian fit
221
222             Gauss_x = np.linspace(x1,x2,n_steps)
223
224             Gaussian_func_vals = []
225
226             for x in Gauss_x:
227                 Gauss_y = a*np.exp(-((x-b)**2)/(2*sig**2))
228                 Gaussian_func_vals.append(Gauss_y)
229
230             #### Data for figure construction #####
231
232             analytical_ZLP = np.sqrt(2*np.pi)*a*sig
233
234             ###################################################################
235             ### Determining the log-ratio ###
236             nat_log_It_I0 = np.log(entire_spectrum_area/EELS_area)
237
238             ### Adding the log-ratio to a storage array ###
239             intensity_ratio_array.append(nat_log_It_I0)
240             ###################################################################
241
242             ### Define the exp. parameters
243             E0_keV = set_acceleration_voltage # Talos 200: 200, TitanHB: 300
244             F_rel_factor = (1+E0_keV/1022)/(1+E0_keV/511)**2
245             ### A variety of definitions exist for Z_eff, choose the desired
                    definition for the calculation ###
246             Z_eff_def = 4
247             if Z_eff_def == 1:
248                 # Quadratic mean Z_eff
249                 Zeff_Si3N4 = np.sqrt(((3/7)*(14)**2)+((4/7)*(7)**2))
```

```
250                 # Quadratic mean Z_eff
251                 Zeff_H2O = np.sqrt(((2/3)*(1)**2)+((1/3)*(8)**2))
252             elif Z_eff_def == 2:
253                 # Mean Z_eff
254                 Zeff_Si3N4 = (3/7)*14+(4/7)*7
255                 # Mean Z_eff
256                 Zeff_H2O = (2/3)*1+(1/3)*8
257             elif Z_eff_def == 3:
258                 # Hine's Z_eff
259                 Zeff_Si3N4 = (((3/7)*(14)**3.1)+((4/7)*(7)**3.1))**(1/3.1)
260                 # Hine's Z_eff
261                 Zeff_H2O = (((2/3)*1**3.1)+((1/3)*(8)**3.1))**(1/3.1)
262             elif Z_eff_def == 4:
263                 # Lenz's Z_eff
264                 Zeff_Si3N4 =
                        (((3/7)*(14)**1.3)+((4/7)*(7)**1.3))/(((3/7)*(14)**0.3)+\
265                                                               ((4/7)*(7)**0.3))
266                 # Lenz's Z_eff
267                 Zeff_H2O =
                        (((2/3)*1**1.3)+((1/3)*(8)**1.3))/(((2/3)*1**0.3)+((1/3)\
268                                                                    *(8)**0.3))
269             Em_Si3N4_eV = (7.6*Zeff_Si3N4**0.36)
270             Em_H2O_eV = (7.6*Zeff_H2O**0.36)
271             collection_angle_mrad = set_collection_angle # Talos 200: 23 mrad #
                    Titan HB: 55 mrad
272             if silicon_nitride_line_scan == True:
273                 IMFP = (106*F_rel_factor*E0_keV)/\
274                     (Em_Si3N4_eV*np.log((2*collection_angle_mrad*E0_keV)\
275                                         /Em_Si3N4_eV))
276                 thickness = IMFP*nat_log_It_I0
277             else:
278                 IMFP = (106*F_rel_factor*E0_keV)/\
279                     (Em_H2O_eV*np.log((2*collection_angle_mrad*E0_keV)\
280                                       /Em_H2O_eV))
281                 thickness = IMFP*(nat_log_It_I0-t_over_lamda)
282             print("Thickness: ", thickness)
283             thickness_array.append(thickness)
284
285             ### Writing important EELS analysis results to a text file ###
286             output.write(str("#################### EELS analysis results from
```

```
            fitting: Result " + str(count+1) + " ################### ")+"\n")
287         output.write(str(result.fit_report())+"\n")
288         output.write(str("Inelastic mean free path (IMFP): " +
                str(IMFP))+"\n")
289         output.write(str("Thickness: " + str(thickness))+"\n")
290         output.write(str("nat_log_It_I0 " + str(nat_log_It_I0))+"\n")
291         output.write(str("Analytical solution (Area of the ZLP): " +
                str(analytical_ZLP))+"\n")
292         output.write(str("Simpson's method (Area of the ZLP: Negative
                energies to minimum): " + str(EELS_area))+"\n")
293         output.write(str("Total area of the EELS spectrum: " +
                str(entire_spectrum_area)) + "\n")
294         output.write(str("############################\
295                          ################################################ "))
296
297         count += 1
298         print (str(100*count/len(s_array)) + " %")
299
300
301 path_1 = str(main_path) + "/" + str(linescan_ID) +
        str("_LMFIT_linescan_thicknesses")
302 # Check whether the specified path exists or not
303 isExist = os.path.exists(path_1)
304
305 ### Storing text files for post-analysis in another script / Excel
306 if not isExist:
307   # Create a new directory because it does not exist
308   os.makedirs(path_1)
309
310 ### Calculated thickness
311 with open(str(path_1)+"/"+"thickness_results.txt", "w") as output:
312     for i in thickness_array:
313         output.write(str(i)+"\n")
314
315 ### Calculated intensity ratio
316 with open(str(path_1)+"/"+"intensity_results.txt", "w") as output:
317     for i in intensity_ratio_array:
318         output.write(str(i)+"\n")
319
320 ##### Saving the first and last spectrum for figure construction #####
```

```
321         with open(str(path_first_plot)+"/"+"Raw_data_x.txt", "w") as output:
322             for i in data_x_plot_0:
323                 output.write(str(i)+"\n")
324         with open(str(path_first_plot)+"/"+"Raw_data_y.txt", "w") as output:
325             for i in data_y_plot_0:
326                 output.write(str(i)+"\n")
327         ########################################################################
328         with open(str(path_233_plot)+"/"+"Raw_data_x.txt", "w") as output:
329             for i in data_x_plot_233:
330                 output.write(str(i)+"\n")
331         with open(str(path_233_plot)+"/"+"Raw_data_y.txt", "w") as output:
332             for i in data_y_plot_233:
333                 output.write(str(i)+"\n")
334         ########################################################################
335         with open(str(path_last_plot)+"/"+"Raw_data_x.txt", "w") as output:
336             for i in data_x_plot_1:
337                 output.write(str(i)+"\n")
338         with open(str(path_last_plot)+"/"+"Raw_data_y.txt", "w") as output:
339             for i in data_y_plot_1:
340                 output.write(str(i)+"\n")
341         ########################################################################
342
343 ##### Talos 200 EELS Analyis #####
344 else:
345     silicon_nitride_line_scan = input("Is the linescan for an empty nanofluidic
        cell (no liquid)? ")
346     if silicon_nitride_line_scan == "Y" or silicon_nitride_line_scan == "Yes" or
        silicon_nitride_line_scan == "yes" or silicon_nitride_line_scan == "y":
347         silicon_nitride_line_scan = True
348     else:
349         silicon_nitride_line_scan = False
350     print("Please open the file for the linescan")
351     file_path = filedialog.askopenfilename()
352     print(file_path)
353     ##### This variable and the subsequent function allow for the creation of
        folders within the path of the data files #####
354     path_to_dm4 = file_path.count("/") # Counting the number of sub-folders
        within the root folder
355     def remove_last(s):
356         num_removed = 0
```

```
357         while s.count("/") == path_to_dm4:
358             try:
359                 s = s[0:-1]
360                 if s.count('/') == path_to_dm4:
361                     num_removed += 1
362                     continue
363                 else:
364                     return [s,num_removed]
365 
366             except ValueError:
367                 return ""
368     initial_file_path = remove_last(file_path)[0] # Finding the root file path
369     linescan_ID = file_path[len(file_path)-remove_last(file_path)[1]:-4] #
        Finding the name of the file ("linescan ID")
370     print(initial_file_path)
371     s = hs.load(file_path) # Using the Hyperspy API to open the .dm4 file
372     s_array = np.array(s[2]) # Converting the filetype from H5py to a numpy
        array for easy manipulation. The spectra are contained within the second
        index of the list
373     main_path = str(initial_file_path) + "/" + str(linescan_ID) # Creating a
        root folder for the linescan
374     # Check whether the specified path exists or not
375     isExist = os.path.exists(main_path)
376 
377     if not isExist:
378       # Create a new directory because it does not exist
379       os.makedirs(main_path)
380 
381     path = str(main_path) + "/" + str(linescan_ID) +
        str("_EELS_linescan_thickness")
382 
383     isExist = os.path.exists(path)
384 
385     if not isExist:
386       # Create a new directory because it does not exist
387       os.makedirs(path)
388 
389     ##### ANALYSIS OF THE SELECTED .dm4 FILE #####
390     count = 0 # First we establish a counter as a means to select where we would
        like to begin data analysis within the linescan
```

```
391     with open(str(path)+"/"+"EELS_thickness_calculation_results.txt", "w") as
            output: # Within the text file that we have created in the newly
            established path, we will conduct data analysis and save the results
392         while count < len(s_array): # While the counter is less then the length
                of the collected data file, we will perform data analysis, change
                this parameter to select individual spectra or groups of spectra from
                a larger dataset
393             output.write(str("#####"+str(s_array[count])+ "#####" + "\n")) # A
                    label to easily search the text file which will be generated
394             data_y = s_array[count] # The intensity of the EELS linescan, this
                    will change as we iterate through the while loop with the counter
395             data_x = np.arange(0, len(data_y), 1) # The x-axis is created as a
                    counter of the step within the linescan
396             max_y = np.max(data_y) # Finding the maximum intensity within the
                    spectrum
397             max_y_index = np.where(data_y == max_y)[0][0] # Finding the index in
                    the numpy array where the spectrum is at an intensity maximum
398             # if max_y_index < 100: # This conditional is used if outliers exist
                    at the beginning of the linescan, eg. a false maximum in the EELS
                    spectrum
399             #     max_y = np.max(data_y[100:])
400             #     max_y_index = np.where(data_y == max_y)[0][0]
401             half_max = max_y/2
402
403             data_x_corrected = []
404             data_x_counter = 0
405             while data_x_counter < max_y_index:
406                 data_x_corrected.append(-max_y_index+data_x_counter)
407                 data_x_counter += 1
408             data_x_corrected.append(0)
409             data_x_counter = 1
410             while len(data_x_corrected) < len(data_y):
411                 data_x_corrected.append(data_x_counter)
412                 data_x_counter += 1
413
414             dispersion_value = \
415                 s[2].original_metadata.ImageList.TagGroup0.\
416                     ImageTags.EELS_Spectrometer.Dispersion_eVCh # Channel is
                        apparently capitalized for the Talos software but not for
                        the Titan software
```

```
417             data_x_corrected = \
418                 np.linspace(data_x_corrected[0]*dispersion_value,\
419                             (len(data_x_corrected)-max_y_index)\
420                                 *dispersion_value-dispersion_value,\
421                                 num=len(data_x_corrected))
422             xdata = np.array(data_x_corrected)
423             ydata = data_y
424
425             ### Since the half-maximum changes quite substantially from each
                    measurement, here we roughly define the half-maximum value on
                    either side of the ZLP, which gives a pseudo FWHM for the
                    construction of the Gaussian function
426             def find_nearest(array, value):
427                 array = np.asarray(array)
428                 idx = (np.abs(array - value)).argmin()
429                 return array[idx]
430
431             approximate_half_max_left_point =
                    (find_nearest(ydata[max_y_index-100:max_y_index], value=half_max))
                    # Here we confine the selection of the nearest left data point (in
                    relation to the global maximum) to within 100 data points
432             approximate_half_max_right_point =
                    (find_nearest(ydata[max_y_index:max_y_index+100], value=half_max))
                    # Here we confine the selection of the nearest right data point
                    (in relation to the global maximum) to within 100 data points
433             nearest_left_index = np.where(ydata ==
                    approximate_half_max_left_point)[0][0] # Here we define the index
                    which corresponds to the approximate values set above
434             nearest_right_index = np.where(ydata ==
                    approximate_half_max_right_point)[0][0]
435
436             # Defining the Gaussian function (unnormalized)
437             def gaussian(x, a, b, sig):
438                 return a*np.exp(-((x-b)**2)/(2*sig**2))
439
440             gmod = Model(gaussian)
441             ### Fitting the defined Gaussian function above to a selected range
                    of data ###
442             result = gmod.fit(ydata[0:max_y_index+24], x=xdata[0:max_y_index+24],
                    a=max_y, b=xdata[max_y_index],
```

```
            sig=xdata[nearest_left_index:nearest_right_index+1].std())
443
444         ##### Data for figure construction #####
445         x_data_array.append(data_x_corrected)
446         y_data_array.append(ydata)
447         ### Select the first plot shown for the linescan
448         if count == 0:
449             data_x_plot_0 = data_x_corrected
450             data_y_plot_0 = data_y
451             path_first_plot = str(main_path) + "/" + str(linescan_ID) +
                    str("_Raw_data_first_plot")
452             isExist = os.path.exists(path_first_plot)
453             if not isExist:
454               # Create a new directory because it does not exist
455               os.makedirs(path_first_plot)
456
457         ### Select a spectrum of interest
458         elif count == 179:
459             data_x_plot_233 = data_x_corrected
460             data_y_plot_233 = data_y
461             path_233_plot = str(main_path) + "/" + str(linescan_ID) +
                    str("_Raw_data_179_plot")
462             isExist = os.path.exists(path_233_plot)
463             if not isExist:
464               # Create a new directory because it does not exist
465               os.makedirs(path_233_plot)
466
467         ### Select the last plot shown for the linescan
468         elif count == len(s_array)-1:
469             data_x_plot_1 = data_x_corrected
470             data_y_plot_1 = data_y
471             path_last_plot = str(main_path) + "/" + str(linescan_ID) +
                    str("_Raw_data_last_plot")
472             isExist = os.path.exists(path_last_plot)
473             if not isExist:
474               # Create a new directory because it does not exist
475               os.makedirs(path_last_plot)
476
477         ########################################
478
```

```
479             # Compute the area using the composite Simpson's rule.
480             entire_spectrum_area = simps(data_y, dx=dispersion_value)
481             EELS_area = simps(ydata[0:max_y_index+24],xdata[0:max_y_index+24],\
482                             dx=dispersion_value)
483
484             #### Parameters from the lmfit method ####
485
486             a = result.params['a'].value # The height of the curve's peak
487             b = result.params['b'].value # The position of the centre of the peak
488             x1 = xdata[0] # Lower bound
489             x2 = xdata[len(xdata)-1] # Upper bound
490             sig = result.params['sig'].value # The standard deviation
491             n_steps = 100000 # Selecting how finely we would like to perform the
                    integration, many points are added here to clearly show the shape
                    of the Gaussian fit
492
493             Gauss_x = np.linspace(x1,x2,n_steps)
494
495             Gaussian_func_vals = []
496
497             for x in Gauss_x:
498                 Gauss_y = a*np.exp(-((x-b)**2)/(2*sig**2))
499                 Gaussian_func_vals.append(Gauss_y)
500
501             #### Data for figure construction #####
502
503             analytical_ZLP = np.sqrt(2*np.pi)*a*sig
504
505             ###################################################################
506             ### Determining the log-ratio ###
507             nat_log_It_I0 = np.log(entire_spectrum_area/EELS_area)
508
509             ### Adding the log-ratio to a storage array ###
510             intensity_ratio_array.append(nat_log_It_I0)
511             ###################################################################
512
513             ### Define the exp. parameters
514             E0_keV = set_acceleration_voltage # Talos 200: 200, TitanHB: 300
515             F_rel_factor = (1+E0_keV/1022)/(1+E0_keV/511)**2
516             ### A variety of definitions exist for Z_eff, choose the desired
```

```
    definition for the calculation ###
Z_eff_def = 4
if Z_eff_def == 1:
    # Quadratic mean Z_eff
    Zeff_Si3N4 = np.sqrt(((3/7)*(14)**2)+((4/7)*(7)**2))
    # Quadratic mean Z_eff
    Zeff_H2O = np.sqrt(((2/3)*(1)**2)+((1/3)*(8)**2))
elif Z_eff_def == 2:
    # Mean Z_eff
    Zeff_Si3N4 = (3/7)*14+(4/7)*7
    # Mean Z_eff
    Zeff_H2O = (2/3)*1+(1/3)*8
elif Z_eff_def == 3:
    # Hine's Z_eff
    Zeff_Si3N4 = (((3/7)*(14)**3.1)+((4/7)*(7)**3.1))**(1/3.1)
    # Hine's Z_eff
    Zeff_H2O = (((2/3)*1**3.1)+((1/3)*(8)**3.1))**(1/3.1)
elif Z_eff_def == 4:
    # Lenz's Z_eff
    Zeff_Si3N4 =
        (((3/7)*(14)**1.3)+((4/7)*(7)**1.3))/(((3/7)*(14)**0.3)+\
                                                ((4/7)*(7)**0.3))
    # Lenz's Z_eff
    Zeff_H2O =
        (((2/3)*1**1.3)+((1/3)*(8)**1.3))/(((2/3)*1**0.3)+((1/3)\
                                                    *(8)**0.3))
Em_Si3N4_eV = (7.6*Zeff_Si3N4**0.36)
Em_H2O_eV = (7.6*Zeff_H2O**0.36)
collection_angle_mrad = set_collection_angle # Talos 200: 23 mrad #
    Titan HB: 55 mrad
if silicon_nitride_line_scan == True:
    IMFP = (106*F_rel_factor*E0_keV)\
        /(Em_Si3N4_eV*np.log((2*collection_angle_mrad*E0_keV)\
                             /Em_Si3N4_eV))
    thickness = IMFP*nat_log_It_I0
else:
    IMFP = (106*F_rel_factor*E0_keV)\
        /(Em_H2O_eV*np.log((2*collection_angle_mrad*E0_keV)\
                           /Em_H2O_eV))
    thickness = IMFP*(nat_log_It_I0-t_over_lamda)
```

```
553             print("Thickness: ", thickness)
554             thickness_array.append(thickness)
555 
556             ### Writing important EELS analysis results to a text file ###
557             output.write(str("#################### EELS analysis results from
                    fitting: Result " + str(count+1) + " ################### ")+"\n")
558             output.write(str(result.fit_report())+"\n")
559             output.write(str("Inelastic mean free path (IMFP): " +
                    str(IMFP))+"\n")
560             output.write(str("Thickness: " + str(thickness))+"\n")
561             output.write(str("nat_log_It_I0: " + str(nat_log_It_I0))+"\n")
562             output.write(str("Analytical solution (Area of the ZLP): " +
                    str(analytical_ZLP))+"\n")
563             output.write(str("Simpson's method (Area of the ZLP): " +
                    str(EELS_area))+"\n")
564             output.write(str("Total area of the EELS spectrum: " +
                    str(entire_spectrum_area)) + "\n")
565             output.write(str("############################\
566                              ################################################ "))
567 
568             count += 1
569             print (str(100*count/len(s_array)) + " %")
570             plt.close("all")
571 
572 
573     path_1 = str(main_path) + "/" + str(linescan_ID) +
            str("_LMFIT_linescan_thicknesses")
574     # Check whether the specified path exists or not
575     isExist = os.path.exists(path_1)
576 
577     ### Storing txt files for post-analysis in another script / Excel
578     if not isExist:
579       # Create a new directory because it does not exist
580       os.makedirs(path_1)
581 
582     ### Calculated thickness
583     with open(str(path_1)+"/"+"thickness_results.txt", "w") as output:
584         for i in thickness_array:
585             output.write(str(i)+"\n")
586 
```

```
    ### Calculated intensity ratio
    with open(str(path_1)+"/"+"intensity_results.txt", "w") as output:
        for i in intensity_ratio_array:
            output.write(str(i)+"\n")

    ##### Saving the first and last spectrum for figure construction #####
    with open(str(path_first_plot)+"/"+"Raw_data_x.txt", "w") as output:
        for i in data_x_plot_0:
            output.write(str(i)+"\n")
    with open(str(path_first_plot)+"/"+"Raw_data_y.txt", "w") as output:
        for i in data_y_plot_0:
            output.write(str(i)+"\n")
    ########################################################################
    with open(str(path_233_plot)+"/"+"Raw_data_x.txt", "w") as output:
        for i in data_x_plot_233:
            output.write(str(i)+"\n")
    with open(str(path_233_plot)+"/"+"Raw_data_y.txt", "w") as output:
        for i in data_y_plot_233:
            output.write(str(i)+"\n")
    ########################################################################
    with open(str(path_last_plot)+"/"+"Raw_data_x.txt", "w") as output:
        for i in data_x_plot_1:
            output.write(str(i)+"\n")
    with open(str(path_last_plot)+"/"+"Raw_data_y.txt", "w") as output:
        for i in data_y_plot_1:
            output.write(str(i)+"\n")
    ########################################################################
```

A.4 Savitzky-Golay filtering

A short script for Savitzky-Golay filtering.

Please see the following article for a detailed theoretical description:

A. Savitzky and M. J. E. Golay, Anal. Chem. 1964, 36, 8, 1627–1639, 1964

doi:10.1021/ac60214a047

This script was developed in the following environment:

Python 3.9.7

matplotlib 3.4.3

tk 8.6.11

numpy 1.20.3

scipy 1.8.0

```
"""
Created on Sun Oct 9 16:58:03 2022

@author: tyler

A short script for Savitzky-Golay filtering

MIT License

Copyright (c) 2023 Tyler Lott

Permission is hereby granted, free of charge, to any person obtaining a copy
of this software and associated documentation files (the "Software"), to deal
in the Software without restriction, including without limitation the rights
to use, copy, modify, merge, publish, distribute, sublicense, and/or sell
copies of the Software, and to permit persons to whom the Software is
furnished to do so, subject to the following conditions:
The above copyright notice and this permission notice shall be included in all
copies or substantial portions of the Software.
THE SOFTWARE IS PROVIDED "AS IS", WITHOUT WARRANTY OF ANY KIND, EXPRESS OR
IMPLIED, INCLUDING BUT NOT LIMITED TO THE WARRANTIES OF MERCHANTABILITY,
FITNESS FOR A PARTICULAR PURPOSE AND NONINFRINGEMENT. IN NO EVENT SHALL THE
AUTHORS OR COPYRIGHT HOLDERS BE LIABLE FOR ANY CLAIM, DAMAGES OR OTHER
LIABILITY, WHETHER IN AN ACTION OF CONTRACT, TORT OR OTHERWISE, ARISING FROM,
OUT OF OR IN CONNECTION WITH THE SOFTWARE OR THE USE OR OTHER DEALINGS IN THE
SOFTWARE.
"""
import os
import matplotlib.pyplot as plt
import tkinter as tk
from tkinter import filedialog
import numpy as np
from scipy.signal import savgol_filter
```

```
34
35 root = tk.Tk()
36 root.withdraw()
37
38 print("Please select the data with which to perform the Savitzky-Golay filtering
       method.")
39
40 file_path = filedialog.askopenfilename()
41 file_path = open(os.path.expanduser(file_path))
42 thickness_array = []
43 for i in file_path:
44     thickness_array.append(i)
45
46 thickness_array_stripped = []
47 data = []
48 ### Cleaning up the text files
49 for i in thickness_array:
50     i_stripped = i.strip('\n')
51     thickness_array_stripped.append(i_stripped)
52
53 for i in thickness_array_stripped:
54     i_stripped2 = float(i.strip("'"))
55     data.append(i_stripped2)
56 x = np.linspace(0,len(data)-1,num=len(data))
57 w = savgol_filter(data, 101, 2)
58 plt.plot(x, w, 'b')
59 plt.plot(x,data,linestyle="-", c="r")
```

Appendix B

Javascript Code for Data Analysis

B.1 Auto contrast of image stacks

A short script and macro to enhance contrast in an image stack.

Auto_contrast_stack.ijm is a macro which can be installed on Fiji / ImageJ to perform the auto-contrasting of a stack of images. ABC_each_image.js is referenced by the Auto_contrast_stack.ijm macro and acts as a short Javascript which uses Fiji's Enhance Contrast command to set the saturation and normalization of pixels in each image.

More information on the Enhance Contrast command can be found in the ImageJ documentation: https://imagej.nih.gov/ij/docs/menus/process.htmlenhance

```
/* MIT License
Copyright (c) 2023 Tyler Lott
Permission is hereby granted, free of charge, to any person obtaining a copy
of this software and associated documentation files (the "Software"), to deal
in the Software without restriction, including without limitation the rights
to use, copy, modify, merge, publish, distribute, sublicense, and/or sell
copies of the Software, and to permit persons to whom the Software is
furnished to do so, subject to the following conditions:
The above copyright notice and this permission notice shall be included in all
copies or substantial portions of the Software.
THE SOFTWARE IS PROVIDED "AS IS", WITHOUT WARRANTY OF ANY KIND, EXPRESS OR
IMPLIED, INCLUDING BUT NOT LIMITED TO THE WARRANTIES OF MERCHANTABILITY,
FITNESS FOR A PARTICULAR PURPOSE AND NONINFRINGEMENT. IN NO EVENT SHALL THE
```

```
AUTHORS OR COPYRIGHT HOLDERS BE LIABLE FOR ANY CLAIM, DAMAGES OR OTHER
LIABILITY, WHETHER IN AN ACTION OF CONTRACT, TORT OR OTHERWISE, ARISING FROM,
OUT OF OR IN CONNECTION WITH THE SOFTWARE OR THE USE OR OTHER DEALINGS IN THE
SOFTWARE.

A short script to convert images in a stack to 16-bit and enhance contrast.
    Saturated pixels are set to 0.35 % with normalization by default.
*/

IJ.run("16-bit", "");
var imp = IJ.getImage();
var n = imp.getStackSize();

for( var i = 0; i < n; ++i) {
    imp.setSlice(i+1);
    IJ.run(imp, "Enhance Contrast", "saturated=0.35 normalize");
}
```

```
/* MIT License
Copyright (c) 2023 Tyler Lott
Permission is hereby granted, free of charge, to any person obtaining a copy
of this software and associated documentation files (the "Software"), to deal
in the Software without restriction, including without limitation the rights
to use, copy, modify, merge, publish, distribute, sublicense, and/or sell
copies of the Software, and to permit persons to whom the Software is
furnished to do so, subject to the following conditions:
The above copyright notice and this permission notice shall be included in all
copies or substantial portions of the Software.
THE SOFTWARE IS PROVIDED "AS IS", WITHOUT WARRANTY OF ANY KIND, EXPRESS OR
IMPLIED, INCLUDING BUT NOT LIMITED TO THE WARRANTIES OF MERCHANTABILITY,
FITNESS FOR A PARTICULAR PURPOSE AND NONINFRINGEMENT. IN NO EVENT SHALL THE
AUTHORS OR COPYRIGHT HOLDERS BE LIABLE FOR ANY CLAIM, DAMAGES OR OTHER
LIABILITY, WHETHER IN AN ACTION OF CONTRACT, TORT OR OTHERWISE, ARISING FROM,
OUT OF OR IN CONNECTION WITH THE SOFTWARE OR THE USE OR OTHER DEALINGS IN THE
SOFTWARE.

An example macro which references the ABC_each_image.js script. This macro
    should be installed and reference the ABC_each_image.js script in the
    appropriate location for personal usage.
```

```
20 */
21
22 runMacro("/Applications/Fiji.app/macros/ABC_each_image.js");
```